

Part I. Influence of Membrane Morphology on Ion-Exchange and Charge  
Propagation in Composite Polyelectrolyte Electrode Coatings.

Part II. Dynamic Surface Tension Measurements of Polarization  
Relaxation at Mercury Pool Electrodes by the Method of Wilhelmy.

Thesis by

Donald David Montgomery

In Partial Fullfillment of the Requirements

for the Degree of

Doctor of Philosophy

California Institute of Technology

Pasadena, California

1990

(Submitted December 14, 1989)

COPYRIGHT 1990

Donald David Montgomery

All Rights Reserved

## ACKNOWLEDGMENTS

I would like to express my appreciation to Richard Borup for his guidance, advice and tolerance as he taught me everything I need to know about the design, construction and machining of scientific instruments within the constraints of a shoe-string budget. Thanks also to Dr. Dave Malerba for his help in matters electronic and always useful discussions on the medieval state of affairs in electrochemistry. I would also like to acknowledge the unwitting and important pedagogical role that Dr. Kip Thorne and other members of the physics department played in demonstrating and demanding a high standard of scholarship, honesty and enthusiasm toward their subject.

Because I find the traditional role of this section as an obligatory sycophantic exercise abhorrent and because I feel that pejorative comments are not appropriate, I will not acknowledge a number of individuals whose role in my graduate education would otherwise warrant comment.

The financial support of the Exxon Education Foundation, the Shell Oil Company and IBM in the form of graduate fellowships, and the National Science Foundation in the form of a research grant is gratefully acknowledged.

## ABSTRACT

Part I. Novel composite polyelectrolyte materials were developed that exhibit desirable charge propagation and ion-retention properties. The morphology of electrode coatings cast from these materials was shown to be more important for its electrochemical behavior than its chemical composition.

Part II. The Wilhelmy plate technique for measuring dynamic surface tension was extended to electrified liquid-liquid interphases. The dynamical response of the aqueous NaF-mercury electrified interphase was examined by concomitant measurement of surface tension, current, and applied electrostatic potential. Observations of the surface tension response to linear sweep voltammetry and to step function perturbations in the applied electrostatic potential (e.g., chronotensiometry) provided strong evidence that relaxation processes proceed for time-periods that are at least an order of magnitude longer than the time periods necessary to establish diffusion equilibrium. The dynamical response of the surface tension is analyzed within the context of non-equilibrium thermodynamics and a kinetic model that requires three simultaneous first order processes.

## TABLE OF CONTENTS

## Part I

## Chapter 1

Introduction.	I-2
Experimental.	I-5
Results.	
A. Ion-Exchange Behavior of Composite Coatings.	I-12
B. Charge Propagation Rates.	I-21
C. Transmission Electron Microscopy of Polyelectrolyte Coatings.	I-33
D. The Roles of the Components of Composite Coatings.	I-38
Summary.	I-42
Bibliography.	I-47

## Chapter 2

Introduction.	I-50
Experimental.	I-52
Results.	
A. Ion-Exchange Behavior.	I-61
B. Transmission Electron Microscopy.	I-67
C. Discussion.	I-70
Summary.	I-74
Bibliography.	I-77

## Part II

## Chapter 3

Introduction.	II-2
Conditions for the Existence of a Separable Electrified Interphase.	II-4
Local Thermodynamics.	II-9
Non-equilibrium Thermodynamics and Relaxation Phenomena.	II-15
An Operative Definition of Chemical Potential for Charged and Polarized Systems.	II-17
Surface Tension.	II-21
Limitations of Non-Equilibrium Thermodynamics.	II-23
Bibliography.	II-26

## Chapter 4

Introduction.	II-30
Experimental.	II-33
A Modified Wilhelmy Plate for Static and Dynamic Surface Tension Measurements at the Electrified Interphase.	II-41
Sensitivity of the Wilhelmy Plate Technique for Static Surface Tension Measurements.	II-46
Equilibrium Surface Tension Measurements.	II-48
Linear Sweep Voltammetry with Concomitant Measurement of the Dynamic Surface Tension.	II-54
Limits to the Response Time of the Wilhelmy Plate Technique.	II-61
Chronotensiometry.	II-70
Effect of Supporting Electrolyte.	II-74
Non-Equilibrium Thermodynamic Analysis of Chronotensiometric Responses.	II-74
An Alternative Kinetic Model for the Chronotensiometric Response of the Surface Tension.	II-90
Summary.	II-95
Bibliography.	II-97

Appendix I	II-100
Appendix II	II-106
Appendix III	II-110

**You can't beat a paradigm at its own game.**

**- Anomalous**

**CHAPTER 1**

## INTRODUCTION

Polyelectrolyte coatings are attractive as a simple means for endowing electrode surfaces with high affinities for either ionic reactants or redox mediators that can be incorporated into the coating by ion-exchange.<sup>1-3</sup> Much of the interest in polyelectrolyte modified electrodes derives from the advantage for electrocatalysis of having immobilized reactants in high concentrations adjacent to the electrode surface. An immobilized system can offer substantial simplification of both separation problems and scale-up relative to the corresponding homogeneous system. There also exists a potential for enhanced electrocatalyst efficiency relative to both the homogeneous and immobilized monolayer cases that could accrue from the capacity of polyelectrolyte coatings to immobilize a large number (e.g. >100) of effective monolayers of reactant at the electrode.<sup>6k</sup>

Although electrodes coated with polyelectrolytes that contain incorporated redox reactants have been exploited in a variety of applications,<sup>3-9</sup> the number of useful polyelectrolyte systems is limited because common polyelectrolytes lack one or more essential properties required for use as effective electrode coatings. These include strong, irreversible binding of the polyelectrolyte to electrode surfaces, reasonable ion-exchange capacity of the coating, retention by the coating of counterionic reactants for long periods when exposed to solutions containing very low concentrations of these counterions, rapid charge propagation rates within the coatings and sufficient long-term chemical and mechanical stability to ensure that polyelectrolyte electrode coatings are something more than a

laboratory curiosity.

A random block copolymer electrolyte, PLC, which incorporates poly(*l*-lysine) as the electrolyte, is perhaps the best single-component material in terms of the criteria outlined above that has been applied to electrode surfaces to bind electroactive counterions.<sup>6f-1</sup> This polymer, for example, is reported to exhibit charge propagation rates that are at least two orders of magnitude larger than have been observed in otherwise attractive coatings prepared from Nafion.<sup>5, 6b, e</sup> Coatings prepared from protonated or quarternized poly(4-vinylpyridine), PVP or QPVP, are less adherent than PLC and much inferior for retaining incorporated anions when transferred to pure supporting electrolyte solutions. The latter shortcoming is also shared by sulfonated polystyrene that has not been cross-linked. Improvements in the stability of PVP and poly(4-vinylpyrazine), PVPz, coatings can be realized by an *in situ* cross-linking procedure that forms robust films.<sup>61-n</sup> The desirable stability features offered by cross-linking are comparable to PLC, but are offset by much slower charge propagation rates and a decrease in coating ion-exchange capacity.

The present chapter describes a series of two-component "composite" electrode coatings that exhibit properties superior to those of PLC.<sup>10</sup> These new coatings consist of a random ternary copolymer, I, containing cationic sites mixed with any one of a series of cationic homopolymers. Copolymer I, which contains both hydrophobic styrene groups and hydrophilic quarternized aminostyrene groups, yields cast films having an internal structure characterized by segregated hydrophobic and hydrophilic domains. By means of

transmission electron microscopy (TEM) it was possible to demonstrate that the self-segregating tendency of the copolymer causes it to exert a strong influence on the internal structures of coatings prepared from its mixtures with auxiliary, single-component polyelectrolytes. Close inspection of TEM micrographs revealed that the domain morphology of composite coatings was relatively indifferent to the chemical nature of different auxiliary polyelectrolytes. Thus, the copolymer can be considered as a structural template that establishes domain morphology inside composite coatings. Unlike coatings cast from single-component polyelectrolytes, the ion-exchange and charge propagation properties displayed by these coatings were also independent of the chemical nature of auxiliary polyelectrolytes. This result led to the conclusion that film morphology, far more than the chemical composition, is the dominant factor determining electrochemical behavior of composite coatings.

**EXPERIMENTAL****Materials.**

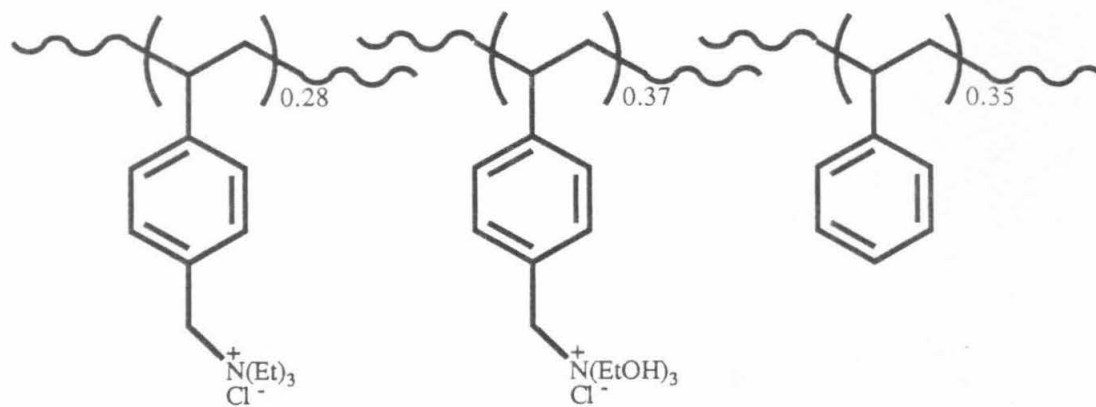
Poly(n-vinyl-2-methylimidazole), PVI (Figure 1E), of average molecular weight  $7 \times 10^4$  daltons and the functionalized nylons (Figures 1B-D) were prepared by standard procedures.<sup>13, 14</sup> All other auxiliary polyelectrolytes (Figures 1F-1J) were commercially available samples that were used as received.

Except as noted, *vide infra*, all supporting electrolyte solutions consisted of 0.1 M anhydrous sodium acetate adjusted to pH 4.5 with glacial acetic acid. Laboratory distilled water was purified by passage through a purification train (Barnsted Nanopure). Solutions of the counterionic species were prepared from the appropriate analytical grade salts. Solutions of  $K_4Fe(CN)_6$  were prepared immediately prior to the experiment in which they were employed.

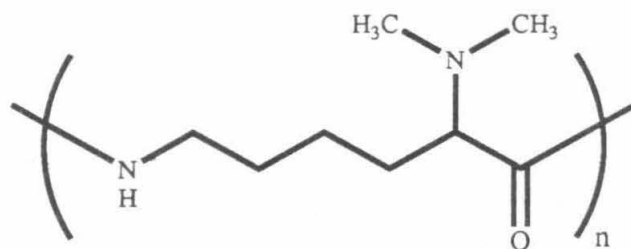
**Random Ternary Copolymer I.**

A benzene solution containing 0.6 M styrene, 2.4 M chloromethylstyrene, and 6 mM 2,2'-azobis(isobutyronitrile), AIBN, as an initiator was degassed on a vacuum line according to standard procedure.<sup>11</sup> The polymerization was allowed to proceed for 24 hours at 60 °C and consumed about 70% of the monomers. The resulting random binary copolymer was isolated and purified by reprecipitation from n-hexane. The Menshutken reaction<sup>12</sup> was employed to convert the chloromethyl groups in the copolymer to quarternary amine groups using first triethyl amine and subsequently triethanol amine. The resulting ternary copolymer was dissolved in concentrated HCl and dialyzed against water for two days to remove unreacted amine and other low

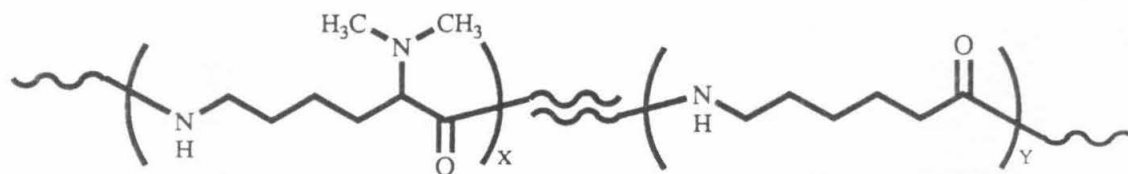
Figure 1. Structures of the copolymers and auxiliary polyelectrolytes used in this study. (A) Random ternary copolymer I. The proportions of the three groups were calculated from the percentage of chloride and nitrogen it contained. (B) Dimethylamino nylon. (C,D) Random binary copolymers of nylon and dimethylamino nylon. The values of X and Y were determined from elemental analysis. (E) Poly(1-vinyl-2-methyl-imidazole). (F) Poly(4-vinylpyridine). (G) Poly(L-lysine) = PLL. (G) Linear poly(ethyleneimine). (H) Branched poly(ethyleneimine).



(A)



(B)



(C)

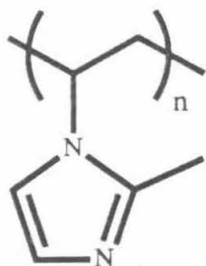
$$X = 0.52$$

$$Y = 0.48$$

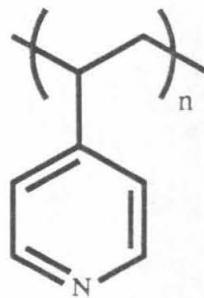
(D)

$$X = 0.33$$

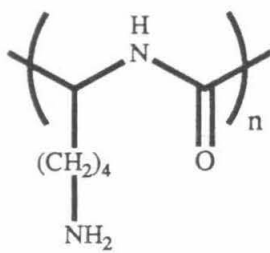
$$Y = 0.67$$



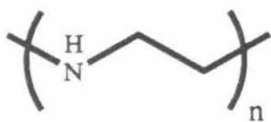
(E)



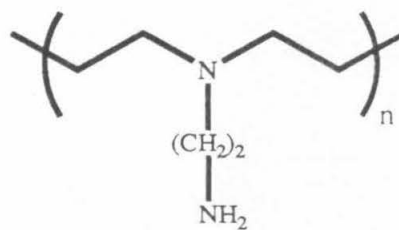
(F)



(G)



(H)



(I)

molecular weight impurities. The aqueous polyelectrolyte solution became quite turbid during the course of the dialysis and THF was added at this point to improve the solubility of the polyelectrolyte. The resulting solvent ratio (THF:H<sub>2</sub>O) for the slightly turbid 1 wt.% solution was ca. 1:1. The final 0.5 wt.% polyelectrolyte solution from which the coatings were prepared was approximately 25% water by volume (0.67 M THF/ 1.0 M H<sub>2</sub>O) and remained slightly turbid. The composition of the ternary copolymer (Figure 1a) was determined by elemental analysis for Cl and N at each step of the synthesis as well as infrared spectroscopy. Its molecular weight was not estimated.

#### Apparatus and Procedures.

Glassy carbon electrodes (Tokai Electrode Manufacturing Co., Ltd.; Tokyo, Japan) having an area of 0.34 cm<sup>2</sup> were mounted and prepared as previously described.<sup>1b</sup> The hanging mercury drop electrode was conventional (Brinkmann Instruments, Inc.) and was filled with triply distilled mercury (Bethlehem Instruments Co.).

Cyclic voltammetry was conducted with conventional, previously described procedures and instrumentation.<sup>1b, d</sup> The quantity of electroactive counterion incorporated by an electrode coating was measured coulometrically after transfer to pure supporting electrolyte solution. The potential was ramped at 2 mVs<sup>-1</sup> immediately after transfer until a potential well beyond the peak potential was reached and maintained at that point until the current had decreased to background levels (ca. 10-20 s). After subtracting background values, the total charge passed during an experiment was used to calculate the quantity of electroactive counterion that could access the electrode. Slopes of chronocoulometric charge vs. (time)<sup>-1/2</sup> plots were used to

estimate diffusion coefficients for electroactive counterions incorporated inside coatings.<sup>1b, 6e</sup> The data were obtained with an electrochemical analyzer (Bioanalytical Systems, model 100) and evaluated graphically. Relatively long measurement times (25 ms) were employed to avoid possible nonlinearity arising from the uncompensated resistance presented by the coatings. All electrochemical experiments employed a conventional two-compartment cell. Solutions were deaerated with pre-purified argon. Potentials were measured and are reported with respect to a sodium chloride-saturated calomel reference electrode (SSCE). Experiments were conducted at ambient temperatures ( $22 \pm 2^\circ\text{C}$ ).

Coatings were cast by transferring  $2\mu\text{l}$  aliquots of solutions of the polyelectrolytes in aqueous THF-methanol (1:1) to freshly polished glassy carbon electrodes and allowing the solvent to evaporate at room temperature. All solutions contained 0.5 wt.% of the appropriate polyelectrolytes.

Coating thickness was estimated by micrometric measurements on coatings prepared from 10 to 20 times more polyelectrolyte than was employed experimentally with the assumption that the thickness was a linear function of the quantity of polyelectrolyte used.<sup>6g</sup>

Transmission electron micrographs were obtained with a Phillips EM 201 instrument. Coatings were cast on 400 mesh copper minigrids (Ted Pella, Inc.) that were first coated with a thin layer of carbon by conventional procedure.<sup>23</sup> One  $\mu\text{l}$  aliquots of 0.005 wt.% solutions of the polyelectrolytes of interest in aqueous THF-methanol (1:1) were carefully applied to the coated minigrids using a  $10\mu\text{l}$  syringe, and allowed to dry for thirty minutes. To stain the resulting coatings,

one  $\mu\text{l}$  of a  $1 \times 10^{-7}$  M solution of  $\text{IrCl}_6^{3-}$  in a 0.1 M acetate buffer (pH 4.5) was syringed onto the coating and time allowed for the coating to swell and incorporate the  $\text{IrCl}_6^{3-}$ . Next, 1.5  $\mu\text{l}$  of deionized water was applied to the coating, allowed to stand five minutes, and then carefully wicked away using the fine point of a triangular sliver of filter paper. The coatings were then allowed to dry for several hours before they were used. This last step proved necessary in order to remove most of the residual supporting electrolyte, which otherwise tended to form micro-crystals that obscured morphological features revealed by the staining procedure.

For purposes of comparison, micrographs were also taken of unstained coatings treated with a solution of pure supporting electrolyte and of coatings in which ferrocene was used in place of  $\text{IrCl}_6^{3-}$  as a staining agent. The procedure was identical to that used to obtain the  $\text{IrCl}_6^{3-}$ -stained coatings in both cases. Scanning electron micrographs were taken with an ETEC Autoscan instrument. Samples of the coated and stained minigrids used for scanning microscopy were mounted on a stud and prepared using conventional procedures.<sup>23</sup>

Interference micrographs were obtained with a Nikon Optiphot microscope equipped with a tilting stage and a 10x Mireau-type interference objective. A filter was used to obtain monochromatic green light at 5460 Å. Interferometry of dry coatings was performed on samples prepared by casting 2  $\mu\text{l}$  of 0.5 wt.% polymer solution onto a glass slide marked to denote a 0.34  $\text{cm}^2$  circular area.

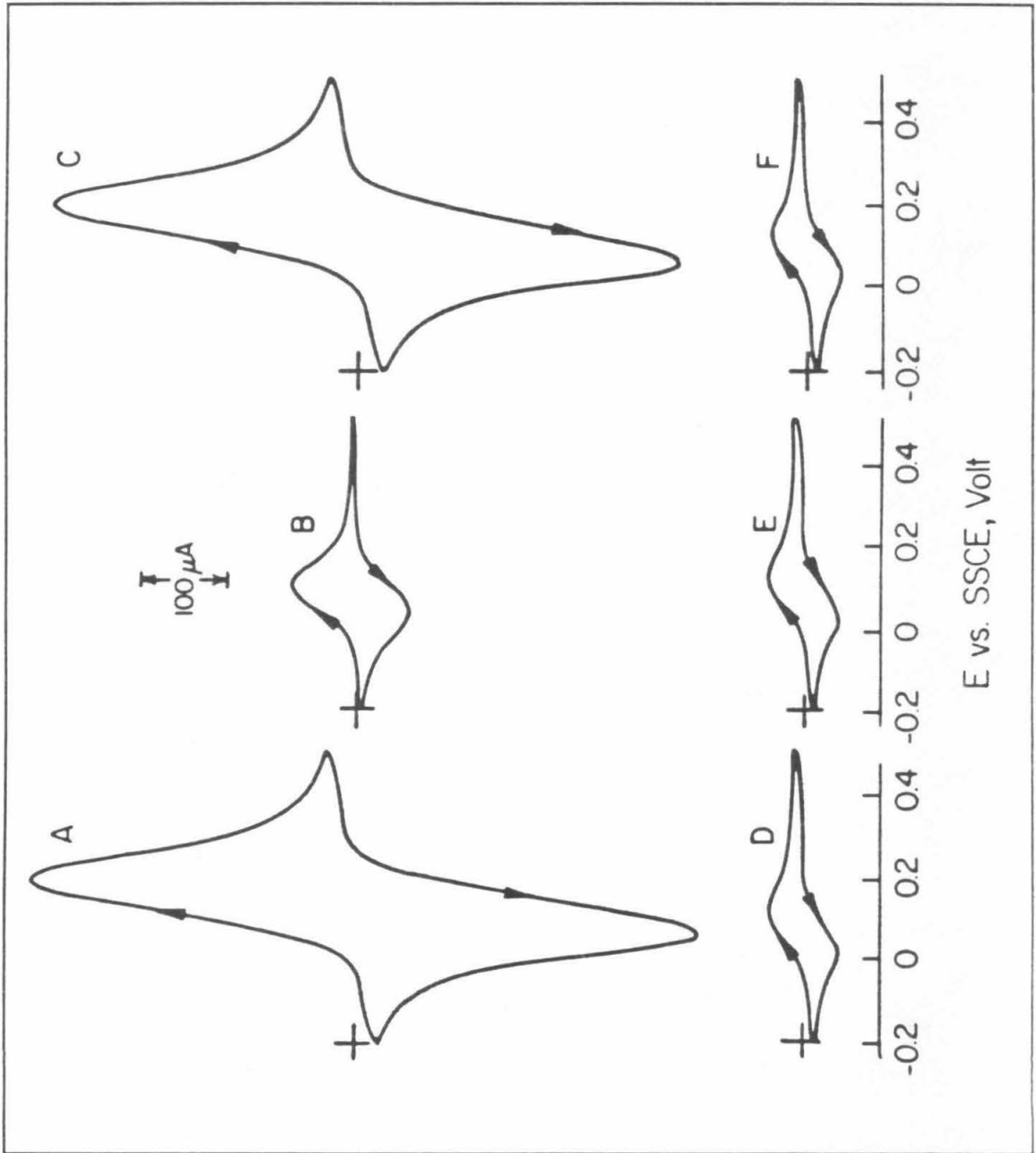
## RESULTS

## A. Ion-Exchange Behavior of Composite Coatings.

Cyclic voltammetry is a useful diagnostic tool for making rapid, qualitative evaluation of the ion-exchange properties of swollen polyelectrolyte membranes on electrodes. The peak current,  $i_p$ , of a voltammetric wave due to the presence of an incorporated electroactive counterion (e.g.  $\text{Fe}(\text{CN})_6^{4-}$ ) is directly proportional to the concentration of that counterion within the coating, and thus serves as an index for comparing counterion concentration within different coatings. Time-resolved measurement of  $i_p$ , while a coating is exposed to a pure supporting electrolyte solution after having first been loaded to a steady-state value with electroactive and polyvalent counterions, is a useful test of its ability to retain those ions against a large concentration gradient between ions in the film and in solution.

The set of steady-state cyclic voltammograms in Figure 2 compares the responses of: i) PVI (Figure 2, A and B); ii) I (Figure 2, C and D); iii) a composite system composed of PVI and I (Figure 2, E and F). The response immediately after each coating (that had been equilibrated with 0.1 mM  $\text{Fe}(\text{CN})_6^{4-}$ ) was transferred to a pure supporting electrolyte solution (represented in Figures 2A, 2C and 2E). The corresponding response after 45 minutes of exposure to the supporting electrolyte solution is exhibited in Figures 2B, 2D and 2F. The coatings prepared from either PVI (Figure 2A) or I (Figure 2C) alone, incorporate relatively little  $\text{Fe}(\text{CN})_6^{4-}$  and much of this is lost within 45 minutes (Figure 2, B and D). This contrasts

Figure 2. Steady-state cyclic voltammograms for  $\text{Fe}(\text{CN})_6^{4-}$  incorporated into pure and composite polyelectrolyte coatings on a glassy carbon electrode ( $0.34 \text{ cm}^2$ ). Coating compositions: (A), (B), pure PVI; (C), (D), pure copolymer I; (E), (F), PVI + copolymer I. All curves were recorded in pure supporting electrolyte solutions ( $0.1 \text{ M CH}_3\text{COONa} + \text{CH}_3\text{COOH}$ ; pH 4.5) where the electrode was transferred after it was equilibrated with  $10^{-4} \text{ M Fe}(\text{CN})_6^{4-}$  in the same electrolyte for the 5-10 minutes required for a stable response to be obtained. Curves (A), (C) and (E) were recorded immediately after the transfer. Curves (B), (D) and (F) were recorded 45 minutes after the transfer. The dashed curve in (E) is the voltammogram for  $10^{-4} \text{ M Fe}(\text{CN})_6^{4-}$  at the uncoated electrode. Scan rate  $100 \text{ mVs}^{-1}$ .



dramatically with the response obtained from the composite coating (Figure 2, E and F). Much more  $\text{Fe}(\text{CN})_6^{4-}$  is incorporated initially by the composite coating and is lost much more slowly when the coating is transferred to a pure supporting electrolyte solution. The composite coating exhibits properties that would not be expected on the basis of the behavior of its two components alone and displays synergistic enhancement of both net ion-exchange capacity and ion-retention capability.

Although useful as a qualitative index of incorporated electroactive counterion concentration, cyclic voltammetry is an uncertain technique for obtaining solid quantitative values due to the difficulty of assessing the contributions to  $i_p$  from film capacity and uncompensated resistance and an unreliable knowledge of the effective diffusion coefficient for charge propagation. A quantitative measurement was obtained by coulometry during exhaustive electrolysis of incorporated counterions.

One measure of the ion-exchange capacity of polyelectrolyte coatings is the ratio of electroactive counterion initially incorporated into a coating,  $\Gamma_0$ , multiplied by the charge of that counterion,  $z$ , to the total quantity of monovalent charge sites calculated to be in the film,  $\Gamma_p$ . This number,  $z\Gamma_0/\Gamma_p$ , is defined here as the steady-state ion-exchange capacity and will, unless otherwise indicated, refer to coatings equilibrated with a 0.1 mM solution of electroactive counterion in 0.1 M aqueous and monovalent supporting electrolyte. As a measure of relative ion-exchange capacity this ratio incorporates two tenuous assumptions: i) all polymer-bound charge sites are equally accessible to incorporated

electroactive counterions and *ii*) all incorporated electroactive counterions have equal access to the electrode and can be measured by coulometry. Nevertheless, use of a steady-state ion-exchange capacity ratio as a tool for comparing polyelectrolyte coating materials in a given supporting electrolyte environment is both practical and common in the literature.

Measurement of coating ion-retention capability is a tedious and somewhat arbitrary experimental task because the time scale for equilibration of a loaded coating with a pure supporting electrolyte solution can be on the order of weeks for some materials reported here. The most direct and informative measure would be a rate constant for leaching of polyvalent counterion from a coating. However, the kinetics of leaching for coatings cast from both single-component and two-component polyelectrolyte solutions were complex, non-monotonic and a strong function of relative loading values. Because differences between single-component and composite coatings were very large, a detailed understanding of the leaching kinetics was judged ancillary to the primary objective of evaluating the relative virtues of different coating materials. Instead, the simple ratio of the quantity of incorporated electroactive counterion retained by a film after 45 minutes exposure to 0.1 M pure monovalent supporting electrolyte solution,  $\Gamma_{45}$ , to the quantity initially incorporated by equilibration of a film with a 0.1 mM solution of the electroactive counterion in the same electrolyte,  $\Gamma_0$ , was found to be a useful qualitative measure of coating ion-retention capability. This quantity,  $\Gamma_{45}/\Gamma_0$ , is defined here as the retention ratio. The assumptions of coating homogeneity and equal electrode access that are

made for the steady-state ion-exchange capacity are operative for retention ratios as well because all  $\Gamma$  values are measured coulometrically. Thus, any changes in this ratio are assumed to result from leaching of electroactive counterions from the coating and not from structural changes inside the coating that could modify the ability of electroactive species to gain access to the electrode surface. A 45 minute exposure period was chosen largely as a matter of experimental convenience but is practical as a comparative index because the rate at which incorporated polyvalent counterions leach from most common single-component polyelectrolyte coatings is so rapid that 5-10 minutes of exposure to pure supporting electrolyte is sufficient to result in the loss of all electrochemical response from the coating. Forty-five minutes is also a large time window in which most electrochemical experiments utilizing polyelectrolyte coatings can be performed.

Values of  $z\Gamma_0/\Gamma_p$  and  $\Gamma_{4,5}/\Gamma_0$  for several single component polyelectrolyte coatings (Table I) and a series of corresponding composite coatings (Table II) have been measured. The retention ratios listed in Table II for the composite coatings are all very similar and quite large. Indeed, the value of 0.93 obtained for the composite coating prepared from PVI and I is the largest observed for any cationic polyelectrolyte.  $\text{Fe}(\text{CN})_6^{4-}$  actually leaches from these coatings very slowly over longer times, e.g. 71% was retained after 36 hours. The values obtained for the steady-state ion-exchange capacities of the composite coatings are, however, not exceptionally large and display considerable variability from one coating to the next. The possibility that the large changes in steady-state

Table I

Retention Ratios and Diffusion Coefficients for  $\text{Fe}(\text{CN})_6^{4-}$  and Other  
Multiply-Charged Counterions Incorporated in Electrode Coatings  
Prepared from Single Polyelectrolytes.

Coating Material <sup>a</sup>	$10^7 \Gamma_p^b$ mol $\text{cm}^{-2}$	Counterion	$10^8 \Gamma_0^c$ mol $\text{cm}^{-2}$	$\Gamma_{45}/\Gamma_0^d$	$Z\Gamma_0/\Gamma_p^e$	$10^6 D_E^f$ $\text{cm}^2 \text{s}^{-1}$
I	0.45	$\text{Fe}(\text{CN})_6^{4-g}$	0.37	0.73	0.33	<i>k</i>
PVI	1.55	$\text{Fe}(\text{CN})_6^{4-g}$	0.39	0.54	0.10	<i>k</i>
PVP	5.37	$\text{Fe}(\text{CN})_6^{4-h}$	10.3	-	0.77	0.0038
PLC	2.8	$\text{Mo}(\text{CN})_8^{4-i}$	-	-	0.70	0.76
Nafion	-	$\text{Ru}(\text{NH}_3)_6^{3+j}$	-	-	-	0.002

a. Abbreviations: I, see Figure 1(A); PVI, see Figure 1(E); PVP, see Figure 1(F); PLC, a block copolymer of poly-L-lysine<sup>6h</sup>.

b. Total quantity of fixed charge sites in the polyelectrolyte coating.

c. Quantity of counterion incorporated by the coating as measured coulometrically immediately after transfer to pure supporting electrolyte solution.

d. Retention ratio: fraction of the initially incorporated counterion that was retained after 45 minutes of exposure to pure supporting electrolyte solution.

e. Fraction of the fixed charge sites occupied by the electroactive counterions of charge Z.

f. Effective diffusion coefficient of the multiply-charged counterions incorporated in the coating as measured coulometrically in pure supporting electrolyte solution.

g. Supporting electrolyte: 0.1 M  $\text{CH}_3\text{COONa} + \text{CH}_3\text{COOH}$  (pH 4.5).

h. Supporting electrolyte: 0.1 M  $\text{CF}_3\text{COONa} + \text{CF}_3\text{COOH}$  (pH 1.8).<sup>17</sup>

i. Supporting electrolyte: 0.2 M  $\text{CH}_3\text{COONa} + \text{CH}_3\text{COOH}$  (pH 5.5).<sup>6h</sup>

j. Supporting electrolyte: 0.5 M  $\text{Na}_2\text{SO}_4$ .<sup>6e</sup>

k. Uncertainty in coating thickness prevented calculation of  $D_E$ .

Table II

Retention Ratios and Diffusion Coefficients for  $\text{Fe}(\text{CN})_6^{4-}$  Incorporated in Electrode Coatings Prepared from Composite Polyelectrolyte Systems.

Coating Material <sup>a</sup>	$10^7 \Gamma_p^b$ mol cm <sup>-2</sup>	$10^8 \Gamma_0^c$ mol cm <sup>-2</sup>	$\Gamma_{45}/\Gamma_0^d$	$Z\Gamma_0/\Gamma_p^e$	$10^3 \phi^f$ cm	$10^6 D_E^g$ cm <sup>2</sup> s <sup>-1</sup>
PVI + I <sup>h</sup>	1.99	2.40	0.93	0.48	1.0	1.6
PVP + I <sup>i</sup>	1.85	2.27	0.84	0.49	1.0	1.4
PVP + I <sup>j</sup>	1.85	2.32	0.82	0.50	0.9	1.1
PVP + I <sup>k</sup>	1.85	2.12	0.85	0.46	1.1	1.5
ND1 + I	1.39	2.18	0.88	0.63	0.8	1.5
ND2 + I	0.99	1.90	0.92	0.77	0.9	1.9
ND3 + I	0.83	1.12	0.84	0.54	1.2	4.9
b-PEI + I <sup>l</sup>	3.87	3.96	0.82	0.41	1.1	3.6
l-PEI + I	3.87	4.64	0.87	0.48	1.1	2.9
PLL + I <sup>m</sup>	1.16	2.15	0.83	0.74	1.1	2.1
PVI + I <sup>n</sup>	7.22	8.30	0.91	0.46	0.3	1.4

- a. Abbreviations: I, see Figure 1(A); PVI, see Figure 1(E); PVP, see Figure 1(F); ND1, see Figure 1(B); ND2, see Figure 1(C); ND3, see Figure 1(D); b-PEI, see Figure 1(I); l-PEI, see Figure 1(G); PLL, see Figure 1(G).
- b. Total quantity of fixed charge sites in the polyelectrolyte coating. I contributed  $0.45 \times 10^7$  mol cm<sup>-2</sup> to the value of  $\Gamma_p$  in each case.
- c. Quantity of  $\text{Fe}(\text{CN})_6^{4-}$  incorporated by the coating upon equilibration with a  $10^{-4}$  M solution as measured coulometrically immediately after transfer to pure supporting electrolyte solution.
- d. As in Table I.
- e. As in Table I.
- f. Coating thickness.
- g. Calculated from equation (1).
- h. MW =  $7 \times 10^4$  daltons.
- i. MW =  $7.5 \times 10^5$  daltons.
- j. MW =  $7 \times 10^4$  daltons.
- k. MW =  $1 \times 10^4$  daltons.
- l. MW =  $1.8 \times 10^3$  daltons.
- m. MW =  $1.8 \times 10^5$  daltons.
- n. Experiment performed with a hanging mercury drop electrode: surface area  $2.22 \times 10^{-2}$  cm<sup>2</sup>; total amount of 0.5 wt.% coating solution was 0.25  $\mu\text{L}$ .

ion-exchange capacity values between different composite coatings reflects a real difference in ion incorporation mechanisms is unlikely because of the close similarities in retention ratio values, apparent diffusion coefficients and internal morphologies, *vide infra*, exhibited by these coatings. It is more likely that differences in ion-exchange capacity can be attributed to a breakdown in one or both of the assumptions that lend utility to this measure as a comparative tool. In particular, the calculated value  $\phi \Gamma_p$  may not represent the actual number of polymer-bound charge sites accessible to  $\text{Fe}(\text{CN})_6^{4-}$ . The real value of  $\Gamma_p$  may vary widely from one composite coating to the next for at least two reasons: *i*) polymer-bound charge sites could be buried within hydrophobic portions of a coating where they are inaccessible to counterions from the solution and the relative proportion of such inaccessible charge sites is likely to depend on the chemical structure and molecular weight of the auxiliary polyelectrolyte and *ii*) local pH within a coating could vary with auxiliary polyelectrolyte and prevent complete protonation of amine functional groups.

Both steady-state ion-exchange capacity and retention ratio values rely on assumptions of coating homogeneity and equal electrode access because they must be measured by coulometry. However, the actual form of their dependence on these assumptions is markedly different. For use as an effective comparative index, the steady-state ion-exchange capacity requires that the ratio of available polymer-bound charge sites to calculated charge sites for different coatings be nearly identical for different coatings. Ideally, this ratio should be very close to unity. The retention

ratio, on the other hand, only requires that the number of available polymer-bound charge sites be time-invariant. The actual values of  $\Gamma_p$  for different polyelectrolyte coating materials are not important. Hence, the retention ratio is a more robust measure for evaluation of the relative merits of different polyelectrolyte electrode coating materials than the steady-state ion-exchange capacity.

#### B. Charge Propagation Rates.

The holy grail of polyelectrolyte electrode coating research is a material that will immobilize high concentrations of an electrocatalyst, remain stable for millions of catalyst turnover cycles, and compete with or improve upon the electrocatalytic efficiency measured for both the corresponding homogeneous solution and single monolayer cases. Saveant and Andrieux have calculated the enhancement to electrocatalytic efficiency for a simple  $EC_{cat}$  reaction that could result from immobilization of up to 100 effective monolayers of catalyst within an ideal polyelectrolyte electrode coating. The calculated enhancement depends critically upon both the rate at which charge can propagate through the film and the ability of substrate and product species to diffuse into and out of the coating.<sup>6k</sup> For the expected enhancement to materialize, the diffusion coefficients for charge, substrate and product transport must be at least  $10^{-7} \text{ cm}^2 \text{ s}^{-1}$ . Thus, the charge propagation rate is a key requirement for effective and useful polyelectrolyte electrode coatings. To date, the only materials that have displayed effective diffusion coefficients of this magnitude for aggregate charge transport processes mediated by ionic reactants confined within polyelectrolyte electrode coatings have been PLC and the composite

coatings described here.<sup>6b, e, 15, 16</sup>

Effective diffusion coefficients for charge propagation in coatings are estimated by standard electrochemical methods used to evaluate diffusion coefficients for electroactive species in isotropic media.<sup>1b, 15, 17</sup> In accordance with usual and customary procedure, potential-step chronocoulometry was used in this study. Experiments were performed after a coating that had been equilibrated with a 0.1 mM  $\text{Fe}(\text{CN})_6^{4-}$  solution was transferred to pure supporting electrolyte and allowed to stand for 45 minutes. The total quantity of  $\text{Fe}(\text{CN})_6^{4-}$  present in the coating at this point,  $\Gamma_{45}$ , was measured immediately prior to chronocoulometry experiments. The chronocoulometric slopes,  $S$ , were evaluated graphically from quasi-linear regions of the charge vs.  $(\text{time})^{1/2}$  plots. The effective diffusion coefficient,  $D_E$ , was calculated using a form of the integrated Cottrell equation:<sup>17</sup>

$$D_E = \frac{\pi S^2 \Phi^2}{4n^2 F^2 \Gamma_{45}^2} \quad (1)$$

where  $\Phi$  is the coating thickness,  $n$  the number of electrons involved in the redox process and  $F$  the faraday. The quantity  $\Gamma_{45} \Phi^{-1}$  corresponds to the bulk concentration,  $C_o^*$ , found in the standard form of the Cottrell equation. Use of this quantity implies an assumption of homogeneous distribution of electroactive counterion within a coating.

To evaluate coating thickness,  $\Phi$ , for composite systems, films cast from 10 to 20 times the quantity of 0.5 wt.% polymer solution normally employed for electrochemical experiments were prepared and

allowed to swell in a supporting electrolyte solution containing 0.1 mM  $\text{Fe}(\text{CN})_6^{4-}$  for one hour. The swollen membrane was then removed from solution and  $\Phi$  estimated by eye with the aid of a micrometer. The value of  $\Phi$  for at least three coatings cast from different aliquots of polymer solution (typically 10, 15 and 20 times normal experimental quantities) was measured for each composite material and these values used to construct a plot of  $\Phi$  vs. aliquot volume. A  $\Phi$  value for calculation of  $D_E$  (Table II) was obtained by linear extrapolation from the measured values for large aliquot volumes down to the much smaller aliquot volumes used to cast coatings for electrochemical evaluation. Successful application of this technique to estimate  $\Phi$  values was possible for composite coatings because they swell to occupy volumes at least two orders of magnitude greater than their dry volumes. The thickness of coatings that do not swell appreciably, such as Nafion or I, are estimated more reliably by measuring dry coating thickness and assuming  $\Phi$  is very close to this value.

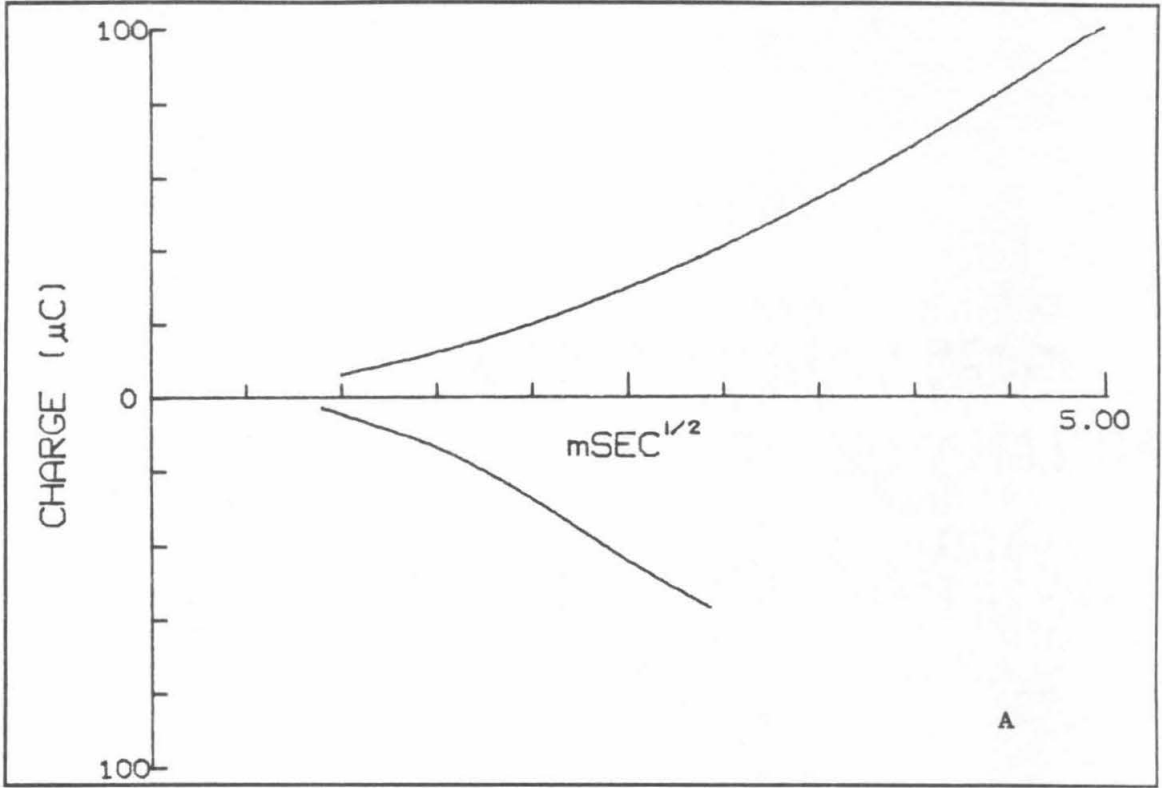
Although useful for estimating the thickness of highly swollen coatings, this technique suffers significant interpretative and technical problems. At an interpretative level, two problematic assumptions are required: *i*) the measured *ex situ* values of  $\Phi$  are nearly identical to *in situ* values and *ii*) a reliable estimate of  $\Phi$  for experimental systems can be obtained by a simple linear interpolation from the measured  $\Phi$  vs. aliquot volume values down to aliquot volumes at least an order of magnitude smaller. An osmotic pressure is probably the primary force driving swelling of polyelectrolyte electrode coatings. This osmotic driving force

disappears when a coated electrode is removed from the supporting electrolyte solution. It is not unreasonable to expect a partial collapse of the swollen polyelectrolyte membrane under these conditions. This would violate the first assumption above and cause a systematic underestimate of  $\Phi$ . In addition, gravity-driven mechanical deformation is not allowed under this assumption. However, thick films examined under a microscope appear to slump over time (e.g. seconds) in response to a downward flow of interstitial water. Significant slumping would cause a systematic overestimate of  $\Phi$ . The second assumption of a linear relation between film thickness and aliquot volume is neither supported nor contradicted by the data. However, establishment of any functional relationship is difficult because sequential estimates of  $\Phi$  for different coatings cast from a given aliquot of polymer solution often resulted in values that differed by at least 10 percent.

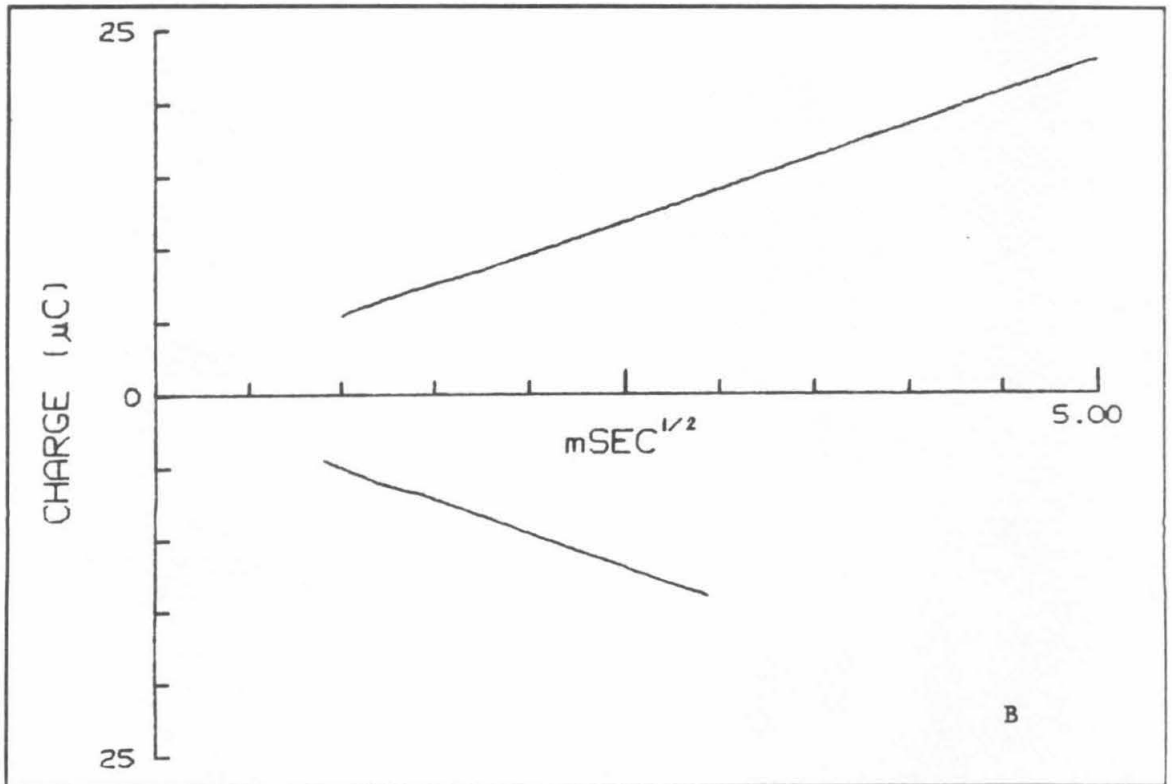
Thus, the compound effects of uncertainty in experimental values and marginal assumptions conspire to make estimated thickness values a large source of error for calculated charge propagation rates. The uncertainty in  $\Phi$  is much larger than error in coulometric measurement of  $\Gamma_{4,5}$  and at least twice the uncertainty in the slope of chronocoulometric charge vs.  $(\text{time})^{1/2}$  plots, *vide infra*. It is important to note that any error in  $\Phi$ ,  $\Gamma_{4,5}$  or  $S$  is squared in equation (1).

Figures 3A and 3B compare the chronocoulometric response of a composite coating containing PVI as the auxiliary polyelectrolyte and loaded with  $\text{Fe}(\text{CN})_6^{4-}$  as previously described (Figure 3A) with that obtained at a bare glassy carbon electrode using a 0.001 M solution of

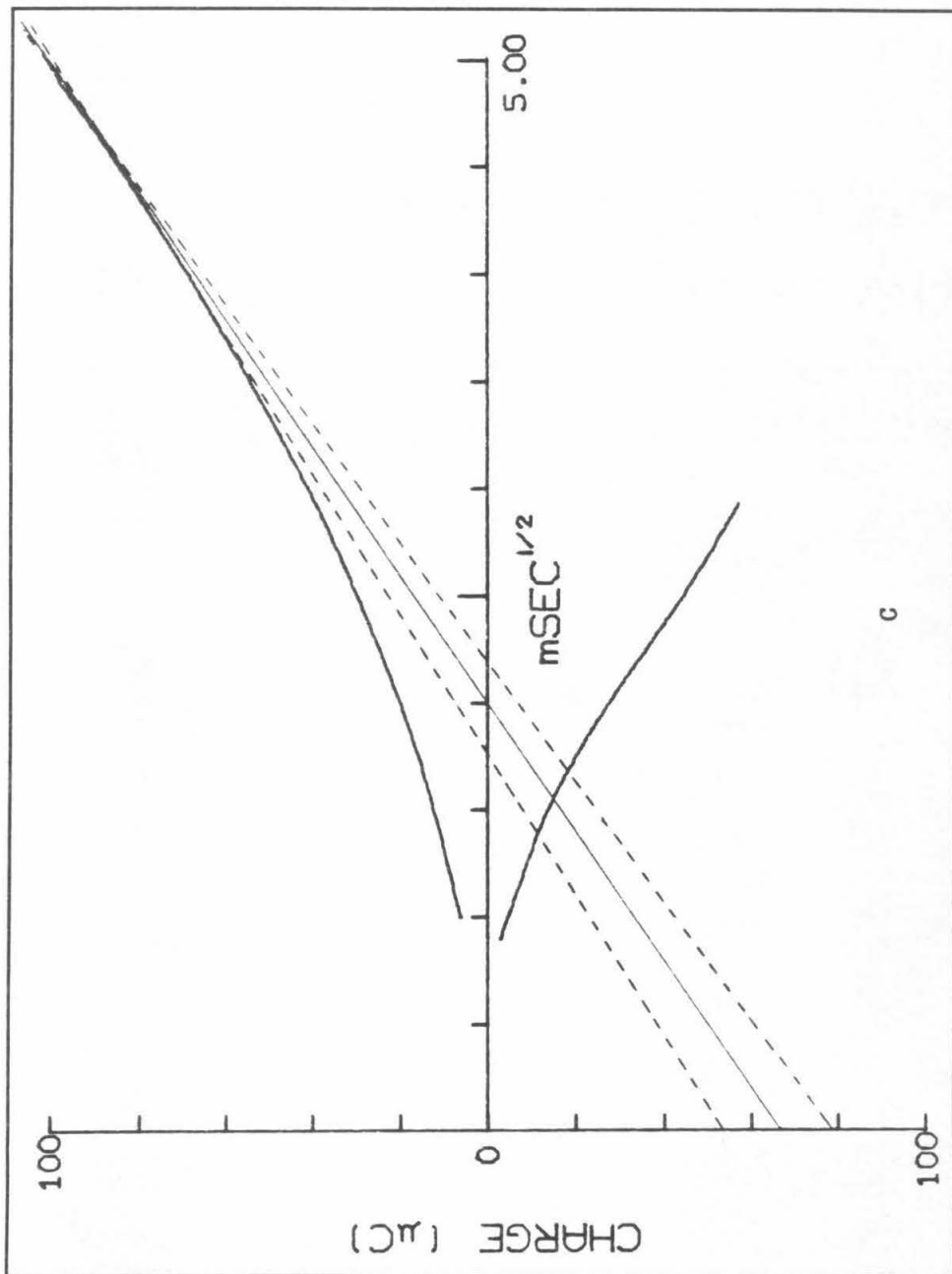
Figure 3. Double-step chronocoulometric charge vs.  $(\text{time})^{1/2}$  curves for  $\text{Fe}(\text{CN})_6^{4-}$  at a bare glassy carbon electrode ( $0.34 \text{ cm}^2$ ) and incorporated into a composite coating cast onto the same glassy carbon electrode. (A) PVI + copolymer I composite coating. (B)  $0.001 \text{ M}$   $\text{Fe}(\text{CN})_6^{4-}$  in a  $0.1 \text{ M}$   $\text{CH}_3\text{COONa} + \text{CH}_3\text{COOH}$  supporting electrolyte solution (pH 4.5) at a bare electrode. (C) Same as (A), dotted lines are tangent to points at the beginning and end of the "quasi-linear" regime (see text) of the double-step chronocoulometric charge vs.  $(\text{time})^{1/2}$  curve obtained for the forward step. The solid line is tangent to a point in the middle of the "quasi-linear" regime. Curves (A) and (C) were recorded after exposing the coating to pure supporting electrolyte solution ( $0.1 \text{ M}$   $\text{CH}_3\text{COONa} + \text{CH}_3\text{COOH}$ ; pH 4.5) for 45 minutes where the electrode was transferred after it was equilibrated with  $10^{-4} \text{ M}$   $\text{Fe}(\text{CN})_6^{4-}$  in the same electrolyte.



A



B



$\text{Fe}(\text{CN})_6^{4-}$  (Figure 3B). Inspection of Figure 3A will reveal that the charge vs.  $(\text{time})^2$  curves are not linear. For electroactive counterions sequestered inside the polyelectrolyte electrode coatings used in this study, nonlinearity in chronocoulometric charge vs.  $(\text{time})^{1/2}$  curves is a universal feature. The prevailing explanation for nonlinearity is that the polyelectrolyte coating presents either a large uncompensated resistance, or an interfacial capacitance that is much larger than those found at bare electrodes, or both. This results in a large RC time constant and charging current persists for a time period sufficient to introduce large nonlinearity into the initial portion of the curve. Once the charging current has disappeared and semi-infinite boundary conditions established for redox couples diffusing through the film to the electrode, the charge vs.  $(\text{time})^{1/2}$  curve should become linear. The curve will then remain linear until reserves of electroactive counterion are depleted and semi-infinite boundary conditions break down. This occurs when the diffusion length scale,  $2(D_E t)^{1/2}$ , approaches  $\Phi$ . For representative values of  $D_E$  (ca.  $2 \times 10^{-6} \text{ cm}^2 \text{ s}^{-1}$ ) and  $\Phi$  (ca.  $1 \times 10^{-3} \text{ cm}$ ) semi-infinite boundary conditions should begin to break down after  $\sim 0.2 \text{ s}$ . The value of  $S$  for calculation of  $D_E$  should be obtained from the linear region of the curve where the system is operating under semi-infinite linear diffusion conditions.

Experimental chronocoulometric charge vs.  $(\text{time})^{1/2}$  curves for composite coatings (e.g. Figure 3A) do not exhibit any uniquely linear regions. Values for  $S$  were obtained from the slope of a line tangent to a point in the middle of a region where the slope of tangent lines varies slowly with time (e.g. "quasi-linear" region). This was done

graphically as demonstrated in Figure 3C where a line tangent to a point in the middle of the quasi-linear region (solid line) has been added to the curve from Figure 3A. The dotted tangent lines in Figure 3C are taken from points near the beginning and end of the quasi-linear region of the curve. Because there is no *a priori* reason to assume that any given tangent line in the quasi-linear region is a better estimate of  $S$  than another, the range of tangent slopes between the dotted tangent lines represents the uncertainty in  $S$  introduced by this graphical method. A value at or near the middle of the quasi-linear region was taken as the best compromise. The uncertainty in  $S$  evaluated from Figure 3C is on the order of  $\pm 5\%$ . Thus, although the uncertainty in  $S$  is significant, it is not as large as that introduced by estimates of  $\Phi$ .

Values of  $D_E$  calculated for a series of composite coatings are listed in the final column of Table II. These may be compared with the values given in Table I for coatings prepared from polyelectrolytes of homogeneous chemical composition. It is of interest to note that  $D_E$  values calculated from chronocoulometric data for  $\text{Fe}(\text{CN})_6^{4-}$  in composite coatings are all within an order of magnitude of the literature value for  $\text{Fe}(\text{CN})_6^{4-}$  in solution ( $D = 6.5 \times 10^{-6} \text{ cm}^2 \text{ s}^{-1}$ ).<sup>18</sup> This literature value, however, was obtained from chronoamperometry experiments at a shielded electrode and the value obtained from the chronocoulometric data in Figure 3b ( $D = 1.6 \times 10^{-5} \text{ cm}^2 \text{ s}^{-1}$ ) is nearly twice as large. A systematic inflation of  $D_E$  values for  $\text{Fe}(\text{CN})_6^{4-}$  in homogeneous electrolyte solutions seems to be a general feature of chronocoulometric measurements at solid electrodes. The effect can be ascribed to

surface roughness and edge effects that cause the effective area of the electrode to be greater than the measured area.<sup>24</sup> These factors may also be important for chronocoulometric evaluation of  $D_E$  for ionic reactants inside polyelectrolyte electrode coatings and lead to systematic overestimates. Nevertheless, these effective diffusion coefficients remain among the largest ever measured in polyelectrolyte coatings on electrodes.

Given the experimental uncertainties outlined above, interpretation of  $D_E$  as a quantitative measure of charge propagation rates within polyelectrolyte electrode coatings is problematic at best. It is more appropriate that  $D_E$  be viewed only as a rough qualitative index of the relative resistance that any given coating presents to the transport of charge along a direction normal to the electrode surface. *Caveat emptor.*

The high values of  $D_E$  make it unlikely that electron exchange between pairs of the oxidized and reduced reactants could contribute to the measured diffusional rates in the way proposed by Dahms and Ruff<sup>20, 21</sup> and inferred for  $\text{Co}(\text{bpy})_3^{2+}$  (bpy = bipyridine) incorporated in Nafion.<sup>6e</sup> Using the equation of Dahms and Ruff, a rate constant for self-exchange between redox reactants inside polyelectrolyte coatings can be estimated, e.g.;<sup>6e, 10, 21</sup>

$$D_E = D_o + \pi k_{ex} \delta^2 \Gamma_{4,5} \Phi / 4 \quad (2)$$

Where  $D_o$  is the diffusion coefficient that would be measured in the absence of any electron self-exchange,  $k_{ex}$  is the second order rate constant ( $\text{M}^{-1}\text{s}^{-1}$ ) governing the self-exchange reaction and  $\delta$  is the distance between the centers of ions when electron transfer occurs.

The conventional choice for a value of  $\delta$  is the estimated diameter of the ion. The rate constant for self-exchange between  $\text{Fe}(\text{CN})_6^{3-}$  and  $\text{Fe}(\text{CN})_6^{4-}$  would have to be on the order of  $10^9 \text{ M}^{-1}\text{s}^{-1}$  in the composite coatings where the concentration of incorporated  $\text{Fe}(\text{CN})_6^{4-}$  was ca. 0.02 M in order for self-exchange to contribute even 10% to a  $D_E$  value as large as  $2 \times 10^{-6} \text{ cm}^2\text{s}^{-1}$ . The value of  $10^9 \text{ M}^{-1}\text{s}^{-1}$  calculated from equation (2) is an unreasonably large rate constant for self-exchange between these two highly charged anions<sup>22</sup> and is the basis for the conclusion that self-exchange does not make a substantial contribution to charge transport processes as measured by  $D_E$  in the composite coatings described here.

Values for the retention ratio and  $D_E$  for several different ionic reactants are presented in Table III. These data suggest that charge transport processes in composite coatings are not strongly influenced by the chemical nature of, or net charge on, incorporated tri- and tetravalent counterions under the experimental conditions employed. Thus, composite coatings appear to offer very low intrinsic resistance to propagation of charge by redox active counterions they incorporate despite their abilities to retain these ions for extended periods. It is reasonable to expect the robust ion-retention capability of composite coatings to be associated with tight ionic bonding of polyvalent counterions to immobilized charge sites within the coating. However, this property might also reasonably be regarded as incompatible with the high rates of charge propagation exhibited by the films and their indifference toward the valency or chemical nature of the redox active counterion employed. If the ion-exchange and charge transport behavior of polyelectrolyte electrode coatings

Table III

Retention Ratios and Diffusion Coefficients for Tri- and Tetravalent Counterions Incorporated within Composite Coatings Prepared from PVI and I.

Counterion	$10^7 \Gamma_p^a$ mol cm <sup>-2</sup>	$10^8 \Gamma_0^b$ mol cm <sup>-2</sup>	$\Gamma_{4.5}/\Gamma_0^c$	$Z\Gamma_0/\Gamma_p^d$	$10^3 \phi^e$ cm	$10^6 D_E^f$ cm <sup>2</sup> s <sup>-1</sup>
Fe(CN) <sub>6</sub> <sup>3-</sup>	1.99	3.32	0.91	0.50	0.9	1.1
Ir(Cl) <sub>6</sub> <sup>3-</sup>	1.99	3.13	0.92	0.48	1.1	1.6
Mo(CN) <sub>8</sub> <sup>4-</sup>	1.99	2.33	0.89	0.47	0.9	1.2

a. As in Table II.

b. As in Table I.

c. As in Table I.

d. As in Table I.

e. As in Table II.

f. As in Table II.

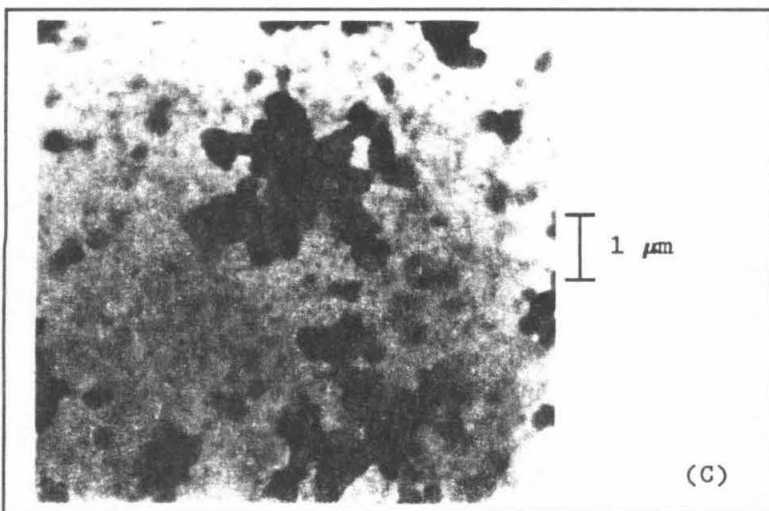
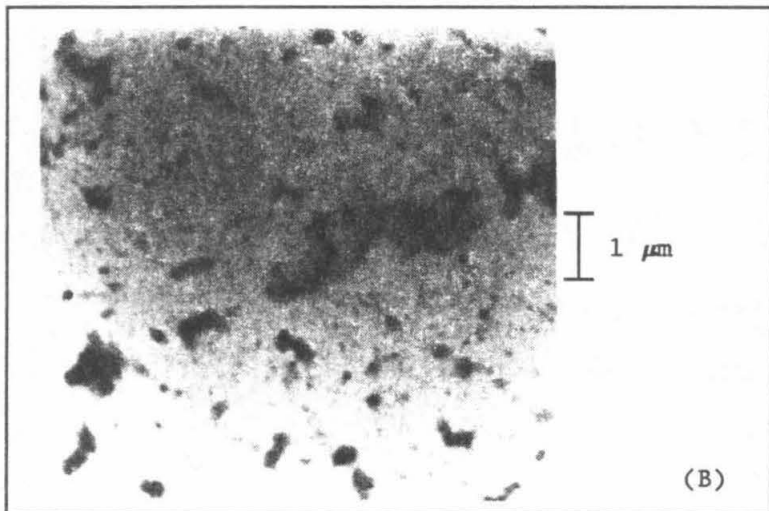
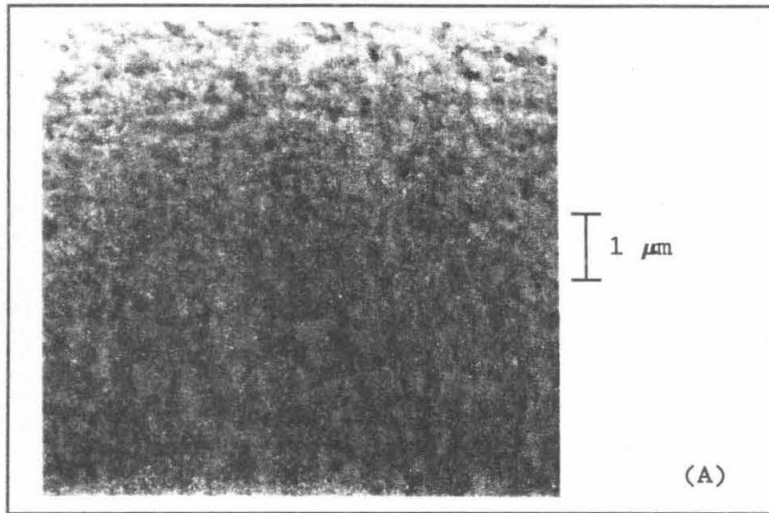
depends only on molecular scale interactions, then the observed behavior presents a seemingly insurmountable paradox. On the other hand, if the observed behavior has its origin in macroscopic scale interactions controlled by the internal morphology of a coating then the paradox may be more apparent than real.

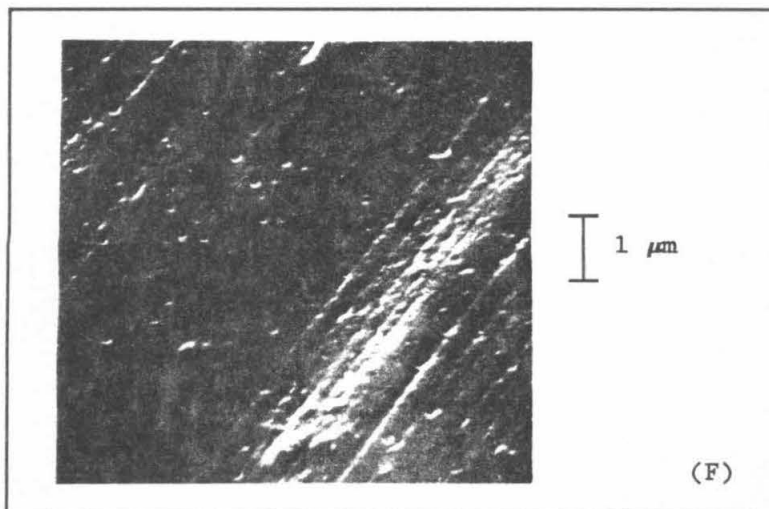
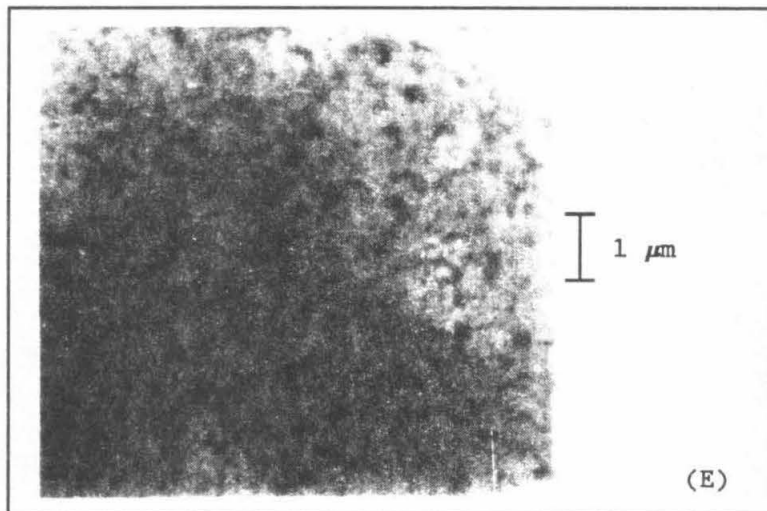
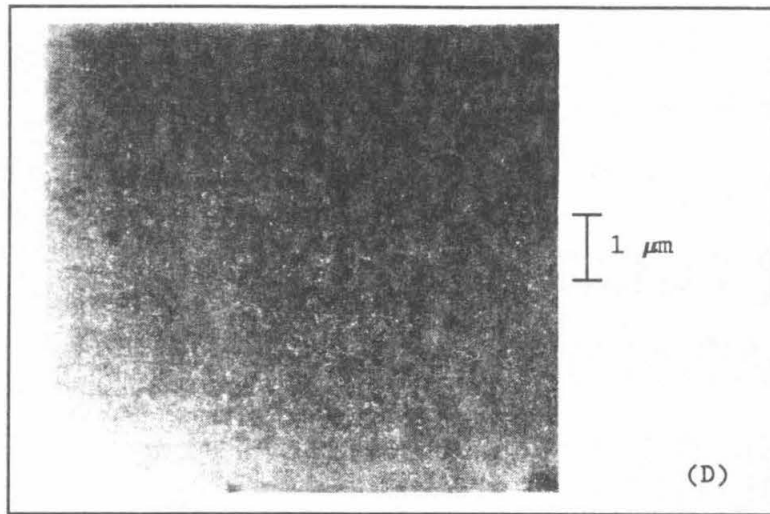
### C. Transmission Electron Microscopy of Polyelectrolyte Coatings.

The implication that morphology may influence the behavior of polyelectrolyte coatings on electrodes is something of a recurrent theme in the literature devoted to the topic.<sup>19</sup> The paradoxical ion-exchange and charge transport behavior and the invariance of these properties between composite coatings prepared from a mixture of I with any of a series of different auxiliary polyelectrolytes (Table II) suggested that a factor other than chemical identity could be important for determining coating behavior. To examine the proposition that morphological factors play a role in coating behavior more directly, transmission electron microscopy (TEM) was employed to examine coatings cast onto carbon layers that were deposited on copper minigrid supports. The resulting coatings were swollen and stained with  $\text{Ir}(\text{Cl})_6^{3-}$  that was incorporated and retained by hydrophilic portions of the polycationic coatings when they were washed with distilled water (see Experimental Section).

Micrographs obtained for five types of coatings are shown in Figure 4. The coating in Figure 4A was prepared from a PVP homopolymer. It exhibits an almost homogeneous structure with little evidence of microphase-separated domains. A similar lack of structure is observed in micrographs of all coatings prepared from auxiliary polyelectrolytes. Figure 4B is a micrograph of a coating cast from

Figure 4. (A)-(E) transmission electron micrographs of polyelectrolyte coatings on carbon-coated copper grids. Preparation of the samples is given in the Experimental Section: (A), pure PVP (MW =  $7.5 \times 10^5$  daltons), (B), pure copolymer I, (C), composite coating prepared from PVP + I, (D), repeat of (C) with the use of only pure supporting electrolyte during the sample preparation, (E), repeat of (C) substituting ferrocene for  $\text{IrCl}_6^{3-}$  as the staining agent. (F) Scanning electron micrograph of a composite coating prepared in the same fashion as (C).





copolymer I. The film appears much less homogeneous with segregation into features that can be interpreted as two types of domains that differ in their ability to accept the  $\text{IrCl}_6^{3-}$  stain. A composite coating prepared from a mixture of PVI and I, Figure 4C, exhibits a similar structure wherein the phase that is stained by  $\text{IrCl}_6^{3-}$  segregates into roughly spherical domains that aggregate together. The structure evident in the micrographs of Figures 4B and 4C seems likely to arise from spontaneous microphase-separation of the coating into hydrophilic and hydrophobic domains. The ternary copolymer I was synthesized to contain both hydrophilic and hydrophobic groups and there is considerable precedent for such materials adopting microphase-separated domains when cast as films or membranes.<sup>19</sup> Hence, the regions that are stained more readily and that aggregate together in the micrographs are believed to have incorporated  $\text{IrCl}_6^{3-}$  by ion-exchange and to represent hydrophilic domains that are dispersed within a hydrophobic matrix that constitutes the remainder of the coating. In isolation, the hydrophilic domains appear to have average diameters of about 700 Å in coatings prepared from copolymer I alone (Figure 4B) but this dimension increases to ca. 2000 Å when I is mixed with PVP (Figure 4C). This expansion may well result from the preferential association of the hydrophilic auxiliary polyelectrolyte with hydrophilic phases of I. The homology of the domain structures displayed in Figure 4B and 4C indicates that, in mixtures, I acts as a template to induce the auxiliary polyelectrolyte to adopt a similar structure. Thus, the conclusion that I is responsible for the general morphological features observed in micrographs of composite coatings seems reasonable.

A pair of coatings comprised of PVP and I were prepared using supporting electrolyte alone (Figure 4D) and a  $10^{-7}$  M solution of ferrocene in supporting electrolyte (Figure 4E) to assure that the structural features seen in Figures 4a-4c were the result of incorporation of  $\text{IrCl}_6^{3-}$  anions into the charged hydrophilic domains and not an artifact of the staining procedure. The featureless micrograph exhibited in Figure 4D indicates that the supporting electrolyte is completely removed during the staining procedure and that without a staining agent there are no observable features in the film. Figure 4E indicates that a neutral molecule with considerable hydrophobic character, ferrocene, is unable to stain the coating effectively. The possibility that the features observed are due to small clusters of polymer that could form as a result of the staining procedure was addressed by scanning electron microscopy (SEM) of the coated and stained minigrids (Figure 4F). The smooth surface displayed by a stained coating of PVP and I in Figure 4F indicates that morphological features observed in TEM micrographs do not reflect the external structure of the coatings. Thus, it appears that the features that result when the coatings are stained with  $\text{IrCl}_6^{3-}$  represent hydrophilic domains that contain a large number of polymer-bound charge sites accessible to anions.

#### D. The Roles of the Components of Composite Coatings

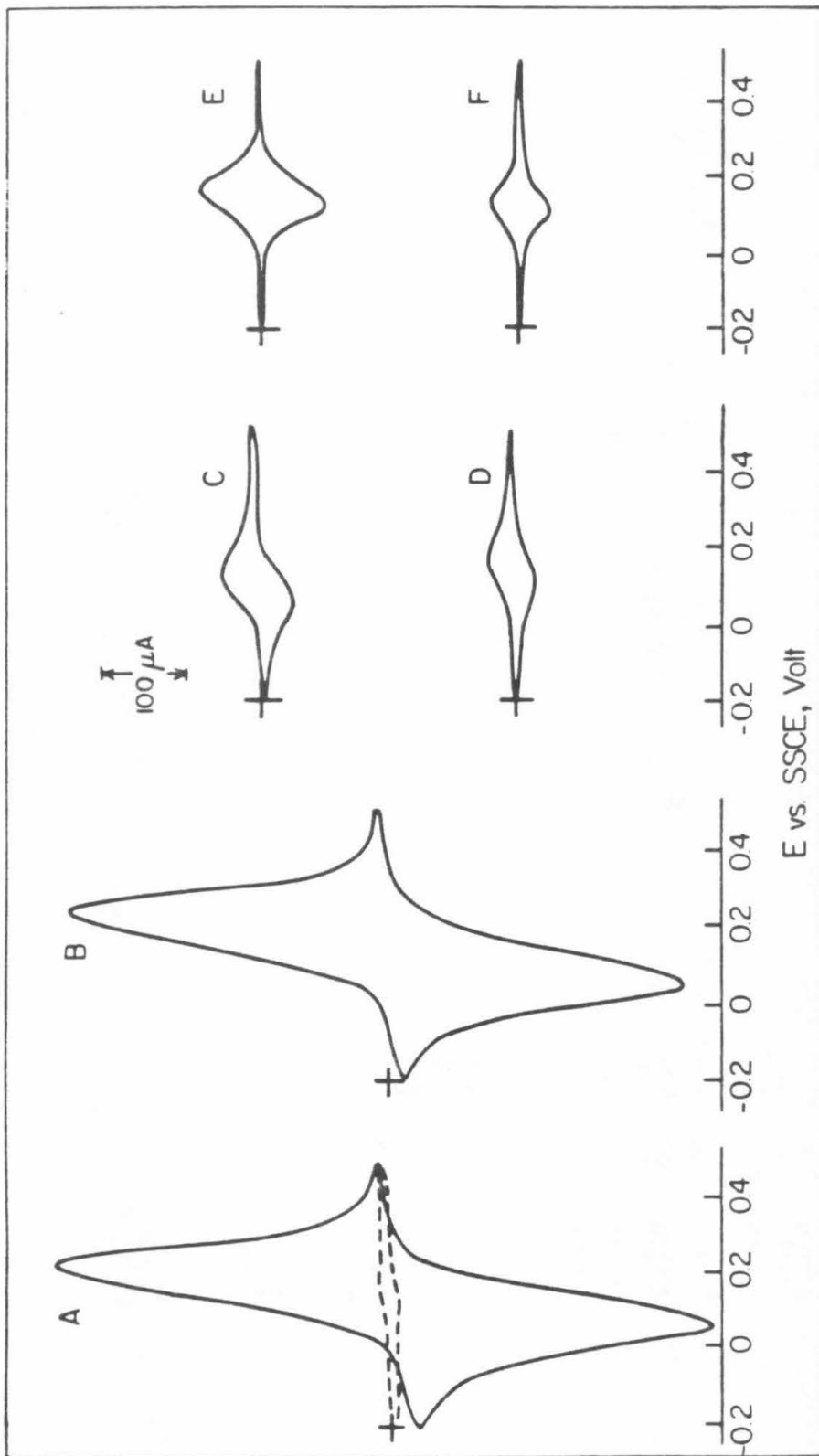
The quantity of  $\text{Fe}(\text{CN})_6^{4-}$  incorporated by different composite coatings relative to the calculated maximum (Table II) varies over a considerable range whereas the retention ratios,  $\Gamma_{45}/\Gamma_0$ , and  $D_E$  values are insensitive to changes in the chemical identity and molecular weight of the auxiliary polyelectrolyte. In addition, of all the

auxiliary polyelectrolytes employed here to form composite coatings (Table II), only PVI yielded coatings with sufficient stability when used alone under these experimental conditions to permit reliable evaluation of its behavior (Table I). Thus, it is reasonable to conclude that I is responsible for the stability of the composite coatings as well as other desirable properties they exhibit.

This stabilizing effect of I allows long-lived coatings to be applied to a wide variety of electrode materials. In addition to glassy carbon and pyrolytic graphite, satisfactorily stable coatings have been cast on gold, tin oxide, platinum and even a hanging mercury drop electrode (Table II). In the latter case, the coated mercury drop was readily transferred between solutions without dislodging the drop from the capillary tube from which it was suspended, a much more difficult task when attempted with an uncoated drop.

The values of  $\Gamma_0$  in Tables II and III are all well below the limit calculated from the number of cationic sites  $\Gamma_p$  assumed to be provided by the composite coatings. It was of interest to determine the relative importance of the two components of the composite coating for electrostatic binding of the multi-valent counterions within the coating. This was possible because cationic sites in auxiliary polyelectrolytes were provided by protonation of basic sites and could be removed at sufficiently high pH values. The quarternary ammonium groups responsible for the cationic sites on copolymer I retain their charge at all pH values. An example of the use of pH to alter the number of fixed charge sites within a composite coating prepared from a mixture of PVI and I is shown in Figure 5. At pH 4.5 the imidazole groups in the PVI ( $pK_a = 8.5$ ) are protonated, both components of the

**Figure 5.** pH dependence of steady-state cyclic voltammograms for  $\text{Fe}(\text{CN})_6^{4-}$  incorporated in a composite coating of copolymer I + PVI, (A)-(C), and in copolymer I alone, (D)-(F). Curves (A), (C), (D) and (F) were recorded in  $10^{-4}$  M solution of  $\text{Fe}(\text{CN})_6^{4-}$  at pH 4.5. For curves (B) and (E) the pH was 10.0. Other conditions as in Figure 2.



coating are polycationic and the coating readily incorporates  $\text{Fe}(\text{CN})_6^{4-}$  (Figure 5A). If the loaded coating is transferred to a 0.1 mM  $\text{Fe}(\text{CN})_6^{4-}$  solution at pH 10, the coating shows a greatly attenuated response (Figure 5B) despite the fact that the cationic sites carried by I are still present. Retransfer of the electrode back to the pH 4.5 solution of  $\text{Fe}(\text{CN})_6^{4-}$  restores most of the original response (Figure 5C) indicating that the coating remains on the electrode surface and regains its ion-exchange capacity upon re-protonation. Figures 5D through 5F represent the response of a coating prepared from 1  $\mu\text{l}$  of a 0.5 wt.% solution of copolymer I alone. As before, Figure 5d shows the initial response of the coating when loaded with  $\text{Fe}(\text{CN})_6^{4-}$  from a pH 4.5 solution, Figure 5E displays the response of that coating when transferred to a pH 10 solution, and Figure 5F exhibits the behavior of the coating when transferred back to the original pH 4.5 solution. The quarternary ammonium charge sites on copolymer I should be insensitive to the pH of the supporting electrolyte and the response of the coating (Figure 5, D through F) was consistent with this fact. These results indicate that the auxiliary polyelectrolyte in a composite coating is the principle agent responsible for the incorporation of  $\text{Fe}(\text{CN})_6^{4-}$ . This conclusion is in agreement with the results summarized in Table I that show copolymer I alone has a poor capacity for incorporating  $\text{Fe}(\text{CN})_6^{4-}$  anions.

#### SUMMARY.

The work described in this chapter had two distinct goals. First, to describe composite coating materials and to demonstrate that they are useful for polyelectrolyte electrode coatings. Second, to

examine the proposition that the internal morphology of composite coatings is the dominant factor influencing their electrochemical behavior.

A test protocol was established to evaluate the relative ion-exchange, ion-retention, charge-propagation and stability of different polyelectrolyte electrode coating materials. All of these properties are considered essential for the effective use of electrode coatings in a variety of chemical contexts, most notably electrocatalysis. Although this test protocol proved useful in general, analysis of assumptions about the physical state of polyelectrolyte interiors that are necessary for effective use of the test protocol described here, led to the conclusion that electrochemically measured steady-state ion-exchange capacity has limited use as an index for comparison of different coating materials. Chronocoulometric measurement of charge transport rates also was shown to suffer from inherent and serious experimental and interpretative problems. This is a problem that warrants concern because of the very important role  $D_e$  would play in practical applications of polyelectrolyte electrode coatings. Nevertheless, when composite coating materials are compared with homogeneous single-component polyelectrolytes and other materials that have been evaluated in a similar fashion in the literature, they offer a superior combination of ion-retention, stability and charge propagation properties.

The electron micrographs in Figure 4 illustrate clearly the morphological differences between coatings cast from homopolyelectrolytes on the one hand, and copolymer I, containing both charged, hydrophilic groups and hydrophobic groups, on the other.

Coatings prepared from homopolyelectrolytes appear largely featureless whereas copolymer I yields coatings that appear segregated into two types of domains. Of greater importance to the present study was the observation that copolymer I appears to retain its domain-forming tendency when mixed with auxiliary polyelectrolytes. The resulting coatings display structures in which copolymer I apparently serves as a template that controls the morphology adopted by the composite coatings. Coatings with structures very similar to that in Figure 4C developed when copolymer I was mixed with several different homopolyelectrolytes, an indication that the spontaneous tendency of copolymer I to form microphase-separated domains dictates the morphology of all coatings formed from mixtures of I and auxiliary polyelectrolytes. However, the auxiliary polyelectrolyte is not an inert component. Its presence is essential to produce highly swollen coatings that possess hydrophilic domains with electrochemically measured ion-exchange capacities much greater than those of copolymer I alone. Hydrophilic domains observed within composite coatings are approximately two orders of magnitude larger than those that have been reported for the rather dissimilar and relatively permselective polyelectrolyte Nafion.<sup>19</sup> The much more highly swollen nature of the composite coatings studied here and their larger domains may result in rather low permselectivity.

Mixing copolymer I with auxiliary polyelectrolytes also yields coatings that are much longer lived than those obtained from the auxiliary polyelectrolytes alone. The greater coating stability probably results from some form of association of the polymeric chains of the two components in composite coatings coupled with a *strong*

hydrophobic interaction between the electrode surface and the styrene groups of copolymer I.

The simultaneous attainment of good ion-retention properties and attractive charge propagation rates evident in Table I and Table II shows that a factor other than molecular scale interactions must be important for determining their electrochemical behavior. The strong correlation of composite coating morphology with electrochemical response led to the conclusion that the internal structure is the dominant factor controlling coating behavior. However, a two-domain structure alone is not adequate to ensure these attractive properties: Coatings prepared from copolymer I alone exhibit a two-domain structure (Figure 4B) but have much lower electrochemically measured ion-exchange capacities and retain incorporated polyvalent ionic reactants rather poorly when exposed to pure supporting electrolyte solutions (Table I). Thus, the presence of segregated domains within polyelectrolyte coatings appears to be a necessary but not sufficient condition for obtaining desirable coating behavior.

The idea that certain types of polyelectrolyte coatings on electrodes are comprised of two or more domains has been suggested in previous studies<sup>6a, 8</sup> and considerable evidence supporting a domain structure for Nafion membranes is available.<sup>19</sup> However, the notion introduced here is that useful domain structure can be induced in polyelectrolyte coatings by employing a polymer that exhibits a large driving force for microphase-separation as a template to control the morphology of coatings obtained from mixtures containing other components that have desirable properties. Hence, composite coatings in which templating polymers define coating morphology and auxiliary

polyelectrolytes establish an overall electrostatic and chemical environment for incorporated reactants offer a novel and flexible approach to the design of materials for polyelectrolyte electrode coatings that permits tailoring of coating properties to meet the specific requirements of different chemical systems.

An important question is whether or not polyelectrolyte electrode coatings offer advantages over other approaches for endowing electrodes with enhanced properties. In the case of electrocatalysis, for example, a polyelectrolyte coating must support substrate and product transport with diffusion coefficients of at least  $10^{-7} \text{ cm}^2 \text{ s}^{-1}$  to compete effectively against an electrode modified with a single monolayer of immobilized electrocatalyst. Sharp et.al., have employed a composite coating for the oxidation of catechol by incorporated  $\text{IrCl}_6^{3-}$  anions.<sup>25</sup> Although charge transport appeared to be rapid, the rate of substrate transport through the coatings was much too slow for effective use as an electrocatalytic system. Transport of dissolved gases (e.g.  $\text{O}_2$ ,  $\text{CO}_2$ ) may be much more facile, but studies of electrocatalytic systems acting on dissolved gases have been limited to Nafion coatings where charge transport is several orders of magnitude too slow for practical use. The utility of polyelectrolyte coatings for electrocatalysis is still an open question, but the weight of available evidence casts doubt on the eventual achievement of the necessary transport rates for both charge and chemical species within coatings.

## BIBLIOGRAPHY

1. (a) Oyama, N.; Anson, F.C. *J. Electrochem. Soc.* 1980, 127, 247.  
(b) *ibid* 1980, 127, 640.  
(c) Oyama, N.; Shinomura, T.; Shigehara, K.; Anson, F.C. *J. Electroanal. Chem.* 1980, 112, 271.  
(d) Oyama, N.; Anson, F.C. *Anal. Chem.* 1980, 52, 1192.
2. Faulkner, L.R. *Chem. Eng. News* 1984, 62, 29.
3. Majda, M.; Faulkner, L.R. *J. Electroanal. Chem.* 1984, 169, 77 and references cited.
4. Murray, R.W. in *Electroanalytical Chemistry* Bard, A.J., Ed.; Marcel Dekker: New York, 1984; Volume 13.
5. (a) Rubinstein, I.; Bard, A.J. *J. Am. Chem. Soc.* 1980, 102, 6641.  
(b) *ibid* 1981, 103, 5007.  
(c) Martin, C.R.; Rubinstein, I.; Bard, A.J. *J. Am. Chem. Soc.* 1982, 104, 4817.
6. (a) Shigehara, K.; Oyama, N.; Anson, F.C. *Inorg. Chem.* 1981, 20, 518.  
(b) Buttry, D.A.; Anson, F.C. *J. Electroanal. Chem.* 1981, 130, 333.  
(c) Buttry, D.A.; Anson, F.C. *J. Am. Chem. Soc.* 1982, 104, 4814.  
(d) Mortimer, R.; Anson, F.C. *J. Electroanal. Chem.* 1982, 138, 325.  
(e) Buttry, D.A.; Anson, F.C. *J. Am. Chem. Soc.* 1983, 105, 685.  
(f) Anson, F.C.; Ohsaka, T.; Saveant, J.-M. *J. Phys. Chem.* 1983, 87, 640.  
(g) Anson, F.C.; Saveant, J.-M.; Shigehara, K. *J. Am. Chem. Soc.* 1983, 105, 1096.  
(h) Anson, F.C.; Oshaka, T.; Saveant, J.-M. *J. Am. Chem. Soc.* 1983, 105, 4883.  
(i) Anson, F.C.; Saveant, J.-M.; Shigehara, K. *J. Electroanal. Chem.* 1983, 145, 423.  
(k) Andrieux, C.P.; Saveant, J.-M. *J. Electroanal. Chem.* 1978, 93, 163.  
(l) Braun, H.; Storck, W.; Doblhofer, K. *J. Echem. Soc.* 1983, 130, 807.  
(m) Lindholm, B.; Sharp, M. *J. Electroanal. Chem.* 1986, 198, 37.  
(n) Ugo, P.; Anson, F.C. *Anal. Chem.* in press.
7. (a) Bookbinder, D.C.; Bruce, J.A.; Dominey, R.N.; Lewis, N.S.; Wrighton, M.S. *Proc. Nat. Acad. Sci.* 1980, 77, 6280.  
(b) Bruce, J.A.; Wrighton, M.S. *J. Am. Chem. Soc.* 1982, 104, 75.
8. (a) Facci, J.; Murray, R.W. *J. Phys. Chem.* 1981, 85, 2870.  
(b) Facci, J.; Murray, R.W. *J. Electroanal. Chem.* 1981, 124, 339.  
(c) Murray, R.W. *Phil. Trans. Royal Soc., London* 1981, 302, 253.  
(d) Kuo, K.; Murray, R.W. *J. Electroanal. Chem.* 1982, 131, 37.

9. (a) Majda, M.; Faulkner, L.R. *J. Electroanal. Chem.* 1982, 137, 149.  
(b) *ibid.* 1984, 169, 97.
10. (a) Montgomery D.D.; Tsuchida, E.; Shigehara, K.; Anson, F.C.  
*J. Am. Chem. Soc.* 1984, 106, 7991.  
(b) Montgomery D.D.; Anson, F.C. *J. Am. Chem. Soc.* 1985, 107, 3431.
11. *Copolymerization* Ham, G.E., Ed.; Wiley-Interscience: New York, 1964.
12. Spialter, L.; Pappalardo, J.A. *The Acyclic Tertiary Amines* Macmillan: New York, 1965; p 14-29.
13. Morgan, P.W. *Condensation Polymers: By Interfacial and Solution Methods.* Wiley-Interscience: New York, 1965.
14. Sorenson, W.R.; Campbell, T.W. *Preparative Methods of Polymer Chemistry.* Wiley-Interscience: New York, second edition; 1968.
15. Daum, P.; Lenhard, J.R.; Rolison, D.; Murray, R.W. *J. Am. Chem. Soc.* 1983, 105, 1096.
16. Andrieux, C.P.; Dumas-Bouchiat, J.M.; Saveant, J.-M.  
*J. Electroanal. Chem.* 1982, 131, 1.
17. Oyama, N.; Nishiki, Y.; Tokuda, K.; Matsuda, H.; Anson, F.C.  
*J. Electroanal. Chem.* 1982, 139, 371.
18. von Slackelberg, M.; Pilgrim, M.; Toome, M. *Z. Elektrochem.* 1953, 57, 342.
19. Mauritz, K.A.; Hopfinger, A.J. in *Modern Aspects of Electrochemistry* Bockris, J. O'M.; Conway, B.E.; White, R.E., Eds.; Plenum Press: New York, 1982.
20. Dahms, H. *J. Phys. Chem.* 1968, 72, 362.
21. (a) Ruff, I. *Electrochim. Acta* 1970, 15, 1059.  
(b) Ruff, I.; Korosi-Odor, I. *Inorg. Chem.* 1970, 9, 186.  
(c) Ruff, I.; Friedrich, V.J. *J. Phys. Chem* 1971, 75, 3297, 3303.
22. (a) Shporer, M.; Ron, G.; Lowenstein, A.; Navor, G. *Inorg. Chem.* 1965, 4, 361.  
(b) Campion, R.J.; Deck, C.F.; King, P.; Wahl, A.C. *Inorg. Chem.* 1967, 6, 672.
23. Bradley, D.E. in *Techniques for Electron Microscopy* Kay, D.M., Ed.; Blackwell Scientific: Oxford, 1965; p. 66.
24. Malerba, D.E. private communication.

**CHAPTER 2**

## INTRODUCTION

Although the composite coating materials described in chapter 1 demonstrate the importance of film morphology for desirable coating behavior, they are not well-suited for detailed study of morphology effects because the internal domain structures they exhibit are poorly defined and difficult to control. To approach the study of morphological effects on coating behavior in a more rational fashion, coating materials with well-defined and controllable domain structures are required. Block copolymers are attractive materials for this purpose because they can often be cast to form membranes with well-defined internal morphologies. Further, internal structures adopted by coatings cast from block copolymers can be controlled by varying their chemical composition. This chapter describes some initial steps toward rational design of block-copolymer materials for polyelectrolyte electrode coatings.

Poly-L-lysine (PLL) offers several interesting features as an electrode coating<sup>1</sup> but the homopolymer is too water-soluble to yield robust and long-lived coatings. However, PLL-polystyrene block copolymers are known to adopt internal structures in cast membranes with separation of the hydrophobic and hydrophilic blocks into microdomains<sup>2</sup> and, in the work described here, they also were found to form stable electrode coatings. Thus, PLL-polystyrene block copolymers offer attractive model coating materials for exploring morphological effects on coating behavior more fully. Two different types of block copolymers (AB and ABA) were used here because it was of interest to know if they would form cast membranes with similar or

different internal morphologies and, if so, how these internal structures would influence the ion-exchange and electrochemical behavior of coatings cast from solutions of these block copolymers.

## EXPERIMENTAL

## Block Copolymer I.

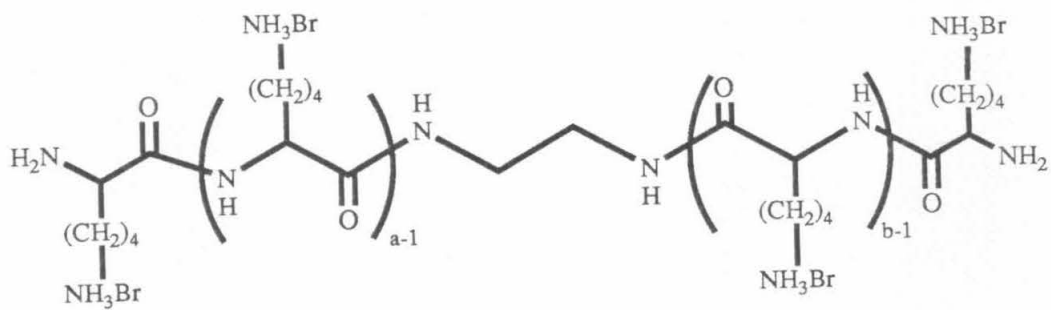
The preparation of the  $\alpha$ -N-carboxy anhydride of  $\epsilon$ -carbobenzoxy-L-lysine (NCA) followed published procedures<sup>3</sup> and NCA was recrystallized from dry ethyl acetate.

Poly( $\epsilon$ -carbobenzoxy-L-lysine) was prepared from the NCA monomer by a ring-opening polymerization initiated by 1,2-diaminoethane, yielding the poly-L-lysine (PLL) prepolymer with terminal amine groups (Figure 1a). The molecular weight was determined by gel permeation chromatography (Table I). The degree of polymerization,  $n$ , was calculated from the molecular weight.

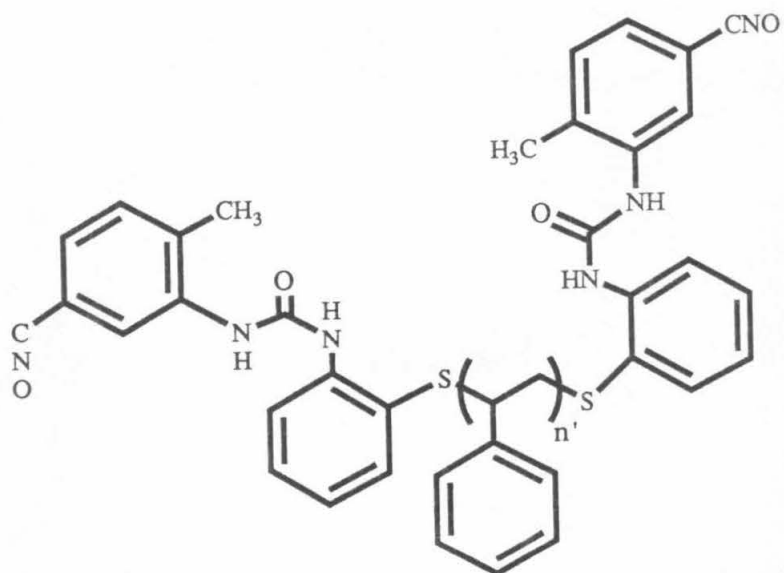
Telechelic polystyrene with terminal amine groups was prepared by the method of Costanza<sup>4</sup> employing bis(2-aminophenyl) disulfide as the chain-transfer agent and 2,2'-azobis(isobutylnitrile) (AIBN) as the initiator. The terminal amine groups of the resulting polystyrene were converted to terminal isocyanate groups by reaction with 2,4-toluene diisocyanate in dry benzene at ambient temperature for 2 hours, followed by reprecipitation from dry hexane to yield the polystyrene prepolymer (Figure 1B). Complete conversion of the terminal amine groups to isocyanates was confirmed by IR ( $-\text{NCO}$ ,  $2300\text{ cm}^{-1}$ ). The molecular weight was determined by vapor-phase osmometry (Hitachi VPO 117). The degree of polymerization,  $n'$ , was calculated from the molecular weight.

To prepare the AB type block copolymer, I (Figure 1C, Table I),  $5 \times 10^{-5}$  mol of amine end-groups attached to the PLL prepolymer ( $n = 17$ ) and  $5 \times 10^{-5}$  mol of terminal isocyanate groups attached to

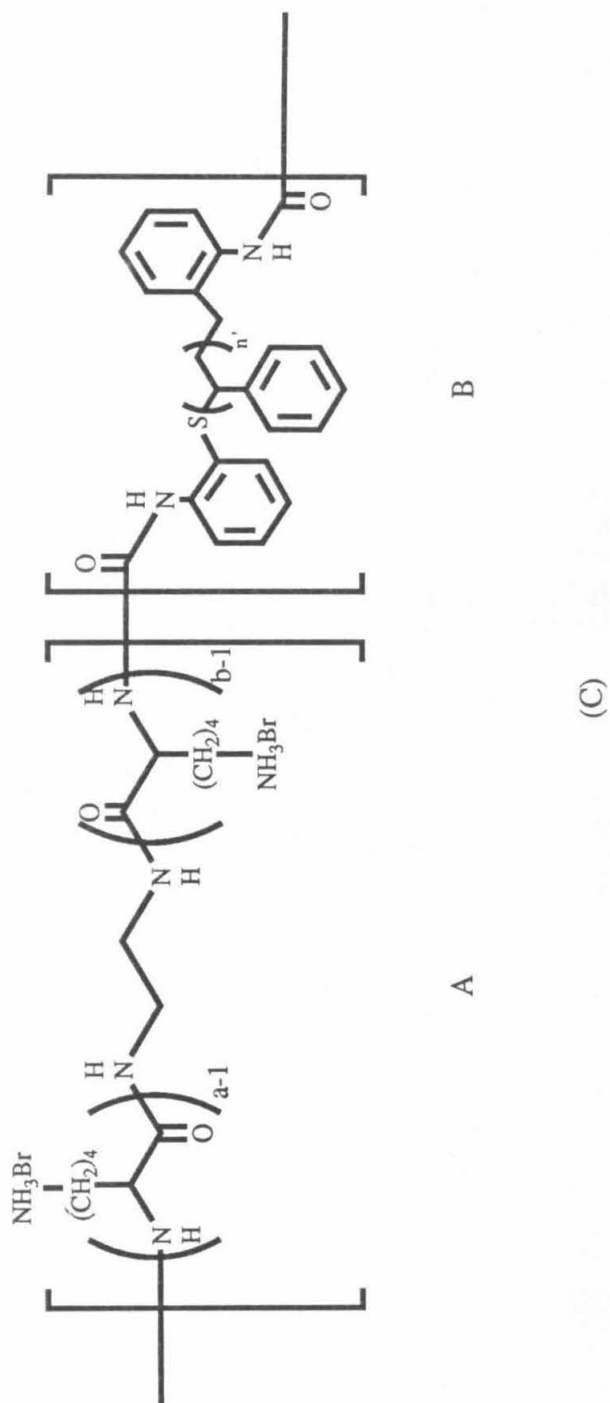
**Figure 1.** Structures of prepolymers and block copolymers used in this study. (A) Polylysine prepolymer. The degree of polymerization,  $n$  (*i.e.* the sum of  $a$  and  $b$ ), was calculated from the molecular weight determined by gel permeation chromatography. (B) Telechelic polystyrene prepolymer. The degree of polymerization,  $n'$ , was calculated from the molecular weight determined by vapor phase osmometry. (C) AB type block copolymer, I. (D) ABA type block copolymer, II. (E) ABA type block copolymer, III.



(A)



(B)



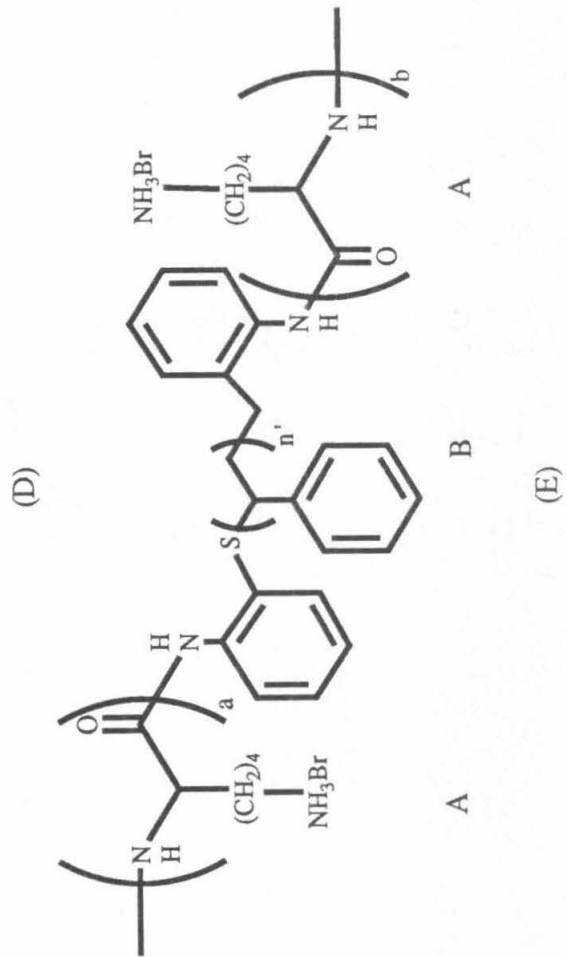
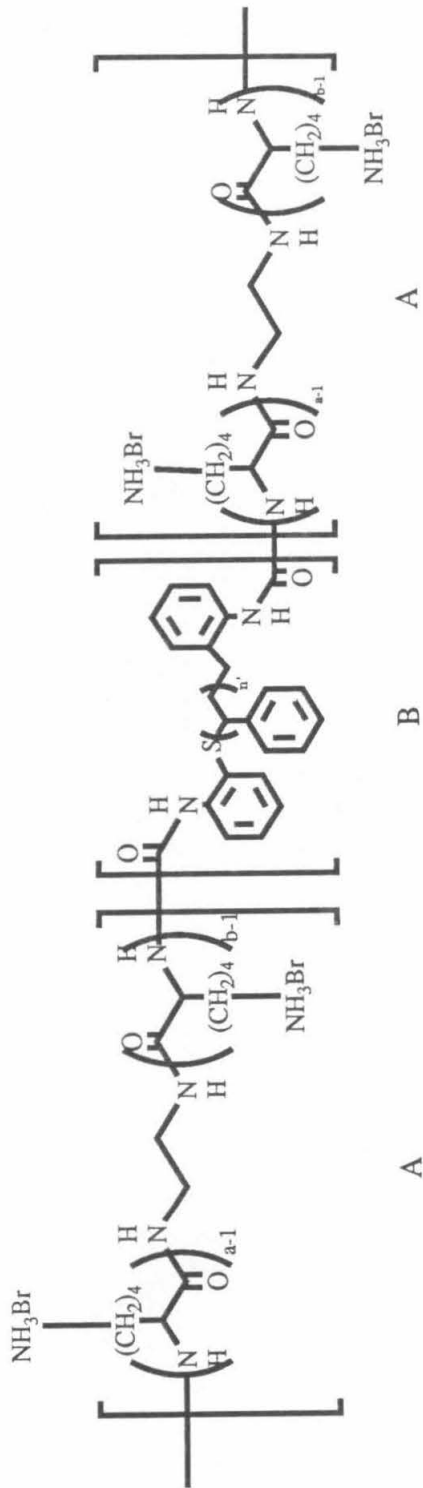


Table I

Composition of the Block Copolymers .

<u>Copolymer</u>	<u>Type</u>	<u>Degree of Polymerization<sup>a</sup></u>		<u>Lysine Residue<sup>b</sup></u>
		<u>PLL-Block</u>	<u>PSt-Block</u>	(Wt%)
I	AB	17	21	57.4
II	ABA	17	191	26.1
III	ABA	67 <sup>c</sup>	21	85.2

a. Determined by GPC (polylysine) or VPO (polystyrene).

b. Calculated from elemental analysis.

c. Average of both blocks as calculated from the measured lysine content (see experimental section).

the telechelic polystyrene prepolymer ( $n' = 21$ ) were dissolved in 100 ml of dry DMF and allowed to react for 10 days under a dry nitrogen atmosphere. The carbobenzoxy protecting group was removed from the lysine residues of the product by hydrolysis with a 20 wt.% solution of HBr in an acetic acid/anisole mixture (ca. 1:1 by volume). The deblocked copolymer, unreacted polystyrene prepolymers and deblocked PLL prepolymers came out of solution together as a white flocculent precipitate. This precipitate was dried and extracted with water using a soxhlet extraction apparatus to remove the residual PLL prepolymer. The precipitate was then washed with an aqueous 1 wt.% HBr solution followed by distilled water and then extracted with hot tetrahydrofuran (THF) to remove the residual polystyrene prepolymer. The remaining solid, block copolymer I, was washed with dry THF and dried in vacuo. The lysine content was determined by elemental analysis and confirmed by NMR.

#### Block Copolymer II.

Synthesis of the ABA-type block copolymer, II (Figure 1D, Table I), followed a procedure identical with that employed for block copolymer I, except that the degree of polymerization of the polystyrene prepolymer ( $n' = 191$ ) was about 11 times greater than the PLL prepolymer ( $n = (a + b) = 17$ ) (Table I). Under these conditions the reaction between the terminal amine groups on PLL blocks already attached to a large polystyrene block and the terminal isocyanate groups of other polystyrene blocks or prepolymers proceeded very slowly. As a result, the reaction of terminal isocyanate groups on polystyrene blocks with terminal amine groups on the much smaller and more mobile PLL prepolymers dominated.<sup>5</sup> Thus,

the overall reaction was effectively terminated at the ABA stage with little or no continued reaction to form AB-type copolymers. The lysine content of block copolymer II was determined by elemental analysis (Table I).

#### Block Copolymer III.

The NCA monomer (0.5 g) was dissolved in 100 ml of dry DMF that had been previously deaerated with nitrogen. The polymerization reaction was initiated by the addition of 0.1 g of the  $\alpha,\omega$ -diaminated polystyrene prepolymer ( $n' = 21$ ).<sup>6</sup> The reaction was allowed to proceed with stirring at 60 °C under an inert atmosphere for 6 days, whereupon the solution was concentrated in vacuo and added to dry diethyl ether to precipitate 0.41 g of the precursor to III. The carbobenzyoxy protecting groups on the lysine residues were removed as described for block copolymer I. The resulting ABA block copolymer (Figure 1e, Table I) was washed with a 1 wt.% aqueous HBr solution and extracted with hot THF to remove any residual polystyrene prepolymer. After extraction, block copolymer III was washed with dry THF and dried in vacuo. The lysine content was determined by elemental analysis (Table I). Because the degree of polymerization of the lysine blocks could not be determined in this case, the value listed in Table I reflects the average of both blocks calculated from the measured lysine content.

Poly(1-vinyl-2-methylimidazole), molecular weight =  $7 \times 10^4$  daltons, and other commercially available chemicals were used as received.

#### Apparatus and Procedures.

Glassy carbon electrodes (Tokai Carbon Co., Ltd.) having an area

of 0.282 cm<sup>2</sup> were mounted by sealing to a cylindrical stainless steel tube with heat-shrinkable polyolefin tubing (Alfa Wire Co.). They were then polished as previously described.<sup>7</sup> Electrode coatings were cast from 4  $\mu$ l of a 0.25 wt.% solution of the appropriate polymer in 1:1 (by volume) THF:water or pyridine:water, allowed to dry at room temperature until only slightly moist, and then warmed with a heat gun to ca. 80 °C for 30 seconds.

Cyclic voltammetry and coulometric measurements were conducted with conventional, previously described equipment and procedures.<sup>7, 8</sup> The supporting electrolyte solutions consisted of aqueous 0.2 M sodium acetate adjusted to pH 4.5 with glacial acetic acid. Solutions were deaerated with prepurified nitrogen. Potentials were measured with respect to a saturated calomel electrode (SCE). Experiments were performed at ambient temperatures (22  $\pm$  2 °C). The halide content of the block copolymers was determined by titration with silver ion.

Transmission electron microscopy (TEM) was carried out with a JOEL JEM-100CX instrument. Samples were prepared according to procedures described and discussed in the previous chapter.

Differential scanning calorimetry (DSC) was performed on samples of cast polymer membranes by co-workers at Waseda University. No experimental details are available.

## RESULTS

### A. Ion-Exchange Behavior.

The chemical structures of the three block copolymers examined in this study are specified in Figure 1. Block copolymer I (Figure 1C) is an AB-type block copolymer where A represents a PLL block and B a polystyrene block. In this block copolymer the A and B blocks contained 17 and 21 monomer units, respectively. Block copolymers II (Figure 1D) and III (Figure 1E) are ABA-type block copolymers composed of two A blocks for each B block. Block copolymer II was constructed from A blocks, each containing 17 lysine monomer units, separated by a B block containing 191 styrene monomer units. With block copolymer III the A blocks contained 67 lysine monomer units each and the B block contained 21 styrene monomer units.

Coatings of the block copolymers were cast onto the surfaces of glassy carbon electrodes and tested for their ability to accept and retain polyvalent counterions by ion-exchange. For purposes of comparison, the ion-exchange behavior of a simple homopolymer, poly(1-vinyl-2-methylimidazole) (PVI), was also evaluated. The testing protocol followed that employed in the previous chapter and consisted of measuring the steady-state ion-exchange capacity,  $4\Gamma_0/\Gamma_p$ , and a 45 minute retention ratio,  $\Gamma_{45}/\Gamma_0$  for each of the coating systems tested here. As before, the probe counterion was  $\text{Fe}(\text{CN})_6^{4-}$  incorporated by ion-exchange into coatings from a  $10^{-4}$  M aqueous electrolyte solution.

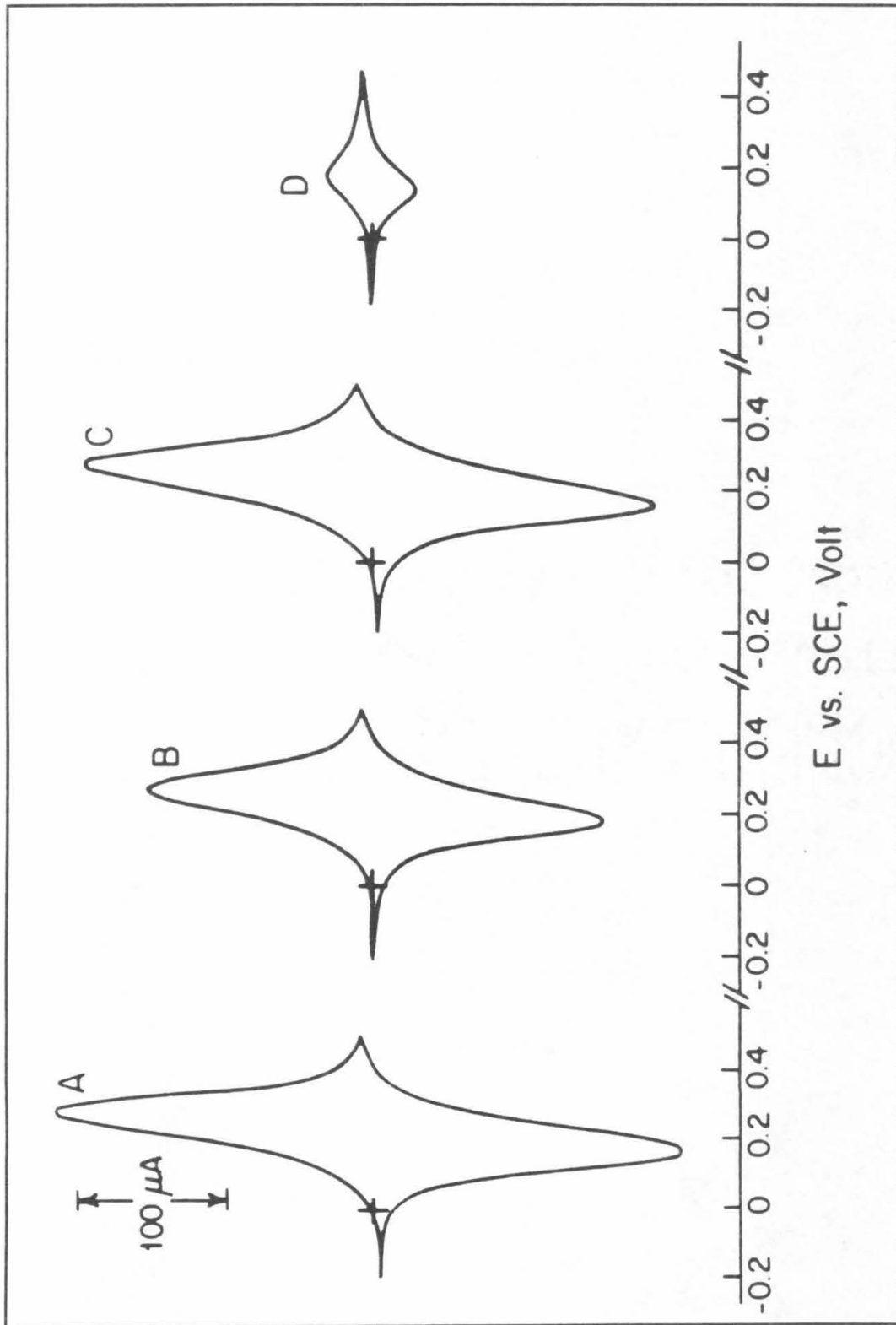
The interpretative and technical problems that accompany attempts to evaluate and explain charge propagation rates through

polyelectrolyte electrode coatings were discussed in detail in the previous chapter. Because such studies are of dubious merit, no effort was made here to evaluate effective rates of charge propagation through the coatings.

Cyclic voltammograms obtained with coatings of block copolymer I equilibrated with a 0.1 mM solution of  $\text{Fe}(\text{CN})_6^{4-}$  are shown in Figure 2. For comparison, a voltammogram for an electrode coated with PVI is also shown (curve D). The large peak currents obtained with coatings of block copolymer I exposed to the  $\text{Fe}(\text{CN})_6^{4-}$  solution (curves A through C) reflect the large ion-exchange capacity of this coating material (Table II). The ability of coatings formed from I to retain incorporated  $\text{Fe}(\text{CN})_6^{4-}$  anions when exposed to pure supporting electrolyte solutions is displayed in curve B. Comparison of curve A and curve C indicates that the block copolymer is not lost from the surface of the electrode during the 45 minute period prior to recording curve B. Thus, the decrease in peak current that occurs after immersing the coating in a pure supporting electrolyte solution for 45 minutes is a consequence of  $\text{Fe}(\text{CN})_6^{4-}$  leaching out of the polyelectrolyte coating and is not due to the loss of coating material from the electrode surface. The much smaller response obtained from the PVI coating that contained half again as many positive charge sites (curve D) demonstrates the superiority of block copolymer I over simple homopolyelectrolytes as an electrode coating material for incorporating and retaining multiply-charged and electroactive counterions.

A summary of the quantitative data obtained with electrode coatings prepared from the three block copolymers in Figure 1 is

**Figure 2.** Steady-State cyclic voltammograms for  $\text{Fe}(\text{CN})_6^{4-}$  incorporated within the PLL-PSt block copolymer I and PVI coatings on a glassy carbon electrode ( $0.283 \text{ cm}^2$ ). Coating compositions: (A, B, C) I; (D) Pure PVI. Curves A and D were recorded after the coatings had equilibrated with the  $0.1 \text{ mM Fe}(\text{CN})_6^{4-}$  solution and the peak currents had stabilized. Curve B was recorded 45 minutes after the coating was transferred to pure supporting electrolyte. Curve C was recorded immediately after the coating was transferred back to the original solution of  $\text{Fe}(\text{CN})_6^{4-}$ . Scan rate:  $100 \text{ mVs}^{-1}$ . Supporting electrolyte:  $0.2 \text{ M acetate buffer (pH 4.5)}$ .



E vs. SCE, Volt

presented in Table II. The two ABA-type block copolymers, II and III, can be seen to yield coatings with inferior properties compared to the AB type block copolymer I. Block copolymer II shows only about half the steady-state ion-exchange capacity of block copolymer I, although it is still much higher than that of the PVI coating. Anion retention by coatings cast from block copolymer II is unimpressive. Block copolymer III, with its high lysine content (85%), was too soluble in aqueous media to yield stable coatings. Thus, the very small value of  $4\Gamma_0/\Gamma_p$  for block copolymer III in Table II is more a reflection of the detachment of the polymer from the surface than of its intrinsic ion-exchange capacity.

On the basis of their chemical compositions alone, the large differences in the behavior of the three block copolymers is difficult to explain. However, the work on composite coatings described in chapter 1 as well as other studies in these laboratories by Sumi and Inoue<sup>9</sup> have underscored the important role internal structure plays in establishing long-term stability, ion-exchange capacity and electrochemical behavior of coatings cast from solutions of copolymers that contain both hydrophilic and hydrophobic groups. Further evidence suggesting that morphologic differences may be important for understanding the behavior of the coating materials described here is the large effect produced by changing the solvent mixture from which the coatings are cast. Both the incorporation and retention of  $\text{Fe}(\text{CN})_6^{4-}$  by coatings of block copolymer I decrease when the casting solvent is changed from THF-H<sub>2</sub>O to pyridine-H<sub>2</sub>O (Table II). With the THF-H<sub>2</sub>O solvent mixture, the hydrophobic polystyrene blocks probably separate from the casting solution before the water soluble PLL blocks

Table II

Steady-State Anion Exchange Capacities and Retention Ratios for  
Fe(CN)<sub>6</sub><sup>4-</sup> Incorporated in Polycationic Coatings on Glassy Carbon  
Electrodes .

Coating Material <sup>a</sup> (Copolymer)	10 <sup>8</sup> $\Gamma_p^b$ (mole cm <sup>2</sup> )	10 <sup>8</sup> $\Gamma_o^c$ (mole cm <sup>2</sup> )	4 $\Gamma_o/\Gamma_p^d$	$\Gamma_{45}/\Gamma_o^e$
I	8.1	1.2	0.59	0.79
I	9.7	1.4	0.51	0.78
I	19.4	3.0	0.58	0.78
I <sup>f</sup>	9.7	0.67	0.28	0.49
II	4.4	0.35	0.32	0.26
III	14.4	0.13	0.04	0.29
PVI <sup>g</sup>	15.5	0.39	0.10	0.54

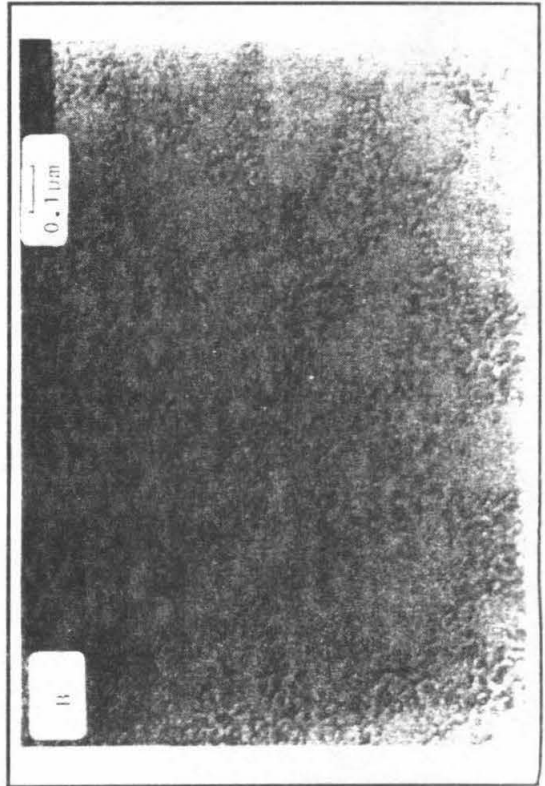
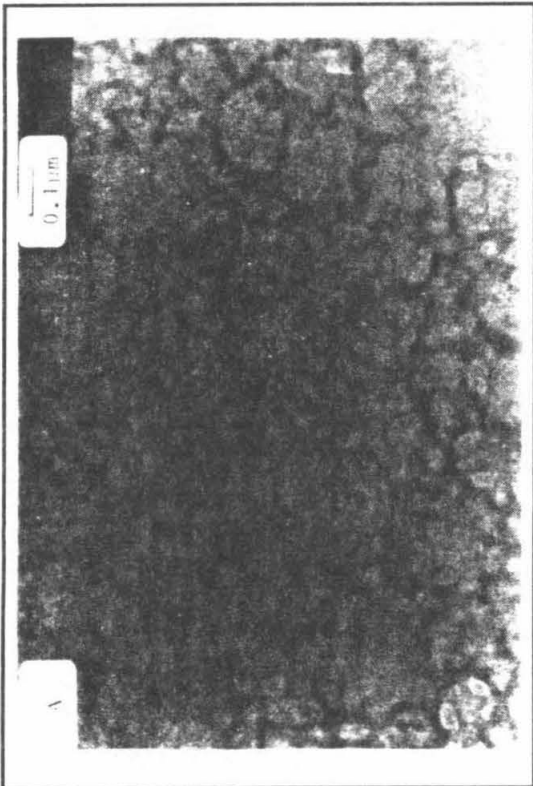
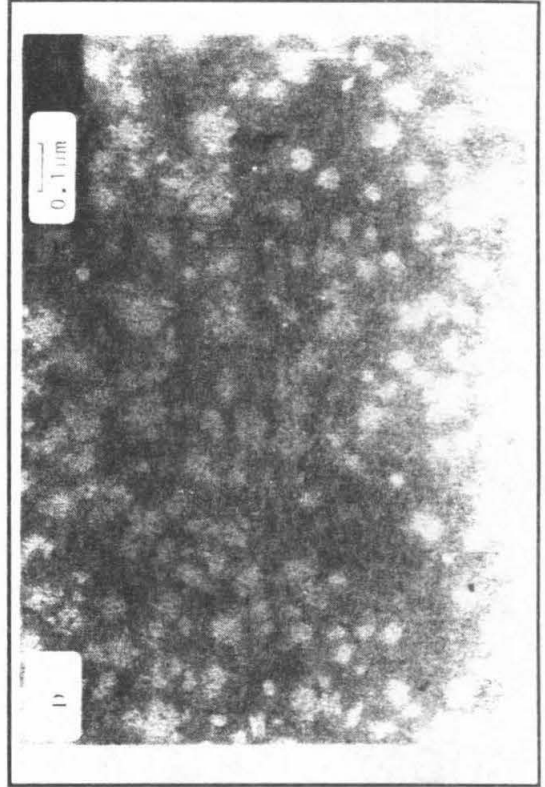
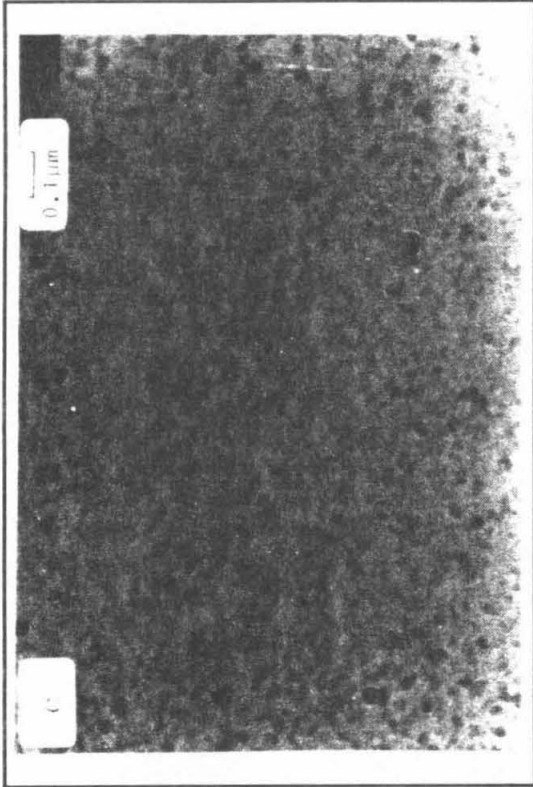
- a. See Figure 1; PVI = poly(N-vinyl-2-methylimidazole). All coatings were cast from 1:1 (by volume) THF:H<sub>2</sub>O except where noted.
- b. Calculated total quantity of cationic sites in the electrode coating.
- c. Quantity of Fe(CN)<sub>6</sub><sup>4-</sup> incorporated by the coating upon equilibration with a 0.1 mM Fe(CN)<sub>6</sub><sup>4-</sup> solution as measured coulometrically immediately after transfer to pure supporting electrolyte solution.
- d. Fraction of the cationic sites occupied by Fe(CN)<sub>6</sub><sup>4-</sup> anions.
- e. Retention Ratio: Fraction of the initially incorporated Fe(CN)<sub>6</sub><sup>4-</sup> anions that remained after 45 minutes of exposure to pure supporting electrolyte (0.2 M acetate buffer, pH 4.5).
- f. Coating cast from 1:1 pyridine:H<sub>2</sub>O.
- g. Coating cast from methanol.

because the more volatile THF evaporates from the solvent mixture more rapidly than water. As a consequence, the hydrophilic PLL blocks may be constrained to occupy narrow domains within the coating interior that remain after the hydrophobic polystyrene blocks have separated from the casting solution. The density of fixed cationic charge sites within these hydrophilic domains could become very large. However, with the pyridine-H<sub>2</sub>O casting solvent mixture the organic component evaporates after the water and the converse behavior is anticipated. Thus, less densely concentrated hydrophilic domains may result that could be partially isolated from the electrode surface by insulating hydrophobic domains that are formed later in the evaporation process.

#### B. Transmission Electron Microscopy.

To evaluate these conjectures and to inspect internal coating morphologies more closely, transmission electron micrographs were obtained from films of the three block copolymers that were stained with IrCl<sub>6</sub><sup>2-</sup> (Figure 3). The micrograph of block copolymer I (Figure 3A) exhibits an internal morphology that suggests microphase-separated domains in which the stained lysine residues form a narrow network structure surrounding the polystyrene domains that appear as large (ca. 0.3 μm) and irregular islands. One notable feature of this micrograph is the small relative area occupied by the dark lysine residues that comprise nearly 60 wt.% of the block copolymer. As noted above, this may be the result of a compression in the solid state of the PLL domains by the large polystyrene island structures that form due to rapid evaporation of THF from the casting solvent mixture.

Figure 3. Transmission electron micrographs of polyelectrolyte coatings on carbon-coated copper minigrids. Preparation of samples is given in the experimental section. (A) AB-type block copolymer I cast from 1:1 (by volume) THF:H<sub>2</sub>O; (B) AB-type block copolymer I cast from 1:1 (by volume) pyridine:H<sub>2</sub>O; (C) ABA-type block copolymer II; (D) ABA-type copolymer III.



Coatings cast from both of the ABA block copolymers (II and III) display morphologies that differ notably from that adopted by the AB block copolymer I. Micrographs of block copolymer II (Figure 3C) and block copolymer III (Figure 3D) exhibit homologous microphase-separated structures in which the minority component of the block copolymer forms small isolated islands of relatively uniform geometry and size dispersed within a matrix of the majority component. In contrast with block copolymer I, the relative areas occupied by the minority and majority components in copolymers II and III are approximately consistent with their mole fraction in the block copolymers.

Additional evidence for the presence of a microphase-separated structure within the block-copolymer coatings was provided by differential scanning calorimetric measurements of the glass transition temperatures,  $T_g$ , of films cast from solutions of the three block copolymers and of their prepolymers (Table III).  $T_g$  values for the  $\alpha,\omega$ -diaminated polystyrene ( $n' = 21$ ) and PLL ( $n = 17$ ) prepolymers were 90 and 168 °C, respectively. All three of the block copolymers exhibited a pair of glass transition temperatures, the first near 100 °C and the second ranging from 135 °C for II and III to ca. 141 °C for I. The appearance of two transitions at temperatures between the values obtained for the two prepolymers is consistent with the presence of microphase-separated morphologies in block copolymers.<sup>10</sup>

### C. Discussion.

The micrographs in Figure 3 and the data in Table III support the hypothesis that all three of the block copolymers examined here adopt

Table III

Glass Transition Temperatures of Polymer Coating Materials.

Coating Material	$T_{g_1}$ ( $^{\circ}\text{C}$ )	$T_{g_2}$ ( $^{\circ}\text{C}$ )
Block Copolymer I	100	141
Block Copolymer II	100	135
Block Copolymer III	100	135
Polystyrene Prepolymer	90	-
Polylysine Prepolymer	-	168

microphase-separated structures when cast as coatings. That the coatings nevertheless behave very differently in electrochemical experiments demonstrates that microphase-separated domains are not sufficient to obtain the desirable properties exhibited by coatings of block copolymer I. Differences in detail between different microphase-separated structures within coatings are evidently crucial. A factor contributing to the superior properties of coatings prepared from solutions of block copolymer I may be the apparent compression of lysine residues into narrow channels that would tend to increase the local concentration of cationic sites responsible for ion-exchange. Higher concentrations of immobilized charge sites also may assist in the retention of incorporated anions.

A second structural feature of importance is the continuity of the PLL phase found with coatings cast from block copolymer I (Figure 3A). This contrasts with the more discreet and isolated PLL domains found in coatings prepared from block copolymer II (Figure 3C). Physical isolation of portions of the lysine residues could decrease the measured ion-exchange capacity because of the lack of a continuous ionic pathway to the electrode surface that is required for electroactivity of the incorporated  $\text{Fe}(\text{CN})_6^{4-}$  anions.

The micrograph in Figure 3D of a coating prepared from block copolymer III shows an internal structure that has a polystyrene phase dispersed as small and irregular islands throughout a PLL matrix. Because the PLL matrix should be soluble, the instability of coatings cast from block copolymer III is consistent with the solid state internal morphology observed by TEM. In the micrographs of coatings cast from block copolymers I and II, the hydrophobic polystyrene phase

appears to occupy the majority of coating volume and is therefore likely to help bind the coating to the glassy carbon electrode surface by hydrophobic bonding.

The changes in coating stability and ion-exchange capacity that accompany a change in casting solvent, *vide supra*, are matched by changes in solid state coating morphology as observed by TEM. This can be seen by comparing the micrograph of a coating of block copolymer I that was cast from a pyridine-H<sub>2</sub>O solvent mixture (Figure 3B) with that obtained when the casting solvent was THF-H<sub>2</sub>O (Figure 3A). The micrograph in Figure 3B shows that the coating cast from pyridine-H<sub>2</sub>O displays a microphase-separated structure that is distinctly different from that obtained from the THF-H<sub>2</sub>O solvent mixture. The narrow and well-defined PLL network evident in Figure 3A is replaced in Figure 3B with a wide and diffuse band that surrounds a series of large irregular polystyrene islands. The relative area occupied by the PLL phase in the micrograph has increased several fold so that the local concentration of lysine residues may have decreased substantially. Thus, the smaller values for incorporation and retention of  $\text{Fe}(\text{CN})_6^{4-}$  by the coating of block copolymer I that was cast from pyridine-H<sub>2</sub>O (Table II) can be at least partially understood on the basis of the TEM micrographs.

The possibility that structural features revealed in TEM micrographs of thin, dry films may not apply to swollen polymer coatings was examined by varying the thicknesses of coatings. If the properties of the coatings close to the electrode surface differed from those in the bulk of the film, then those properties should depend on coating thickness. However, as the data in Table II show,

coatings of block copolymer I retain their desirable properties over a 2.5-fold range in thickness indicating that the observed electrochemical behavior of these coatings are intrinsic to the block copolymer material and the casting conditions and do not depend upon specific interaction with an electrode surface.

#### SUMMARY.

The research discussed in this chapter was directed toward a more refined understanding of how the internal morphology of polyelectrolyte electrode coatings influence their electrochemical response. This work builds on and extends the observations discussed in chapter 1 that demonstrate the importance of a microphase-separated internal structure for long-term coating stability, ion-exchange capacity and electrochemical behavior. Toward this end, the research described in this chapter had the primary goal of synthesizing block copolymer electrolytes that could adopt microphase-separated and well-defined internal morphologies. A secondary goal was to establish experimentally the assertion that coating morphology can be manipulated in a controlled and rational fashion by adjusting the chemical composition of block-copolymer electrolytes.

Incorporation of a polymer electrolyte material (*i.e.*, PLL) that is too soluble as a homopolymer for use as an electrode coating into a block copolymer, was shown to be a strategy useful for stabilizing the polyelectrolyte and allowing it to be employed as a medium for sequestering electroactive counterions within an electrode coating. Although this approach is much less facile than the composite coating technique, the coating materials prepared in this fashion form

membranes that have reasonably well-defined internal morphologies. The internal structures of coatings formed from these materials also can be manipulated reproducibly by changes in casting solvent and the chemical composition of the block copolymer. Block copolymers of the AB type were found to yield electrode coatings that were superior to those cast from solutions of ABA-type copolymers and a PVI homopolymer. Also, use of an organic component in the aqueous casting solvent, which is more volatile than water, was shown to be important for good coating behavior.

Close inspection of TEM micrographs of thin and dry membranes cast from solutions of the block copolymers employed here and stained to reveal features due to hydrophilic domains within the coatings pointed to several morphologic features associated with better coating materials. In particular, internal structures such as that displayed by coatings of I, which force hydrophilic components to occupy narrow domains, appear to offer the best electrochemical response. Disruption of this structure by changes in the casting solvent causes a marked degradation of electrode coating performance.

The proposition advanced in chapter 1 that coating morphology is the dominant factor for determining the electrochemical response of polyelectrolyte electrode coatings has been lent further support by the block copolymer materials examined here. The capacity for design of coating materials to examine morphologic features that contribute to desirable performance characteristics has been demonstrated by block copolymer I. Furthermore, comparison of coatings formed from block copolymers I, II and III supports the hypothesis that coating morphology can be controlled by changes in the chemical composition of

a given polyelectrolyte material. Before the design of polyelectrolyte coating materials can be approached in a rational fashion the difficult problem of correlating morphological features with coating behavior must be addressed. Because the internal structures adopted by coatings of block copolymers can be controlled by varying their chemical composition it is reasonable to assume that they will prove increasingly useful for developing electrode coating materials with specifiable properties.

## BIBLIOGRAPHY

1. (a) Anson, F.C.; Ohsaka, T.; Saveant, J.-M. *J. Phys. Chem.* 1983, 87, 640.  
(b) Anson, F.C.; Saveant, J.-M.; Shigehara, K. *J. Am. Chem. Soc.* 1983, 105, 1096.  
(c) Anson, F.C.; Ohsaka, T.; Saveant, J.-M. *ibid.* 1983, 105, 4883.  
(d) Anson, F.C.; Saveant, J.-M.; Shigehara, K. *J. Electroanal. Chem.* 1985, 145, 423.
2. (a) Gallot, B. *Adv. Polym. Sci.* 1978, 29, 87.  
(b) Gallot, B.; Douy, A.; Billot, J.-P. *Makromol. Chem.* 1977, 178, 1641.
3. (a) Blout, E.R.; Karlson, R.H. *J. Am. Chem. Soc.* 1956, 78, 941.  
(b) Baizer, M.M.; Clark, J.R.; Swindinsky, J. *J. Org. Chem.* 1957, 22, 1595.  
(c) Fuller, W.D.; Verlander, M.S.; Goodman, M. *Biopolymers* 1976, 15, 1869.
4. Costanza, A.J.; Coleman, R.J.; Pierson, R.M.; Marvel, C.S.; King, C. *J. Polym. Sci.* 1955, 17, 319.
5. Elias, H.-G. *Macromolecules*, 2nd ed., Plenum: New York, 1984; Vol. 2, p. 765.
6. (a) Lundberg, R.D.; Doty, P. *J. Am. Chem. Soc.* 1957, 79, 3961.  
(b) Tsuchida, E.; Hasegawa, E.; Honda, K. *J. Polym. Sci. Polym. Chem. Ed.* 1975, 13, 1747.  
(c) Hasegawa, E.; Shibata, T.; Tsuchida, E. *Eur. Polym. J.* 1977, 13, 669.
7. Oyama, N.; Anson, F.C. *J. Electrochem. Soc.* 1980, 127, 640.
8. Oyama, N.; Anson, F.C. *Anal. Chem.* 1980, 52, 1192.
9. (a) Sumi, K.; Anson, F.C. *J. Phys. Chem.* 1986, 90, 3845.  
(b) Inoue, T.; Anson, F.C. *J. Phys. Chem.* 1987, 91, 1519.
10. (a) Bares, J. *Macromolecules* 1975, 8, 244.  
(b) Krause, S.; Iskandar, M. In *Multiphase Polymers*, Cooper, S.L.; Estes, G.M., Eds.; American Chemical Society: Washington, DC, 1979; Adv. Chem. Ser. No. 176, p. 205.  
(c) Inoue, T.; Ogata, S.; Kakamoto, M.; Imai, Y. *Macromolecules* 1984, 17, 1417.

**CHAPTER 3**

## INTRODUCTION

The conventional approach to the phenomenological analysis of the electrified interphase by global equilibrium thermodynamics was developed in 1942 by Grahame and Whitney who adopted the dividing-surface model of Gibbs<sup>1</sup> and coined the term "ideal polarizable electrode" as a label for their system.<sup>2</sup> However, this analysis requires an extension of Guggenheim's operational definition of "electrochemical" potential<sup>3a, b, 10</sup> to the electrified interphase where it is not appropriate because the chemical composition of the interphase is not identical to that of the bulk phases with which it is in equilibrium (*vide infra*). Prigogine and co-workers have demonstrated that the use of a Gibbs model for electrified interphases is not allowed at a fundamental level because the free energy of the interphase depends upon the non-isotropic distributions of chemical species within the interphase.<sup>4</sup> Therefore, the direct use of global observables (e.g., charge densities, electrostatic potential, chemical composition of bulk phases) to define the state of the interphase is precluded because local information about the distribution of chemical species within an electrified interphase is required. Further, it can be shown that there are pathological features inherent to the use of a dividing-surface model that lead to the prediction of infinite electric fields within the interphase for systems that employ an electrostatic potential as an electric state variable (Appendix I). Thus, the conventional analysis that leads to important thermodynamic relations such as the electrocapillary equation and the Lippmann equation is formally incorrect, although these equations may serve as

good approximations in special cases. These problems are not mentioned in the pedagogical literature of electrochemistry<sup>5</sup> and, with the exception of a small school of physical electrochemists, have not been recognized as an important element for the analysis of interfacial processes at electrodes. Nevertheless, a more correct and general phenomenological analysis of the electrified interphase has been developed using local non-equilibrium thermodynamics.<sup>4 a-d, 7, 9, 10, 11, 14</sup> The material in chapter 4 will employ elements of a local and non-equilibrium analysis and it is the paucity of this genre of analysis in the electrochemical literature that motivates the inclusion of this chapter.

### Conditions for the Existence of a Separable Electrified Interphase.

The electrified interphase is a local element of a larger global electrochemical system constructed from at least two bulk phases. Electrochemical observables are global quantities and for global observables to provide a connection between thermodynamic functions and local state variables, the interphase must behave like a discreet and "autonomous" phase<sup>6</sup> that is sandwiched between the bulk phases. This requires two approximations. First, that an independent equation of state can be written for the interphase that contains no contributions to the free energy from any bulk phase.<sup>6,7</sup> Second, because a global thermodynamic description of the interphase assumes that all state variables are independent of the space-time coordinates of a system, the temperature, pressure and chemical potential within the electrified interphase must be isotropic.

These assumptions are problematic, in general, because the behavior of condensed matter within electromagnetic fields does not lend itself to a straightforward analysis that is compatible with the requirements of isotropy and autonomy. Large gradients in the electromagnetic field, electric polarization, chemical potential and pressure may exist across an electrified interphase at equilibrium.<sup>4e, 8a, b</sup> Thus, state variables, especially the chemical potential, must be defined carefully to satisfy isotropy requirements. Further, electrostatic energy is not necessarily conserved and, unlike other extensive quantities, cannot be partitioned.<sup>4c, 8</sup> Therefore, an electrified interphase, by definition, must contain all relevant charges and all external field energy out to infinity to satisfy the

conditions for autonomy.<sup>4d, e, 6d, 7, 9</sup> Otherwise, the free energy of the interphase,  $F^\alpha$ , will be a function of the state of adjoining phases. This condition for autonomy cannot be met formally by any local system of finite size, but most common electrodes are of sufficient size to ensure that residual external energy is unimportant and the interphase can be treated as an autonomous phase. The problem of developing operational definitions for isotropic state variables is more serious and a comprehensive discussion will require local thermodynamics.

#### Isotropic State Variables.

The general conditions for a system to be in statistical equilibrium are that gradients of temperature, pressure and chemical potential throughout the system vanish (e.g.  $\nabla T = \nabla p = \nabla \mu_i = 0$ ). The global system observed with an electrochemical experiment consists of at least two bulk phases and an electrified interphase. The problem, simply stated, is that the electrified interphase has one more degree of freedom than adjoining bulk phases. The proper independent variables for the free energy of an electrified interphase are  $T^\alpha$ ,  $V^\alpha$ ,  $n_i^\alpha$  and  $P^\alpha$  whereas those for the free energy of the bulk phases are  $T^\beta$ ,  $V^\beta$  and  $n_i^\beta$  and common operational definitions of  $T$ ,  $p$  and  $\mu_i$  that have been developed for bulk systems in the absence of an external field must be modified extensively to maintain their utility at the electrified interphase.<sup>7</sup> For example, the chemical potential is a function of temperature, pressure and the density,  $\rho_i^\beta$ , of some species  $i$  in some phase  $\beta$  in the absence of a field (e.g.  $\mu_i^\beta = f(T, p^\beta, \rho_i^\beta)$ ). However, at an electrified interphase there must exist gradients in  $\rho_i^\alpha$  for any ionic species in order to establish

an electric field. Thus, any  $\mu_1^\alpha$  that is defined as some  $f(T, p^\alpha, \rho_1^\alpha)$  will also have a non-zero gradient across the interphase and will not meet the required chemical equilibrium condition. A useful operational definition of  $\mu_1^\alpha$  for an electrified interphase will require  $\mu_1^\alpha = f(T, p^\alpha, \rho_1^\alpha, P^\alpha)$ , *vide infra*, such that  $\nabla\mu_1^\alpha = 0$  across the interphase. Both  $T$  and  $p^\alpha$  also need modified operational definitions that include electric field and polarization effects. Note that the global electrostatic potential of the electrochemical cell that is measured in electrochemical experiments is not a useful variable for describing the electrical contribution to the state of an electrified interphase of finite thickness because the electrostatic potential is not constant across the interphase. However, local values of the electrostatic potential within small volume elements inside the interphase are useful, *vide infra*, but cannot be measured directly.

The need for an alternative operational definition of  $\mu_1^\beta$  for ionic species in the presence of an electric potential was recognized by Gibbs<sup>3c</sup> and an expression first formulated by Guggenheim based on his intuition about its form.<sup>3a, b</sup> Because the number of excess free ions necessary to establish an electric potential difference between two adjoining bulk electrolyte phases is infinitesimal relative to the concentration of electrolyte, Guggenheim could assume to a very good degree of precision that two bulk phases of identical chemical composition could be endowed with different electric potentials. For example, to establish a potential difference of one volt between two electrolyte phases would require only *ca.*  $10^6$  excess free ions (*e.g.*  $10^{-17}$  M) per  $\text{cm}^2$  of interfacial area. This corresponds to an error of one part in  $10^{16}$  for 0.1 M electrolyte solutions. Thus,

given the condition that two phases are of identical chemical composition, Guggenheim proposed that the difference in chemical potential for any ionic species jointly present in both phases was simply proportional to the difference between the scalar electric potential of phase 1 and phase 2, e.g.;

$$\mu_i^1 - \mu_i^2 = z_i F(\phi_1 - \phi_2)$$

or

$$\mu_i^1 = \mu_i^2 + z_i F\Delta\phi$$

where  $z_i$  is the charge on ionic species  $i$  and  $F$  is the faraday (96484.56 C/mol). If  $\phi_2$  is taken to be zero, then one obtains the most popular operational definition of electrochemical potential;

$$\tilde{\mu}_i^\beta = \mu_i^\beta + z_i F\phi_\beta \quad (1)$$

where  $\mu_i^\beta$  is the conventional chemical potential of ionic species  $i$  in phase  $\beta$  (e.g.  $\mu_i^\beta = {}^\circ\mu_i^\beta(T, p^\beta) + RT \ln \gamma_i x_i$ ). However, as Guggenheim and others have pointed out emphatically,<sup>3a, b, 4, 7, 10</sup> the equilibrium condition is  $\nabla \tilde{\mu}_i^\beta = 0$  and the proposed electrochemical potential function is an approximation that is valid formally only in the trivial case where  $\Delta\phi = 0$ .

Equation (1) is used almost universally as an operational definition of chemical potential for electrified interphases.<sup>5</sup> This is a muddled enterprise at best because the approximations Guggenheim employs for bulk systems break down at electrified interphases.<sup>7, 10</sup> First, the assumption of identical chemical composition between the interphase and the bulk is unambiguously incorrect. Relative surface

excess quantities of ionic species within an electrified interphase can be 20-30 times larger than or smaller than their bulk values.<sup>5</sup> Even at the electrocapillary maximum (ECM) there are often appreciable relative surface excesses of ionic species. When the chemical compositions of two phases are not identical, the most that can be said is that  $\tilde{\mu}_1^\alpha = \tilde{\mu}_1^\beta$ . Second, with the possible exception of the ECM,  $\phi_\alpha$  is not constant across an electrified interphase of finite thickness. It is seen from equation (1) that if  $\phi_\alpha$  is not constant, then  $\tilde{\mu}_1^\alpha$  is not isotropic and the condition for chemical equilibrium is violated.

One technique that is employed frequently to avoid these problems partitions the interphase into very thin laminar phases such that  $\phi_\alpha$  is constant within the phase and adjoining lamina are nearly identical in chemical composition.<sup>4, 5, 11</sup> However, within the context of global thermodynamics this construction is not allowed because such laminar phases are not autonomous.<sup>4, 7</sup> This model also requires small step functions in  $\phi_\alpha$  at the boundaries of each lamina, which give rise to infinite electric fields in the same fashion as the Gibbs dividing-surface model (Appendix I). The most common approach is to adopt a Gibbs definition for the electrified interphase and regard it as an infinitesimally thin "dividing-surface" with uniform chemical composition.<sup>1, 2, 5</sup> A Gibbs model does not ensure that the interphase and the bulk phases are of identical chemical composition and, in general, is not allowed for electrochemical systems because the thermodynamic properties of electrified interphases depend upon the spatial distribution of electric charge and chemical species.<sup>4, 7, 8a</sup> The Gibbs model also requires the existence of infinite electric

fields within the interphase (Appendix I), but this is a less serious problem than the need to account for local distributions of chemical species. Thus, it appears that an operational definition of electrochemical potential useful for electrified interphases has not been developed within the context of global thermodynamics.

The inability of global thermodynamics to provide a framework for developing operational definitions of isotropic state variables for the electrified interphase arises because the existence of an electric field within a phase requires that  $\nabla\phi_\alpha$  be non-zero.<sup>4,7,8a,10</sup> Because the distribution of ionic species establishes the electric field for electrochemical systems, these distributions are also not isotropic. Therefore, because any attempt to establish a global operational definition of an electrochemical or chemical potential for some species  $i$  within an autonomous phase must assume *a priori* that the distribution of species  $i$  is isotropic, a global operational definition of electrochemical potential for any interfacial system that bounds bulk systems with different electrostatic potentials is not possible. Similar problems also arise for global operational definitions of the temperature and the pressure within an electrified interphase.<sup>8a</sup>

#### Local Thermodynamics.

As is evident from the material presented in the previous section, myriad problems arise naturally when a thermodynamic formalism that assumes state variables are independent of the space-time coordinates of a system is applied to heterogeneous media. The short-comings of global thermodynamics have been recognized and

addressed explicitly since the middle of the nineteenth century<sup>12</sup> and a mature local thermodynamics has been extant for nearly fifty years.<sup>13</sup> The local formulation of thermodynamics was motivated by the need for analysis of non-equilibrium and irreversible processes, but is also useful for the description of heterogeneous systems at equilibrium because both the problem of autonomy and of isotropic state variables become more tractable.

A comprehensive treatment of the electrified interphase and electrochemical kinetics within the context of non-equilibrium thermodynamics has been available since the early 1950's.<sup>10,14</sup> However, despite efforts by Van Rysselberghe, Defay and a small school of physical electrochemists, most electrochemists remain wedded to a global thermodynamic description of the electrified interphase. Therefore, because the results of non-equilibrium thermodynamics applied to the electrified interphase cannot be considered an integral feature of the electrochemical gestalt, this section and those that follow will serve to develop a local formalism within the context of experimental observables that are important for this thesis.

Non-equilibrium thermodynamics is a field theory and all state variables are assumed continuous functions of space-time coordinates.<sup>15</sup> The local character of the theory arises because the basic equations are constructed in differential form and therefore only relate quantities from a single point on the space-time continuum. This can be a very convenient feature because the Maxwell theory of electromagnetism, classical mechanics, and fluid mechanics are also formulated as local field theories. The theory of non-equilibrium thermodynamics begins with construction of the Gibbs

entropy-balance equation in differential form.<sup>7, 10c, 13d, 15</sup> This equation describes the time evolution of the entropy for any given local volume element of a global system. The local entropy changes during a non-equilibrium process because there exists either an entropy flux,  $J_s$ , into or out of the volume element, an entropy production "source",  $\sigma$ , due to irreversible processes inside the volume element or both. This entropy source term is the local equivalent of the Clausius uncompensated heat and is always non-negative. Thus, the entropy source expression serves as a local formulation of the second law of thermodynamics and vanishes for reversible transformations. The goal of a non-equilibrium thermodynamic analysis of an irreversible system is to relate the entropy source term explicitly to processes that occur within local volume elements. The resulting entropy source expression is a sum of terms each being the product of a flux,  $J_i$ , that results from an irreversible process and a quantity,  $X_i$ , defined as a "thermodynamic force", that is related to some non-isotropic state variable, e.g.;

$$\sigma = \sum_i J_i \cdot X_i \geq 0 \quad (2)$$

Thus, the entropy source term serves as the basis for a systematic description of irreversible processes occurring within a system.

The entropy balance equation in its most general form is;

$$\rho \frac{ds}{dt} = -T^{-1} (\nabla \cdot (J_q - \sum_k \mu_k J_k) - T^{-1} J_q \cdot \nabla T - \sum_k J_k \cdot (\nabla(\mu_k T^{-1}) - F_k) - \Pi : \nabla v - \sum_j J_j A_j) \quad (3)$$

where  $s$  is the total entropy of a local volume element,  $\rho$  is the mass density,  $J_q$  is the heat flux,  $J_k$  the mass flux of species  $k$ ,  $F_k$  a

generalized force on species  $k$ ,  $\nu$  the center of mass (i.e., barycentric) velocity of the volume element,  $\Pi$  the viscous pressure tensor,  $J_j$  the rate of chemical reaction  $j$ ,  $A_j$  the chemical affinity of reaction  $j$ , and  $\mu_k$  the chemical potential of species  $k$ . Note that the symbol  $:$  denotes a scalar tensor product. Because the entropy balance equation has the general form,

$$\rho \frac{ds}{dt} = -\nabla J_s + \sigma$$

expressions for the entropy flux;

$$J_s = T^{-1} (J_q - \sum_k \mu_k J_k) \quad (4)$$

and the entropy source term;

$$\sigma = -T^{-2} J_q \cdot \nabla T - T^{-1} \sum_k J_k \cdot (T \nabla \mu_k T^{-1} - F_k) - T^{-1} \Pi : \nabla \nu - T^{-1} \sum_j J_j A_j \geq 0 \quad (5)$$

are obtained readily from equation (3). Examination of equation (4) reveals that the entropy flux has two contributions: one is the reduced heat flux  $J_q T^{-1}$  and the other arises from the mass flux,  $J_k$ . The entropy source term has four different contributions: the first term on the right-hand side of equation (5) arises from heat conduction, the second from mass flux, the third from gradients in the velocity field (e.g. viscous flow), and the fourth from chemical reactions. Equation (5) follows the general form exhibited by equation (2) wherein each term is the product of two factors: a flux and the gradient of an intensive state variable. These gradients of intensive state variables (i.e., thermodynamic forces) drive the system toward an equilibrium state and are sometimes referred to as "affinities."<sup>10, 15, 16</sup>

Equation (3) is somewhat inconvenient for analysis of electrified systems and can be modified to yield a more suitable form by introducing the relation;

$$\nabla(\mu_k T^{-1}) = \nabla\mu_k - \mu_k T^{-1} \nabla T$$

equation (3) becomes;

$$T\sigma = -J_s \cdot \nabla T - \sum_k J_k \cdot (\nabla\mu_k - F_k) - \Pi : \nabla v - \sum_j J_j A_j \quad (6)$$

Hence, the thermodynamic force conjugate to the mass flux,  $J_k$ , is related to a gradient of the chemical potential and a generalized force. It is important to note that  $\mu_k$  is *not* the equilibrium value of the chemical potential. For conservative forces that arise from a gradient in some time-invariant potential energy,  $\Psi_k$  (e.g.  $F_k = -\nabla\Psi_k$ ), one can introduce the quantity;

$$\tilde{\mu}_k = \mu_k + \Psi_k \quad (7)$$

and instead of equation (6);

$$T\sigma = -J_s \cdot \nabla T - \sum_k J_k \cdot \nabla\tilde{\mu}_k - \Pi : \nabla v - \sum_j J_j A_j \quad (8)$$

For an electrostatic system without polarization  $\Psi_k = z_k \phi$ , with  $z_k$  the charge per unit mass of component  $k$  and  $\phi$  the local electrostatic potential. Thus,  $\tilde{\mu}_k = \mu_k + z_k \phi$ , which is analogous to the conventional global definition of electrochemical potential.

Formulation of an entropy source term for any given system requires expressions for macroscopic conservation laws of mass, momentum and energy in local form.<sup>15</sup> These conservation laws, together with equations of state and the entropy balance equation form

a set that can be solved for any given initial and boundary conditions if the irreversible fluxes are known. However, because irreversible fluxes often cannot be measured directly, the set of non-equilibrium equations must be supplemented by ancillary phenomenological equations that relate the irreversible fluxes in a system to the thermodynamic forces. As a first approximation, the fluxes can be considered simple linear functions of their conjugate affinities (e.g., Fick's law of diffusion or Ohm's law of electrical conduction). However, because each flux could be a linear function of all the other thermodynamic forces as well, even a linear approximation must admit a host of cross-term effects (e.g., Soret, Peltier, electrokinetic, etc.) and in general;<sup>13a,b,15,17</sup>

$$J_i = \sum_j L_{ij} X_j$$

The phenomenological coefficients,  $L_{ij}$ , will be tensors for anisotropic media and scalar quantities for isotropic systems. Often the resulting matrix of phenomenological coefficients,  $L_{ij}$ , can be reduced by the Onsager reciprocity theorem (e.g.  $L_{ij} = L_{ji}$  or  $L_{ij} = \tilde{L}_{ji}$ )<sup>13a,b</sup> and certain spatial symmetry properties of the system that preclude coupling of processes with different "tensoral character." For example, in most isotropic cases, scalar and vectoral processes cannot be coupled to yield cross-effects. The appropriate set of reduced ancillary phenomenological equations will generate a complete and self-consistent set of partial differential equations for the non-equilibrium system of interest and allow calculation of the time evolution of all local thermodynamic state variables.

## Non-equilibrium Thermodynamics and Relaxation Phenomena.

The state of any local system at some arbitrary time will be defined by  $n$  external parameters,  $\zeta_i$ , and  $m$  even internal variables,  $\xi_i$ .<sup>18</sup> These latter variables are related to the internal structure of a local system and the distribution of energy over internal states. They could, for example, describe the progress of a chemical reaction or relaxation of molecular dipoles. The total differential of the local entropy in terms of  $\xi_i$  and  $\zeta_i$  may be written as;

$$Tds = \sum_n Z_i d\zeta_i - \sum_m A_i d\xi_i$$

or more generally in tensor notation;

$$Tds = \mathbf{Z} \cdot d\boldsymbol{\zeta} - \mathbf{A} \cdot d\boldsymbol{\xi}$$

Here  $\mathbf{A}$  is the affinity tensor that describes the thermodynamic forces acting within a local system and  $\mathbf{Z}$  is a  $n$ -dimensional vector with components  $Z_i = T\partial s/\partial\zeta_i$  that are thermodynamically conjugate to  $\zeta_i$ . At thermodynamic equilibrium  $\mathbf{A} \cdot d\boldsymbol{\xi} = 0$ , a condition that defines the equilibrium values of  $\xi_i$ . If the external parameters are constant while a system relaxes (e.g.  $\mathbf{Z} \cdot d\boldsymbol{\zeta} = 0$ ), then the rate of entropy production is;

$$\frac{ds}{dt} = -\frac{\mathbf{A} \cdot \partial \boldsymbol{\xi}}{T} \geq 0$$

If there exist linear relations between  $A_i$  and  $\xi_i$  then;

$$\frac{\partial \xi}{\partial t} = -L \cdot \frac{A}{T} \quad \text{where } L = \tilde{L} \quad (9)$$

Defining  $\Delta \xi = \xi - \xi^{eq}$ , where  $\xi^{eq}$  is a set of values for internal variables at thermodynamic equilibrium, the following relation is obtained;

$$A = \frac{\partial A}{\partial \xi} \cdot \xi - T \frac{\partial^2 s}{\partial \xi \partial \xi} \cdot \Delta \xi = Tg \cdot \Delta \xi \quad (10)$$

where  $-g = \partial^2 s / \partial \xi \partial \xi$  and is a symmetric and non-negative definite matrix. Substitution of equation (10) into (9) yields;

$$\frac{\partial \Delta \xi}{\partial t} = -L \cdot g \cdot \Delta \xi = -M \cdot \Delta \xi \quad (11)$$

Solutions for this set of simultaneous first order differential equations are superpositions of simple exponential decay terms for each variable e.g.;

$$\Delta \xi(t) = e^{-Mt} \cdot \Delta \xi(0) \quad (12)$$

Writing equations (11) and (12) in terms of their components gives expressions for each variable  $\xi_i$ ;

$$\frac{\partial \xi_i}{\partial t} = -\sum_k m_{ik} \Delta \xi_k$$

and

$$\Delta \xi_i(t) = \sum_{k1} c_{ik}^{-1} c_{k1} \Delta \xi_1(0) e^{-t/\tau_k}$$

where the set of relaxation times,  $\tau_k$ , are reciprocal eigenvalues of

the matrix  $M$  having elements  $m_{ik}$ .  $C$  is a matrix that diagonalizes  $M$  through a similarity transform.

If the state of a closed system can be specified by an infinite sequence of internal variables,  $\xi(y)$ , then  $\xi(y)$  represents an internal degree of freedom.<sup>18c, 19</sup> For example, the internal coordinate,  $y$ , may represent the orientation of a dipole in space or the progress of a chemical reaction.<sup>18c, 20</sup> This formalism can serve as a basis for a non-equilibrium thermodynamic analysis of equations of the motion for a local system within an internal coordinate space.<sup>21</sup> A description of relaxation dynamics in terms of internal degrees of freedom is useful for coupling non-equilibrium thermodynamics with non-equilibrium statistical mechanics, especially from a kinetic theory perspective.

#### An Operational Definition of Chemical Potential for Charged and Polarized Systems.

The condition for electrochemical equilibrium is simply that  $\nabla\tilde{\mu}_1^\beta = 0$ . As a definition of electrochemical potential, however, this thermodynamic statement has limited utility because it does not connect the value of  $\tilde{\mu}_1^\beta$  with physical properties of an electrified system. A global operational definition that characterizes the functional relationship between physical properties of a system and the electrochemical potential is desirable, but the conventional definition, equation (1), when applied to an electrified interphase does not satisfy  $\nabla\tilde{\mu}_1^\alpha = 0$  at equilibrium. A global operational definition of electrochemical potential for an electrified interphase that is useful and formally correct has not been discovered, *vide*

*supra*.

A local operational definition for  $\tilde{\mu}_1^\alpha$  arises naturally from equation (6) and should have a form similar to equation (7). The chemical potential is present in the affinity conjugate to the mass flux in the second term of equation (6) and at thermodynamic equilibrium;

$$A_i - \nabla\mu_1^\alpha - F_i = 0$$

hence;

$$\nabla\mu_1^\alpha = F_i \quad (13)$$

Equation (13) expresses the intuitable fact that at thermodynamic equilibrium the gradient of the chemical potential acts to oppose exactly any external forces acting on a system.<sup>22</sup> Thus, any local operational definition of the electrochemical potential will have the form  $\nabla\tilde{\mu}_1^\alpha = \nabla\mu_1^\alpha - F_i$ . If the coulomb force exerted on a point charge by an electric field is the only force acting on the system then;

$$\begin{aligned} \nabla\mu_1^\alpha &= \rho_i z_i E \\ &= -\rho_i z_i \nabla\phi_\alpha - \rho_i z_i c^{-1} \partial A / \partial t \end{aligned}$$

where  $A$  here is the vector potential. For electrostatic systems ( $\partial A / \partial t = 0$ )  $\nabla\mu_1^\alpha + \rho_i z_i \nabla\phi_\alpha = 0$  and equation (7) gives a local version of the conventional form for the electrochemical potential,  $\mu_1^\alpha = \mu_1^\alpha + \rho_i z_i \phi_\alpha$ . Thus, for an electrostatic system composed of point charges, the local definition of electrochemical potential corresponds to the conventional definition derived by Guggenheim.<sup>3a, b</sup> It must be emphasized that  $\mu_1^\alpha$  arises from short-range forces within a local

volume element that exists inside of an electrified interphase and is not related directly to the global value of  $\mu_1^\beta$  for some adjacent bulk phase.

Real electrochemical systems are composed of molecules of finite size that are inherently polarized or that are polarizable under the influence of an electric field. Thus, polarized molecules are present as well as ions and a description of the forces acting on the system must include both the coulomb force and ponderomotive forces that arise from the action of an electric field on polarized dielectric media. In the most general case the force acting on a charged and polarized system is;<sup>23</sup>

$$F = \rho z E + c^{-1} I \times B + (\nabla E) \cdot P + (\nabla B) \cdot M + \rho c^{-1} d/dt(P \times B) - \rho c^{-1} d/dt(M \times E) \quad (14)$$

Where  $I$  is the electric current vector,  $c$  the speed of light and  $B$  and  $M$  are the magnetic induction vector and magnetization vector respectively. All terms except the first and second are ponderomotive forces. Note that the symbol  $\times$  denotes a vector product. If magnetic terms are unimportant and  $I = 0$ , then equation (14) reduces to;

$$F = \rho z E + (\nabla E) \cdot P \quad (15)$$

Because  $(\nabla E) \cdot P = (P \cdot \nabla)E + P \times \nabla \times E$  and for electrostatic systems  $\nabla \times E = 0$ , equation (15) can be rewritten;

$$F = \rho z E + (P \cdot \nabla)E \quad (16)$$

The last term in equation (16) is the force that  $E$  would exert on a dipole of moment  $P$  and was proposed by Kelvin as the ponderomotive force on a dielectric.<sup>22a, 23</sup> If all off-diagonal terms of  $(P \cdot \nabla)E$

vanish then  $(\mathbf{P} \cdot \nabla) \mathbf{E} = -\mathbf{P} \cdot \nabla^2 \phi_\alpha$  and an expression for the local electrochemical potential for a charged and polarized system is obtained;

$$\tilde{\mu}_i^\alpha = \mu_i^\alpha + \rho_i z_i \phi_\alpha + \mathbf{P}_i \cdot \nabla \phi_\alpha \quad (17)$$

The term  $\mathbf{P}_i \cdot \nabla \phi_\alpha$  can be written as;

$$\mathbf{P}_i \cdot \nabla \phi_\alpha = -\frac{(\nabla \phi_\alpha)^2}{8\pi} \left( \frac{\partial \epsilon}{\partial \rho_i} \right)_{T, p, \rho_j, \mathbf{E}} \quad (18)$$

where  $\epsilon$  is the dielectric permittivity function of the local volume element and in general depends upon the electric field as well as  $T$ ,  $p$  and  $\rho_i$ . Substitution of equation (18) into equation (17) gives an expression for the electrochemical potential common to the literature of non-equilibrium thermodynamics;<sup>4 a-d, 10, 22 a</sup>

$$\tilde{\mu}_i^\alpha = \mu_i^\alpha + \rho_i z_i \phi_\alpha - \frac{(\nabla \phi_\alpha)^2}{8\pi} \left( \frac{\partial \epsilon}{\partial \rho_i} \right)_{T, p, \rho_j, \mathbf{E}} \quad (19)$$

Although equation (19) is a useful and self-consistent operational definition of electrochemical potential, it is desirable to develop a definition that relates the value of  $\mu_i^\alpha$  to a global value of the chemical potential of species  $i$  in the absence of an electric field. If the local free energy is some  $f(T, p, \rho_i, \mathbf{P})$ , then the electric field is;

$$\mathbf{E} = \left( \frac{\partial f}{\partial \mathbf{P}} \right)_{T, p, \rho_i}$$

and integration at constant  $T$ ,  $p$  and  $\rho_i$  gives;

$$f(T, p, \rho_i, \mathbf{P}) = f^0(T, p, \rho_i) + \int_0^{\mathbf{P}} \mathbf{E} d\mathbf{P}$$

This then yields an expression for  $\mu_i^\alpha$ ;

$$\mu_i^\alpha(T, P, \rho_i, \mathbf{E}) = \mu_i^\beta(T, P, \rho_i) - \frac{1}{8\pi} \int_0^{\mathbf{E}^2} \sum_i \left( \frac{\partial \epsilon}{\partial \rho_i} \right)_{T, P, \rho_j, \mathbf{E}} d\mathbf{E}^2 \quad (20)$$

Substitution of equation (20) into equation (19) gives the desired operational definition of electrochemical potential;<sup>2,2a</sup>

$$\tilde{\mu}_i^\alpha(T, P, \rho_i, \mathbf{E}) = \mu_i^\beta(T, P, \rho_i) + \rho_i z_i \phi_a - \frac{1}{8\pi} \int_0^{\mathbf{E}^2} \sum_i \left( \frac{\partial \epsilon}{\partial \rho_i} \right)_{T, P, \rho_j, \mathbf{E}} d\mathbf{E}^2 - \frac{\mathbf{E}^2}{8\pi} \left( \frac{\partial \epsilon}{\partial \rho_i} \right)_{T, P, \rho_j, \mathbf{E}} \quad (21)$$

where  $\mu_i^\beta$  refers to the chemical potential of species  $i$  within a bulk phase with chemical composition identical to that of the local volume element. The last two terms on the right hand side of equation (21) are not trivial for fluids that are employed for electrochemical studies and the expression will not reduce to that found for systems subject to pure coulomb forces.

### Surface Tension.

Surface tension is the only macroscopic observable that provides direct information about the state of an interphase at thermodynamic equilibrium. It is desirable to develop a general definition of surface tension within the phenomenological context of non-equilibrium thermodynamics for analysis of dynamic surface tension and to provide some insight into physical parameters that could be important for the observed response. Measurement and interpretation of dynamic surface tension at the electrified interphase is the major topic of chapter 4.

Using the local definition of electrochemical potential provided by equation (21) a local analog of the Gibbs-Duhem equation for

electrified interphases at thermodynamic equilibrium can be obtained;<sup>4, 11, 24</sup>

$$d\gamma^\alpha = \Lambda^{-1} [s^\alpha dT^\alpha + V^\alpha dp^\alpha - \sum_i n_i^\alpha d\tilde{\mu}_i^\alpha] \quad (22)$$

where  $\Lambda$  is the surface area of the interphase. Outside of equilibrium and under a regime of constant external forces an affinity tensor may also exist and equation (22) becomes,<sup>24</sup>

$$d\gamma^\alpha = \Lambda^{-1} [s^\alpha dT^\alpha + V^\alpha dp^\alpha - \sum_i n_i^\alpha d\tilde{\mu}_i^\alpha - \mathbf{A}^\alpha \cdot d\xi^\alpha] \quad (23)$$

or,

$$d\gamma^\alpha = \Lambda^{-1} [s^\alpha dT^\alpha + V^\alpha dp^\alpha - \sum_i n_i^\alpha d\tilde{\mu}_i^\alpha - \sum_i A_i^\alpha d\xi_i^\alpha] \quad (24)$$

$\xi_i^\alpha$  is referred to as the "degree of advancement" of some internal degree of freedom.<sup>4, 7, 10, 16, 24</sup> For example,  $\xi_i$  could represent the ensemble average of the first moment (e.g. direction cosine) of the dipole orientation of species  $i$  within a local volume element.<sup>24</sup> If external forces are not constant then equation (23) becomes,

$$d\gamma^\alpha = \Lambda^{-1} [s^\alpha dT^\alpha + V^\alpha dp^\alpha - \sum_i n_i^\alpha d\tilde{\mu}_i^\alpha - \mathbf{A}^\alpha \cdot d\xi^\alpha - \mathbf{Z} \cdot d\zeta] \quad (25)$$

An important class of non-equilibrium systems continue to relax after diffusion equilibrium has been established. If this is the case within an electrified interphase then equation (25) can be written as,<sup>24 a, b</sup>

$$d\gamma^\alpha = -\Lambda^{-1} [\mathbf{A}^\alpha \cdot d\xi^\alpha + \mathbf{Z} \cdot d\zeta]$$

or for constant external forces,

$$d\gamma^\alpha = -\Lambda^{-1} \mathbf{A}^\alpha \cdot d\xi^\alpha \quad (26)$$

The time derivative of equation (26) is of interest here because the primary experimental observable discussed in chapter 4 is the time-resolved dynamic surface tension. If there exists linear relations between  $A_1^\alpha$  and  $\xi_1^\alpha$  then from equations (9) and (26),

$$\frac{d\gamma^\alpha}{dt} = -\Lambda^{-1}A^\alpha \cdot \frac{\partial \xi^\alpha}{\partial t} = \Lambda^{-1}T^{-1}L^\alpha \cdot (A^\alpha)^2 \quad (27)$$

$$= \Lambda^{-1}T(L^\alpha)^{-1} \cdot \left(\frac{\partial \xi^\alpha}{\partial t}\right)^2 \quad (28)$$

where  $L$  is the matrix of phenomenological coefficients described by Onsager and  $T$  the thermodynamic temperature. It can also be shown that for any series of non-equilibrium electrocapillary curves the time derivative of the ECM is related directly to the affinity tensor,<sup>24 a, b</sup>

$$\frac{\partial \gamma_{max}^\alpha}{\partial t} = \frac{\partial \gamma_{mmax}^\alpha}{\partial \xi^\alpha} = -\Lambda A^\alpha \quad (29)$$

$$= \Lambda^{-1}T(L^\alpha)^{-1} \cdot \frac{\partial \xi^\alpha}{\partial t} \quad (30)$$

Thus, measurement of the dynamic surface tension of non-equilibrium electrified interphases driven to statistical equilibrium by constant external forces offers the prospect of evaluation of  $A$  and  $L$ . It is important to note that equations (22)-(30) refer to a local surface tension, whereas the experimental observable is the integration of the local surface tension over the total volume of the electrified interphase.

#### Limitations of Non-equilibrium Thermodynamics.

The range of validity for the first-order conventional

formulation of non-equilibrium thermodynamics is equivalent to the range of validity for the Gibbs relation, *i.e.*;<sup>7,25</sup>

$$T^\alpha ds^\alpha = du^\alpha + p^\alpha dV^\alpha - \sum_i \tilde{\mu}_i^\alpha dn_i^\alpha$$

The nature of the non-equilibrium distribution function,  $f$ , for the system of interest determines the validity of a non-equilibrium analysis based upon a Gibbs expression for the entropy balance. Non-equilibrium distribution functions often can be evaluated by the method of Enskog,<sup>25,26</sup> who developed an approximate solution to the Boltzmann equation in terms of a series of space-time derivatives,

$$f = f_0 + f_1 + f_2 + \dots + f_n \quad (31)$$

Prigogine<sup>25b</sup> demonstrated that first-order non-equilibrium thermodynamics is valid for systems where the series in equation (31) converges rapidly and  $f = f_0 + f_1$  is a good approximation to the distribution function. If  $f_2$  or higher order terms are important, then the entropy production of the non-equilibrium system depends explicitly on the gradients or higher order derivatives of state variables.<sup>25</sup>

The Enskog expansion is of particular relevance to strongly inhomogeneous and anisotropic systems such as the electrified interphase. The need to modify expressions for the free energy of interphases with terms that depend on the density gradients of chemical species within the interphase has been advocated in various forms since van der Waals introduced the idea in 1893.<sup>27</sup> Density gradient terms are a general feature of most contemporary analysis of interphases,<sup>27e</sup> but will only be important in the dynamical case if

their time derivatives are not zero. The analysis of experimental results in chapter 4 will assume that the time derivatives of gradient terms within local volume elements immediately adjacent to the electrode that contributes most to the integrated surface tension are zero.

## BIBLIOGRAPHY

1. Gibbs, J.W. *Collected Works*, volume 1; Longmans, Green:N.Y., 1928, p.336.
2. Grahame, D.C.; Whitney, R.B. *J. Am. Chem. Soc.* 1942, 64, 1548.
3. a. Guggenheim, E.A. *J. Chem. Phys.* 1929, 33, 842.  
b. Guggenheim, E.A. *Thermodynamics*, fifth edition; North Holland:Amsterdam, 1967, §8.03.  
c. Gibbs, J.W. *op. cit.*, p.429.
4. a. Prigogine, I. *J. Chim. Phys.* 1952, 49, 79.  
b. Prigogine, I.; Mazur, P.; Defay, R. *J. Chim. Phys.* 1953, 50, 146.  
c. Prigogine, I.; Mazur, P. *Mém. Acad. Roy. Belg.* 1952, 23, 1.  
d. Defay, R.; Mazur, P. *Bull. Soc. Chim. Belges* 1954, 63, 562.  
e. Defay, R.; Prigogine, I.; Bellemans, A. *Surface Tension and Adsorption*; Longmans, Green:N.Y., 1966, p.391.
5. a. Mohilner, D.M. in *Electroanalytical Chemistry*, volume 1; A.J. Bard, ed.; Marcel Dekker:N.Y., 1966.  
b. Parsons, R. in *Modern Aspects of Electrochemistry*, volume 1; J.O'M. Bockris, ed.; Butterworth:London, 1954.  
c. Delahay, P. *Double Layer and Electrode Kinetics*; Wiley-Interscience:N.Y., 1965, chap. 2.  
d. Conway, B.E. *Theory and Principles of Electrode Processes*; Ronald:N.Y., 1965, chaps. 4 and 5.  
e. Grahame, D.C. *Chem. Rev.* 1947, 41, 441.  
f. Grahame, D.C. *Ann. Rev. Phys. Chem.* 1955, 6, 337.  
g. Bard, A.J.; Faulkner, L.R. *Electrochemical Methods*; J. Wiley and Sons:N.Y., 1980, chap. 12.
6. a. Defay, R.; Prigogine, I.; Bellemans, A. *op. cit.*, p.56.  
b. Defay, R. *Etude Thermodynamique de la Tension Superficielle*; Villars:Paris, 1934.  
c. Defay, R.; Pétré, G. in *Surface and Colloid Science*, volume 3; E. Matijević, ed.; Wiley-Interscience:N.Y., 1971, p.27.  
d. Defay, R.; Prigogine, I.; Sanfeld, A. *J. Coll. Interfac. Sci.* 1977, 58, 498.
7. Sanfeld, A. *Introduction to the Thermodynamics of Charged and Polarized Layers*; John Wiley and Sons:N.Y., 1968, chap. 2.
8. a. Sanfeld, A. *op. cit.*, chaps. 7, 8 and 12.  
b. deGroot, S.R.; Mazur, P. *Non-Equilibrium Thermodynamics*; Dover:N.Y., 1984, chap. 13.  
c. Landau, L.D.; Lifshitz, E.M.; Pitaevskii, L.P. *Electrodynamics of Continuous Media*; Pergammon:Oxford, 1984.
9. a. Defay, R. *J. Chim. Phys.* 1952, 49, C80.  
b. Piontelli, R. *ibid.* 1952, 49c, 80.

10. a. Van Rysselberghe, P. in *Modern Aspects of Electrochemistry*, volume 4; J.O'M. Bockris, ed.; Plenum:N.Y., 1966, p.1.  
b. Van Rysselberghe, P. *Electrochemical Affinity - Studies in Electrochemical Thermodynamics and Kinetics*; Hermann:Paris, 1955.  
c. Van Rysselberghe, P. *Thermodynamics of Irreversible Processes*; Hermann:Paris, chaps. 4 and 6.  
d. Van Rysselberghe, P. *J. Chem. Phys.* 1949, 17, 1229.  
e. Van Rysselberghe, P. *ibid.* 1958, 29, 640.
11. Defay, R. *J. Chim. Phys.* 1949, 46, 375.
12. a. Thomson, W. *Proc. Roy. Soc. Edinburgh.* 1854, 3, 225.  
b. *Ibid. Math. Phys. Papers* 1882, 1, 232.
13. a. Onsager, L. *Phys. Rev.* 1931, 37, 405.  
b. *Ibid.* 1932, 38, 2265.  
c. Meixner, J. *Z. Phys. Chem. B* 1943, 53, 235.  
d. Prigogine, I. *Etude Thermodynamique des Phénomènes Irréversibles*; Dunod:Paris, 1947.  
e. deGroot, S.R.; Mazur, P. *op. cit.*, chap. 1.
14. a. Van Rysselberghe, P. *Electrochim. Acta* 1963, 8, 583.  
b. *Ibid.* 1963, 8, 709.  
c. *Ibid.* 1964, 9, 1547.
15. deGroot, S.R.; Mazur, P. *op. cit.*, chaps. 2, 3 and 4.
16. DeDonder, Th. *L'affinité*; Gauthier-Villars:Paris, 1927.
17. a. deGroot, S.R.; Mazur, P. *op. cit.*, chaps. 6 and 7.  
b. Casimir, H.B.G. *Rev. Mod. Phys.* 1945, 17, 343.
18. a. Meixner, J. *Kolloid Zeitschr.* 1953, 134, 3.  
b. *Ibid. Zeitschr. Phys.* 1954, 139, 30.  
c. deGroot, S.R.; Mazur, P. *op. cit.*, chap. 10.
19. Prigogine, I.; Mazur, P. *Physica* 1953, 19, 241.
20. Kramers, H.A. *Physica* 1940, 7, 284.
21. Meixner, J. *Zeitschr. Phys.* 1957, 149, 624.
22. a. Sanfeld, A. *op. cit.*, chaps. 4 and 5.  
b. deGroot, S.R.; Mazur, P. *op. cit.*, chaps. 2 and 13.
23. deGroot, S.R.; Mazur, P. *op. cit.*, chap. 14.
24. a. Sanfeld, A. *op. cit.*, chap. 14.  
b. Sanfeld, A.; Steinchen, A.; Defay, R. *J. Phys. Chem.* 1969, 73, 4047.  
c. Prigogine, I.; Mazur, P. *Physica* 1951, 17, 661.

25. a. Yourgrau, W.; van der Merwe, A.; Raw, G. *Treatise on Irreversible and Statistical Thermophysics.*; Dover:N.Y., 1982, §I-I.  
b. Prigogine, I. *Physica* 1949, 15, 272.
26. a. Enskog, D. *Kungl. Svenska Acad.* 1922, 63, 4.  
b. Chapman, S.; Cowling, T.G. *The Mathematical Theory of Non-Uniform Gases.*; Cambridge:Cambridge, 1952.  
c. S.R. deGroot, P. Mazur *op. cit.*, chap. 9.
27. a. van der Waals, J.D. *Zeit. Phys. Chem.* 1894, 13, 657.  
b. *Ibid.* *J. Stat. Phys.* 1979, 20, 197.  
c. Landau, L.D.; Lifshitz, E.M.; Pitaevskii, L.P. *op. cit.*, § 39.  
d. Cahn, J.W.; Hillard, J.E. *J. Chem. Phys.* 1958, 28, 258.  
e. Rowlinson, J.S.; Widom, B. *Molecular Theory of Capillarity*; Clarendon:Oxford, 1982, chap.3.

**CHAPTER 4**

## INTRODUCTION

Conventional techniques for investigation of the dynamical behavior of electrified interphases (e.g., chronocoulometry, coulostatitics, small-signal ac impedance) employ charge density and electrostatic potential as observables.<sup>1a-e</sup> A common assumption in the analysis of electrochemical experiments that employ these variables is that the electrostatic potential is related directly to the free energy of the electrified interphase.<sup>1,7b,c</sup> The limits under which this assumption can be considered operative are equivalent to a claim that mass-transport processes that are observable as a current impose the upper limit to the relaxation rate of an electrified interphase. All other possible relaxation processes are assumed to proceed at rates much greater than mass-transport. In other words, establishment of a diffusion-migration equilibrium (e.g.  $\nabla\bar{\mu}_1 = 0$ ) is regarded as sufficient evidence for statistical equilibrium. This assumption finds primary application in the study of electrochemical processes that are confined within the interphase or that occur at rates limited by interfacial electron transfer.<sup>1</sup> It is of little consequence for the very large body of electrochemical reaction-diffusion problems where interfacial processes are not rate limiting.

In an homogeneous solution, typical solvent reorganization time-scales are on the order of  $10^{-9}$ s and thus, by application of Occam's razor, the assumption that mass-transport processes are rate limiting for interfacial relaxation seems both reasonable and convenient. According to the law of Murphy, however, it is desirable

to have unambiguous experimental evidence for the validity of assumptions before proceeding with undue enthusiasm. The conventional electrochemical observables of electric potential and charge density cannot be used to provide a direct experimental test because they are not related directly to the state of the interphase (Chapter 3). Surface tension, on the other hand, is related directly to both the equilibrium and non-equilibrium state of the interphase<sup>1,7,8</sup> and, if measured concomitant with the electric potential and current, would provide direct evidence for the validity of the assumption of mass-transfer limited relaxation.

All conventional methods for measuring surface tension at electrified interphases (Table I) are confined to systems that are in thermodynamic equilibrium and are not useful for dynamical studies.<sup>1,6</sup> Thus, investigation of the dynamical behavior of the surface tension required the development of a new method for measuring both equilibrium and dynamic surface tensions. This chapter describes this method, which is an extension to the electrified interphase of the conventional Wilhelmy plate technique, and experimental results that cast serious doubt onto the validity of the assumption of mass-transfer limited relaxation rates for electrified interphases.

TABLE I

TECHNIQUES FOR DIRECT MEASUREMENT OF SURFACE TENSION AT THE  
ELECTRIFIED Hg-AQUEOUS ELECTROLYTE INTERPHASE.

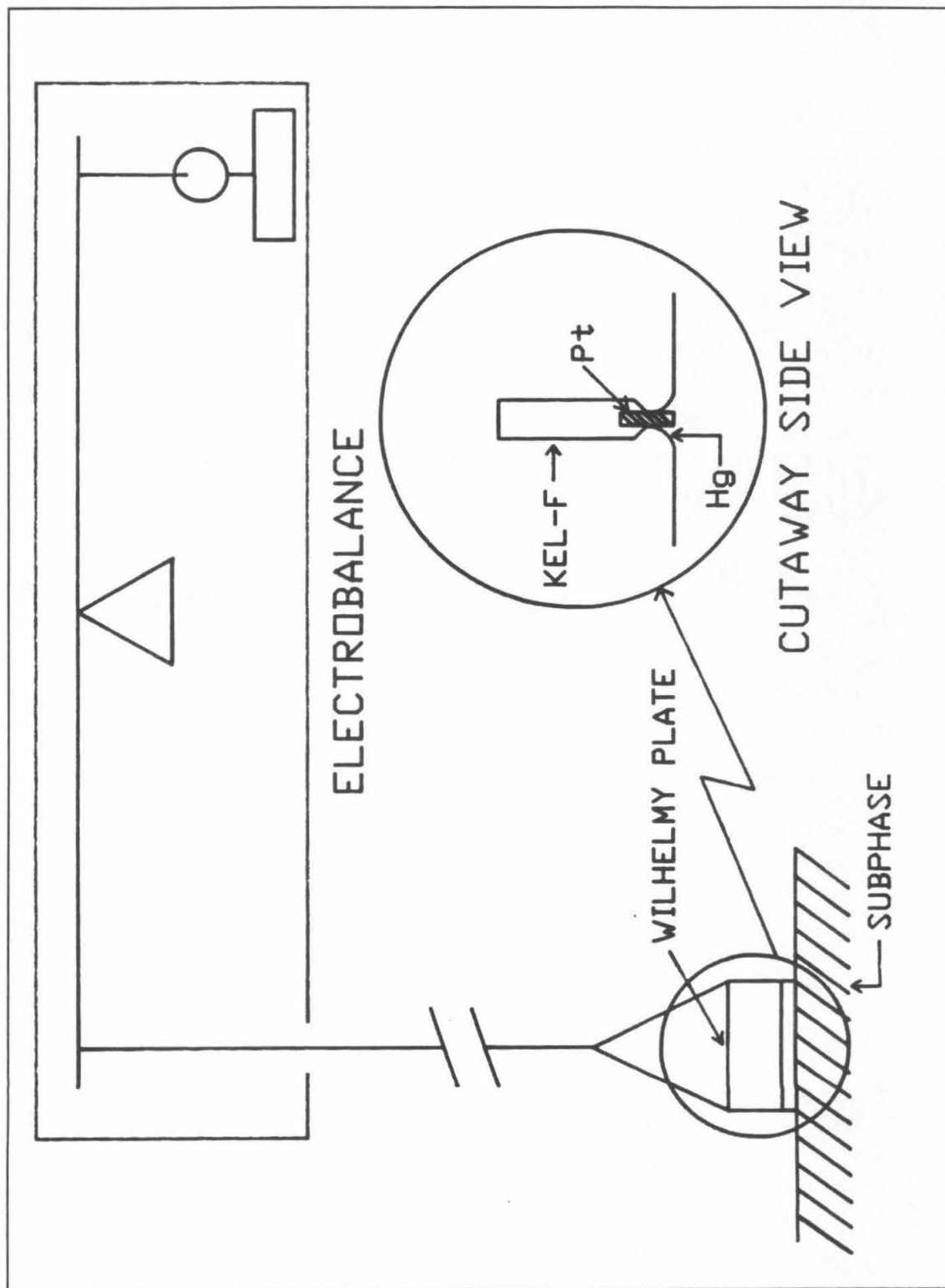
	<u><math>\tau</math>/DATA POINT</u> <u>(sec)</u>	<u>PRECISION</u> <u>(dyne/cm)</u>	<u>DYNAMIC <math>\gamma</math></u> <u>CAPABILITY</u>
SESSILE DROP	~3600	$\pm 0.2$	NO
CAPILLARY ELECTROMETER	~3600	$\pm 0.15$	NO
MAXIMUM BUBBLE PRESSURE	$\geq 5$	$\pm 0.03$	NO
WILHELMY PLATE	$\geq 0.05$	$\pm 0.005$	YES

**EXPERIMENTAL.****Wilhelmy Plate.**

A 0.13 mm thick platinum plate was cut into a 0.7 cm by 2.5 cm rectangle and press fit into a 0.08 mm groove that had been machined into a tapered Kel-F support as illustrated in the inset of Figure 1. The press fit ensures a very tight seal between the Kel-F and the platinum that excludes any leakage of supporting electrolyte. Approximately 4 mm of exposed platinum extends below the Kel-F support on the assembled Wilhelmy plate. This exposed portion was plated with mercury by dipping the plate into a fresh sodium-mercury amalgam (~ 1:10 Na:Hg) until visual inspection indicated that the platinum had been plated completely (ca. 60 sec.). The Hg-plated assembly was then cleaned by sonication (Branson 3200) for 30 minutes in methanol and then for 30 minutes in 1,1,1 trichloroethane. When not in use, the assembly was stored by suspending it above a small mercury pool and adjusting the level of the mercury pool such that the top of the Hg meniscus abutted the edge of the Kel-F support.

The Wilhelmy plate was connected to a Cahn 2000 recording electrobalance for surface tension measurements by a stiff 0.10 mm diameter nichrome wire that was ca. 80 cm in length. The electrobalance was supported and encased by a glass vessel and the wire attached to the Wilhelmy plate ran down to the electrochemical cell via a feedthrough (Figures 1 and 2). The glass electrobalance support vessel was suspended from a rigid frame by a brass threaded-rod and nut assembly that allowed the vertical position of the electrobalance to be changed by rotation of the nut. The bottom

Figure 1. Schematic illustration of the Wilhelmy plate surface tension measuring instrument. The cutaway side view displays the platinum Wilhelmy plate inset into a Kel-F support to isolate it from the supporting electrolyte.



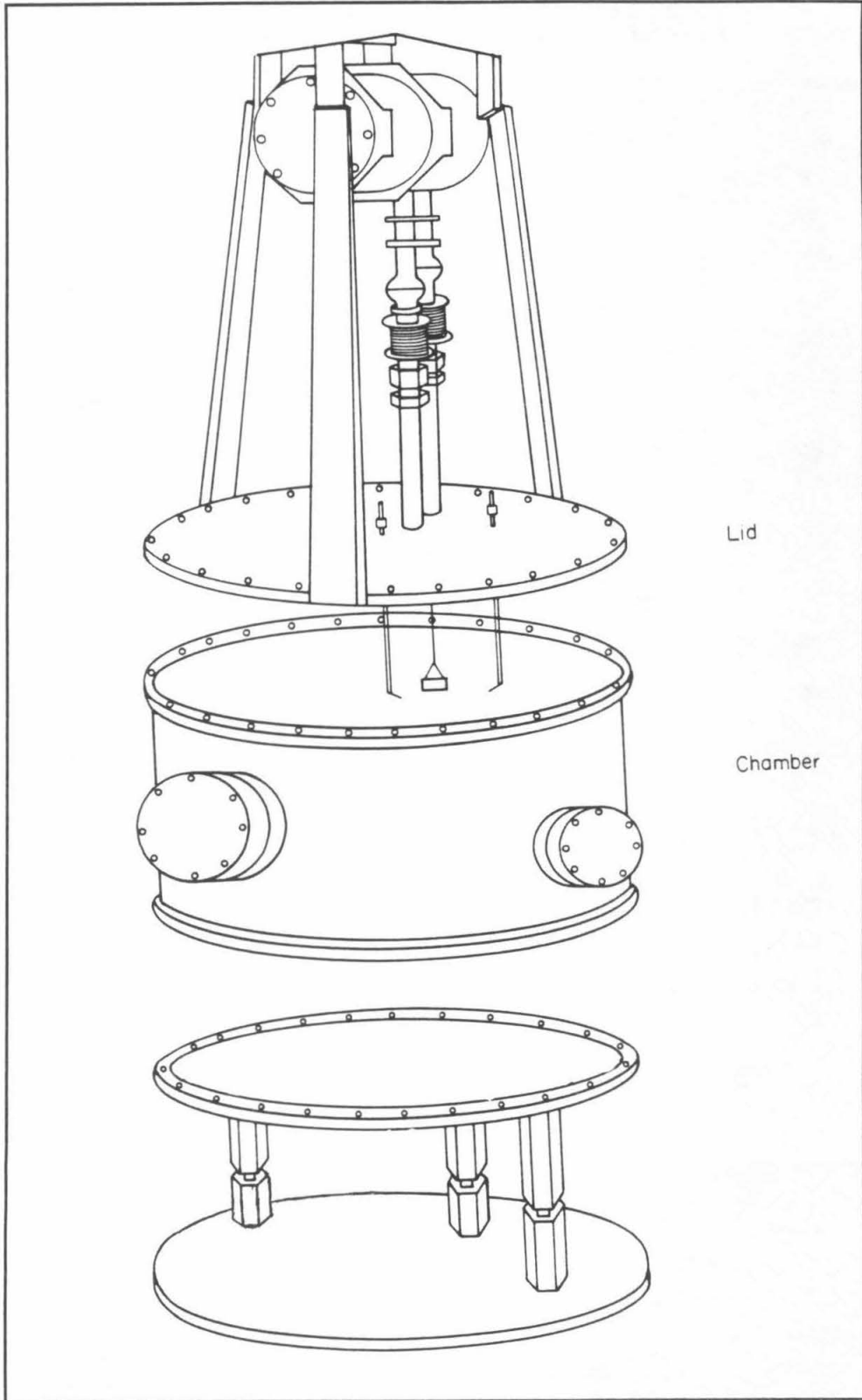
edge of the Wilhelmy plate was positioned such that it just touched the surface of the Hg-pool electrode by adjusting the vertical position of the electrobalance.

#### Electrochemical Cell.

The electrode used here was a  $73.44 \text{ cm}^2$  circular mercury pool that was formed by pouring Hg into the bottom of a crystallization dish with an internal diameter of 9.67 cm. Electrical contact was provided by a PTFE sheathed platinum wire that clipped over the edge of the crystallization dish. The counter-electrode was a large piece of platinum wire that was formed into a nearly circular loop slightly larger in diameter than the inside of the crystallization dish. This allowed the counter-electrode to act as a spring when placed into the crystallization dish and to hold itself tightly in place around the perimeter of the cell. The cell was placed into a large (~ 55 cm diameter) stainless steel chamber (Figure 2) that provided both an inert environment and vibration isolation. A saturated calomel (SSCE) reference electrode was located outside of the chamber and was connected to the cell via a long glass probe. The tip of the probe that was in contact with the cell was sealed by a piece of vycor glass that provided a conductive and nearly ion-impermeable junction. Different probes were used with different supporting electrolyte solutions and the vycor glass allowed to equilibrate with the supporting electrolyte solution for several days before use. When not in use the vycor glass was always immersed in a solution of the appropriate supporting electrolyte.

Prior to an experiment, the chamber was flushed with a vigorous

Figure 2. An exploded view of the stainless steel inert atmosphere chamber. The electrobalance and vacuum aspiration ports are attached to the lid. Electrical feedthroughs and viewing ports are attached to ports on the chamber. The lower portion of the chamber is used as a mass-damper for more effective vibration isolation. The entire assembled chamber is suspended by elastomer fiber cords that are attached to the lid.



flow of deoxygenated argon for several hours. The crystallization dish was then placed into the chamber, connected to electrical leads, and Hg was added to form the pool electrode. The Hg surface was cleaned by aspiration and the Wilhelmy plate lowered onto the surface and positioned near the center of the cell. Supporting electrolyte that had been deaerated with deoxygenated argon was added until both the counter-electrode and the Wilhelmy plate were completely immersed (ca. 100 ml). The reference electrode probe was then introduced and positioned near the Wilhelmy plate.

Linear sweep voltammetry and potential step experiments were performed according to published procedures using a Princeton Applied Research 173-175 potentiostat-programmer combination controlled remotely by an IBM AT microcomputer. Analog-to-digital and digital-to-analog conversion tasks were handled by two 12-bit Analog Devices converters (models RTI-802 and RTI-815). Software macro routines for driving this hardware were written by Analog Devices and used with software written in-house for each specific electrochemical technique. Voltage, current and surface tension data were acquired simultaneously on three channels at approximately 20 Hz and control was provided by interrupt driven pulses. Experiments were conducted at ambient temperature ( $22 \pm 2^\circ\text{C}$ ). Potentials were all measured and reported with respect to a SSCE reference electrode.

#### Vibration Isolation.

The apparatus illustrated in Figure 2 was isolated from mechanical vibration by suspending the entire instrument from three elastomer fiber cords ~1 cm in diameter, which were attached to a

wooden tripod assembly. The chamber is leveled by adjusting turnbuckles that connect the cords to the tripod. Prior to an experiment, the apparatus is supported from below by lab jacks that are lowered slowly to allow the chamber to hang freely during the experiment. No special precautions were taken to isolate the instrument from acoustic vibrations.

#### **Materials.**

Supporting electrolyte solutions were prepared from recrystallized analytical grade NaF. Laboratory distilled water was purified by passage through a purification train (Barnstead-Nanopure). Triple-distilled instrument grade mercury (Bethlehem Apparatus Co.) was used for pool electrodes.

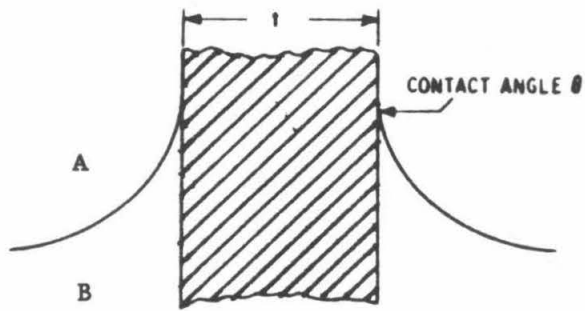
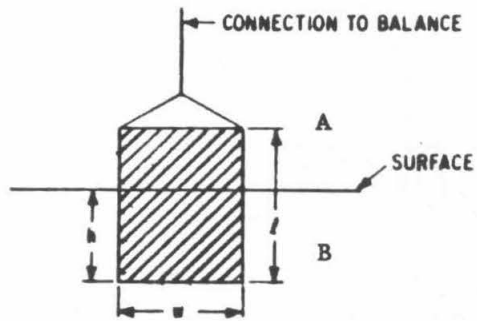
### A Modified Wilhelmy Plate for Static and Dynamic Surface Tension Measurements at the Electrified Interphase.

In 1863 Wilhelmy<sup>2</sup> introduced a technique for measuring surface tension that is based on determining the force exerted by the meniscus of some liquid adhering to the side of a thin plate that is positioned normal to and just touching the surface of the liquid. This technique is used most frequently for measuring the surface tension at liquid-gas interphases, but can be adopted for studies of liquid-liquid interphases as well.<sup>3</sup> The basic elements of the physics of the technique are illustrated in Figure 3. Fluid B is of greater density and intrinsic surface tension than fluid A and wets the surface of the Wilhelmy plate forming a meniscus with a contact angle  $\theta$ , that depends on the degree of wetting. The plate is suspended above the surface and the position of the bottom edge of the plate is adjusted such that it is at or slightly below the level of the surface. The plate is constructed from an appropriate material with density  $\rho_p$ , has a total volume of  $V_p = lwt$  and a perimeter around which the meniscus forms of length  $L_p = 2(t + w)$ . The net force on the plate is;

$$F_p = \rho_p V_p g + \gamma_{AB} L_p \cos\theta - \rho_B (hwt)g \quad (1)$$

where  $g$  is the acceleration of gravity,  $\rho_B$  the density of fluid B, and  $\gamma_{AB}$  the surface tension of the interphase between the two fluids. The last term on the right-hand side of equation (1) is the buoyancy of the plate due to displacement of a volume  $V_B = hwt$  of fluid B. If the wetting of the plate by fluid B is complete, then  $\theta = 0$  and equation

Figure 3. Illustration of the basic physical elements that determine the force on a Wilhelmy plate (see text).



(1) reduces to;

$$F_p = (\rho_p V_p - \rho_B V_B)g + \gamma_{AB} L_p$$

Thus,  $\gamma_{AB}$  is related directly to the force on a Wilhelmy plate, a quantity that can be measured simply by weighing the plate.

The Wilhelmy plate method is not regarded favorably as a technique for measuring absolute surface tension because of uncertainty in evaluating the buoyancy term and the frequently encountered experimental difficulty of completely or reproducibly wetting the plate with the subphase fluid. However, it is a fast and accurate method for measuring dynamic and differential surface tensions. If  $\theta$  and  $h$  in Figure 3 are constant, then equation (1) can be written in differential form as;

$$dF_p = L_p \cos\theta d\gamma_{AB}$$

and if  $\theta = 0$ ;

$$dF_p = L_p d\gamma_{AB} \quad (2)$$

Thus,  $\gamma_{AB}$  scales directly with  $F_p$  and the proportionality constant  $L_p$  can be determined by measurement of the perimeter length of the plate or evaluated independently if absolute values of  $\gamma_{AB}$  are known. It is important to note that, in general, contributions to  $L_p$  from surface roughness on microscopic length scales cannot be neglected because the length scale of the interphase is of comparable magnitude. Thus, the perimeter length should be evaluated empirically by comparing  $\gamma_{AB}$  obtained by the Wilhelmy plate method, with values acquired by another technique such as maximum bubble pressure (Table I), which gives high

accuracy absolute values of the surface tension.

The central element of the technique used here is an adaptation of a conventional platinum Wilhelmy plate for use with a mercury subphase and in an electrochemical cell. The inset in Figure 1 displays a cutaway side view of the modified Wilhelmy plate. The exposed platinum surface is plated with mercury by treating it with sodium-mercury amalgam as described by Smith.<sup>4</sup> This procedure results in complete wetting of the platinum plate by a mercury subphase. The remainder of the platinum plate is encased in a machined jacket of Kel-F fluoropolymer that isolates it from supporting electrolyte and eliminates any possible potential dependent platinum-electrolyte interphase contributions to the observed surface tension. For the mercury-water interphase, the maximum height of the meniscus at room temperature is ca. 4 mm (e.g.  $\gamma = 426 \text{ dyne cm}^{-1}$ ) and at least this much of the platinum plate should be exposed and plated. The force on the Wilhelmy plate was measured by a recording electrobalance (Cahn 2000) that maintains the plate in a constant vertical position and abrogates the need to make buoyancy corrections. The experimental apparatus is illustrated schematically in Figure 1. The electrochemical cell was placed inside a large stainless steel chamber that maintains a clean atmosphere of dry and deoxygenated argon, and the mercury pool electrode was then prepared by skimming off contaminated surface layers using vacuum aspiration. The Wilhelmy plate was lowered onto the large ( $73.44 \text{ cm}^2$ ) mercury pool electrode until the bottom edge of the plate was at or slightly below the surface level of the pool. Deaerated supporting electrolyte was added to the electrochemical cell up to a level that completely immersed the

Wilhelmy plate. A long glass probe that was sealed at one end by a piece of Vycor glass, which provided a conductive and ion-impermeable junction provided contact between the electrochemical cell and a SSCE reference electrode that was located outside of the inert atmosphere chamber. The apparatus was isolated from vibration by suspending it from elastomer fiber cords attached to a wooden frame.

#### Sensitivity of the Wilhelmy Plate Technique for Static Surface Tension Measurements.

A useful first step for evaluating a new technique is to establish its sensitivity limits. Because measurement of surface tension by the Wilhelmy technique is accomplished by weighing the plate, the primary limit on the sensitivity will be either the lowest mass unit that the electrobalance can resolve ( $\sim 5 \times 10^{-8}$  g) or noise in the electrobalance signal due to mechanical vibration of the plate. For an instrument located on the third floor of a large concrete structure (*i.e.* Noyes Laboratory of Chemical Physics) and directly adjacent to a utility core, mechanical vibration is most likely to limit the sensitivity of the technique. This hypothesis was supported by monitoring the electrobalance output at 100 Hz for a five minute period as it measured the mass of the Wilhelmy plate suspended both in air and in a 0.1 M NaF supporting electrolyte solution. The sensitivity of the measurement was  $\pm 5 \times 10^{-6}$  g, a number about two orders of magnitude larger than the lower limit for the electrobalance claimed by the manufacturer.

Because the surface tension of mercury is large, it tends to support vibration-driven standing waves more efficiently than other

fluids such as water. The electrobalance signal for the Wilhelmy plate positioned at an electrified mercury-aqueous electrolyte interphase has a lower sensitivity than that measured for a plate hanging freely in air or water because of this effect. The sensitivity of the instrument for a plate positioned at the electrified mercury-water interphase was  $\pm 1 \times 10^{-5}$  g. The sensitivity of the instrument for mass measurements is related to the sensitivity for surface tension measurements by replacing  $dF_p$  in equation (2) by  $gdm$  to give;

$$\begin{aligned} d\gamma_{AB} &= 2(t + w)^{-1}gdm \\ &= Kdm \end{aligned} \quad (3)$$

where  $m$  is the mass of meniscus. The value of  $K$  for the Wilhelmy plate used here, *vide infra*, was  $497.8 \text{ s}^{-2}$  and the surface tension sensitivity was  $\pm 5 \times 10^{-3} \text{ dyne cm}^{-1}$ . This value for the surface tension sensitivity is slightly better than the best values reported for the Wilhelmy technique applied to aqueous subphases in Langmuir troughs.<sup>3, 6</sup>

A surface tension sensitivity of  $\pm 5 \times 10^{-3} \text{ dyne cm}^{-1}$  is about two orders of magnitude better than the minimum necessary for the experiments described here and is the direct result of an efficient vibration isolation scheme. Although wood and elastomer fiber cords can be expected to damp mechanical vibrations efficiently at high and mid-range frequencies, the effective vibration isolation observed at low frequencies cannot be ascribed directly to the dissipation characteristics of the materials. Rather, it is likely that the tripod suspension system is responsible for the good low frequency

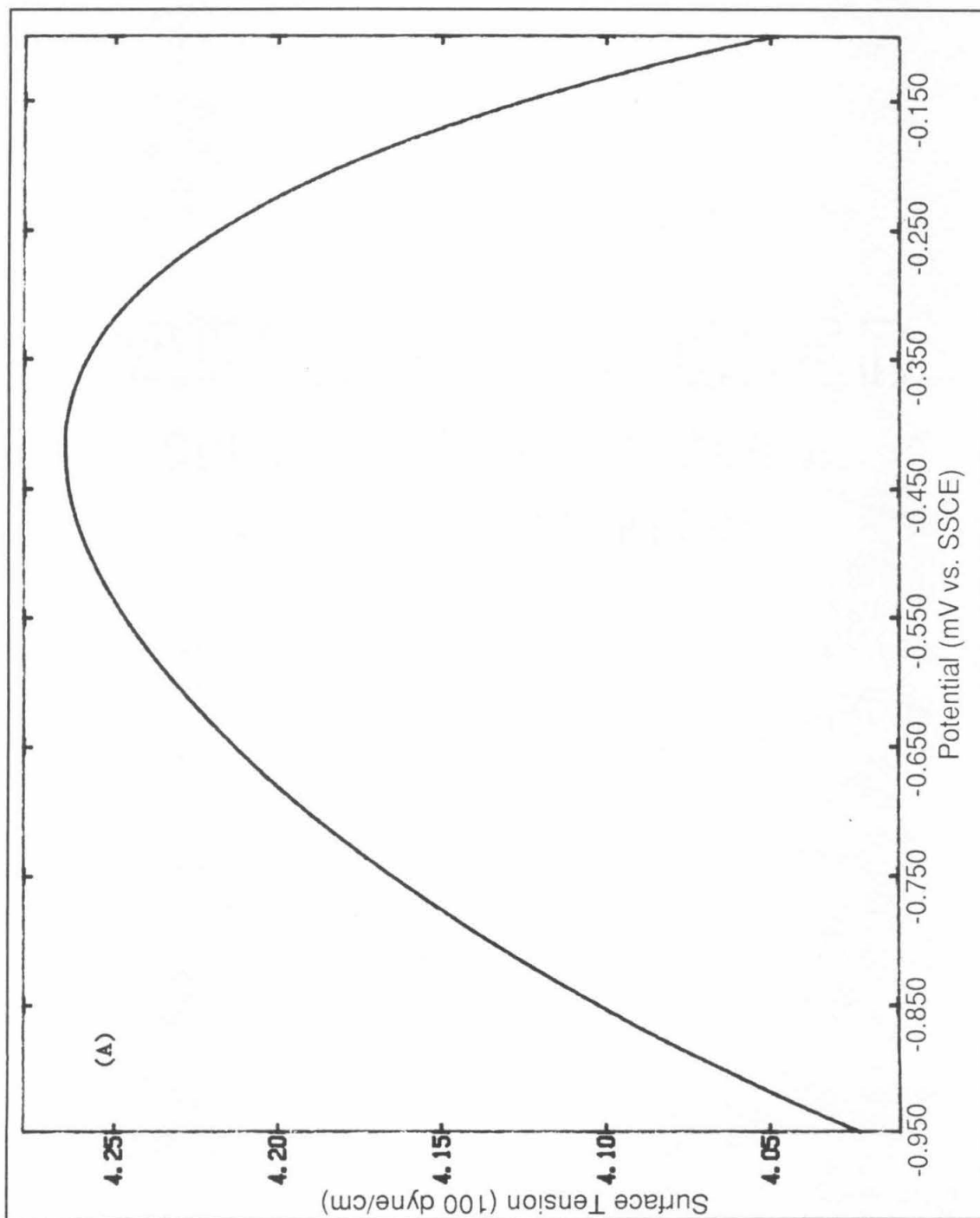
response of the vibration isolation system. A three-point suspension system will give rise to torsional low frequency normal modes and coupling between these modes and the translational low frequency normal modes of the building will be inefficient. Thus, the vibration isolation scheme employed here has wide effective bandwidth.

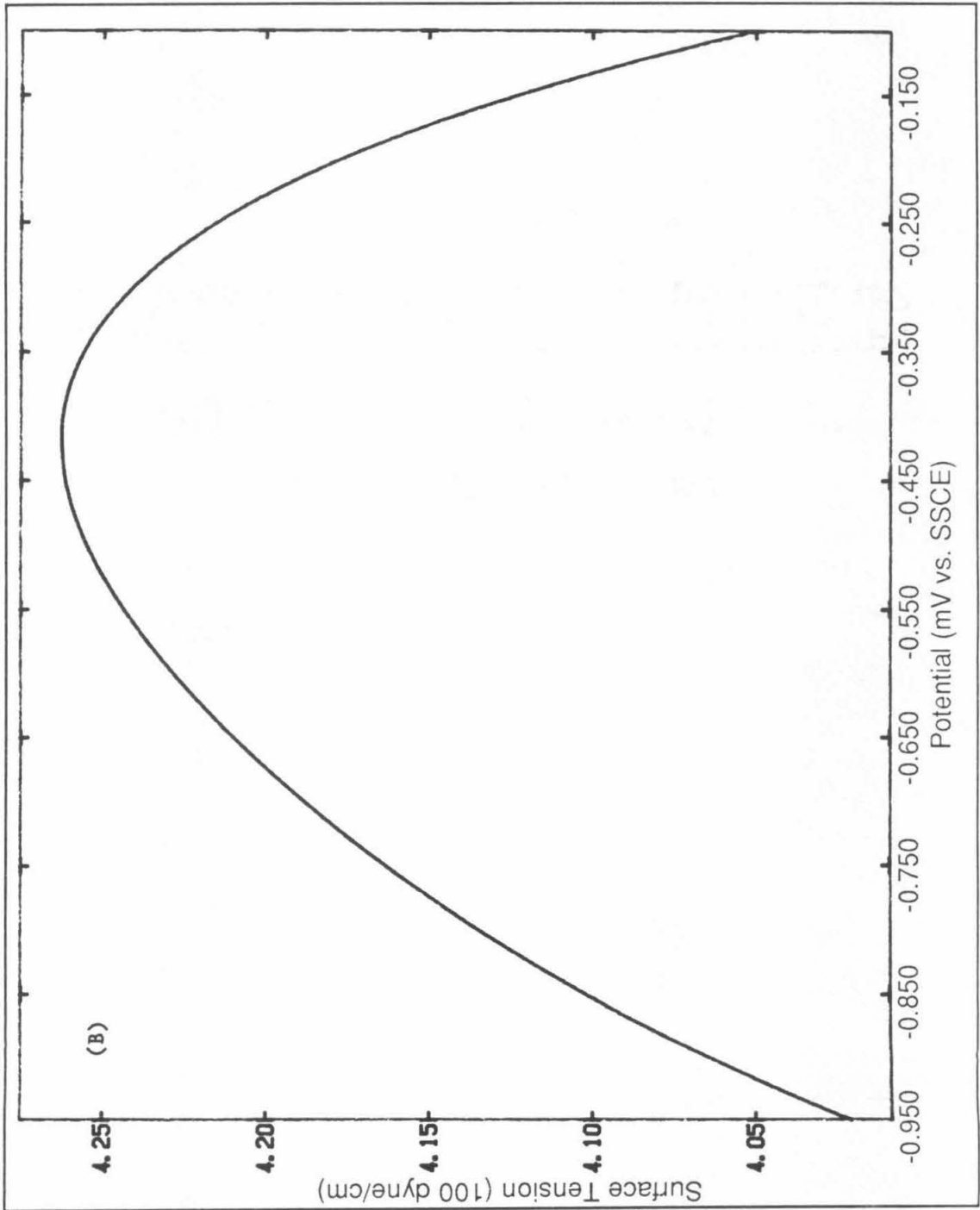
#### Equilibrium Surface Tension Measurements.

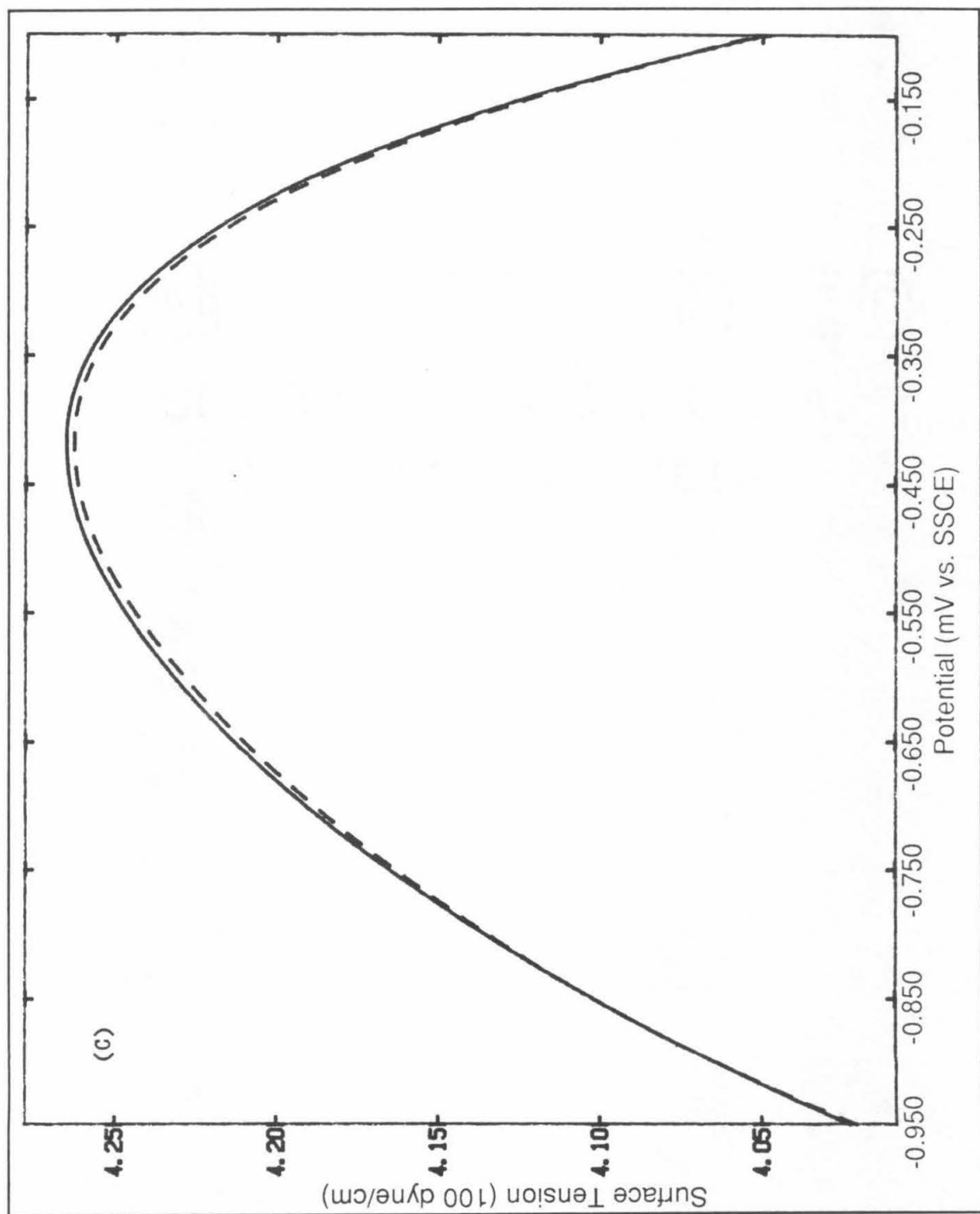
The reliability of the Wilhelmy technique was established by measuring the equilibrium electrocapillary response of the mercury-0.01 M aqueous NaF interphase and comparing it to literature values obtained by the maximum bubble pressure technique (Figure 4).<sup>5</sup> Evaluating the surface tension in the region of the ECM was complicated somewhat by low frequency fluctuations in the time-series data. Operating under the assumption that these fluctuations were a real effect (*vide infra*), points near the ECM were evaluated by taking maximum values rather than an average. The electrocapillary curve in Figure 4a was obtained by stepping the cell potential in 5 mV increments and allowing the observed surface tension to attain a constant value. The electrocapillary curve obtained from Wilhelmy plate data (Figure 4a) was qualitatively very similar to the electrocapillary curve obtained by the maximum bubble pressure method (Figure 4b) providing good empirical support for the reliability of the Wilhelmy method.

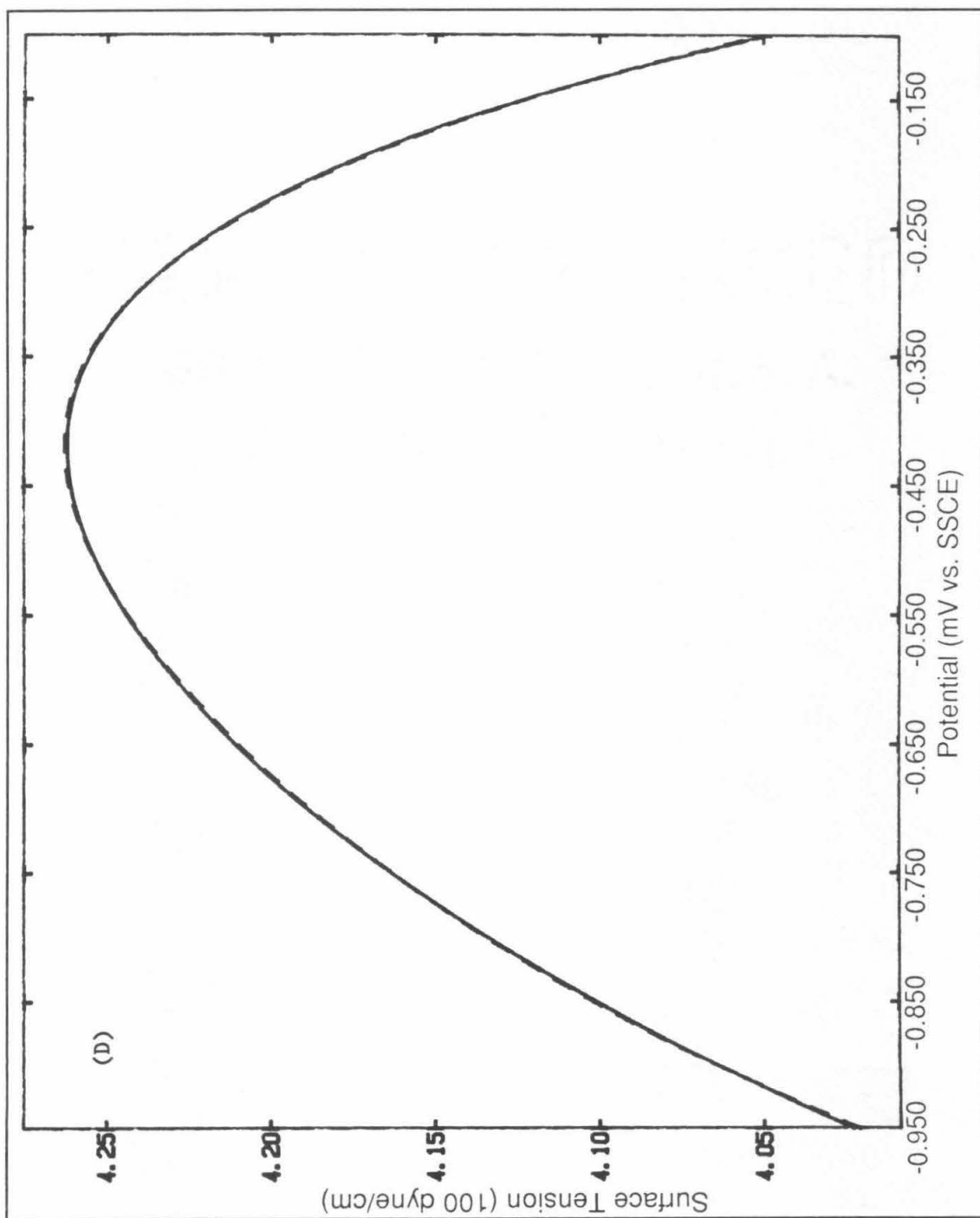
Figure 4c illustrates that the primary difference between the curves obtained by the two different methods occurs in the vicinity of the ECM where the Wilhelmy method appears to systematically overestimate the surface tension by a small amount. However, because

Figure 4. (A) Equilibrium electrocapillary curve for 0.01 M NaF constructed from maximum values of the surface tension observed at each potential for five minutes and obtained using the Wilhelmy plate technique described here (see text). (B) Equilibrium electrocapillary curve for 0.01 M NaF obtained by Mohilner (ref. 5) using a maximum bubble pressure instrument. (C) Superposition of the equilibrium electrocapillary curves from (A) (solid line) and (B) (dotted line). (D) Superposition of an equilibrium electrocapillary curve obtained as in (A) but using average values from each potential (solid line) and the curve from (B) (dotted line).









the maximum bubble pressure technique gives an average value of the absolute surface tension, it may underestimate the surface tension if fluctuations in the surface tension near the ECM are large. This point is demonstrated in Figure 4d where the surface tension data obtained by the Wilhelmy plate was averaged and the resulting electrocapillary curve superimposed onto the literature values. The curves here are nearly identical as expected. The value for  $K$  in equation (3) was evaluated from the electrocapillary curve constructed from averaged data (Figure 4d). The value obtained,  $497.8 \text{ s}^{-2}$ , was fairly close to the value of  $490.2 \text{ s}^{-2}$  that was estimated by measuring the perimeter of the plate without including surface roughness effects. The difference between Figure 4c and 4d is small but well within the sensitivity limits of the two techniques and demonstrates the need to account for fluctuations when determining surface tension near the ECM to high precision.

#### Linear Sweep Voltammetry with Concomitant Measurement of Surface Tension.

An electrified interphase that is composed of pure supporting electrolyte across which no electron transfer can occur is known as an "ideal" polarizable interphase.<sup>1, a, f, g</sup> Electrochemical systems of this sort at thermodynamic equilibrium have been extensively studied and are responsible for much of the conventional paradigm (*i.e.* "double-layer" model) of the electrified interphase.<sup>1, 7</sup> Conventional analysis of electrified interphases predicts that the surface tension, and hence, the free energy of the interphase is related directly to the excess charge density on the electrode through

the Lippmann equation, e.g.;<sup>1</sup>

$$\sigma^M = - \left( \frac{\partial \gamma}{\partial \phi} \right)_{\mu_i}$$

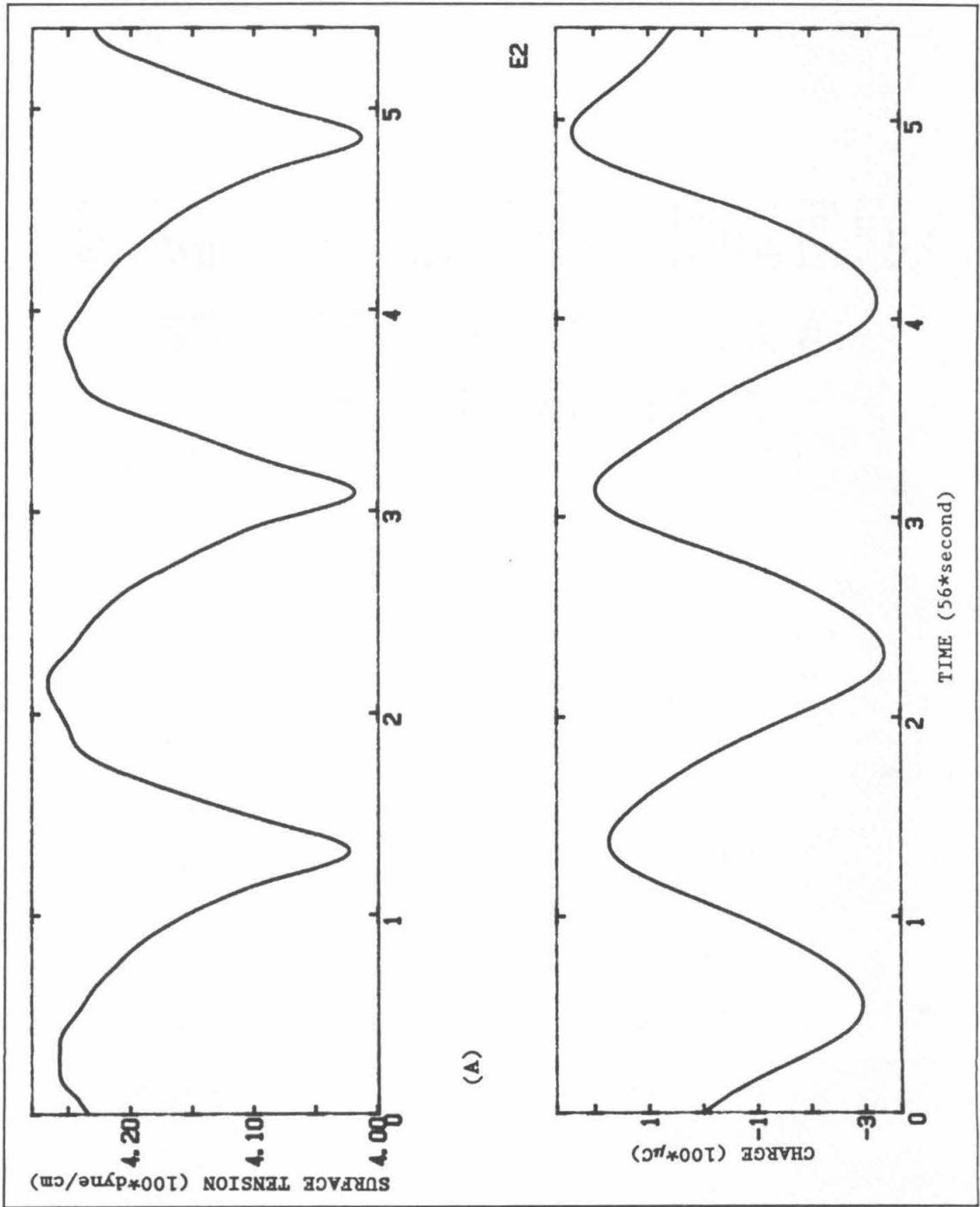
Therefore, at thermodynamic equilibrium the slope of the electrocapillary curve should be related directly to the measured excess charge density on the electrode. This equation should also hold in the non-equilibrium case as long as the rate of charge transport to or from the electrified interphase is much slower than other relaxation processes. Thus, changes in the observed charge density at the electrode due to excursions in the applied electrostatic potential should be exactly in phase with changes in the surface tension, although opposite in sign.

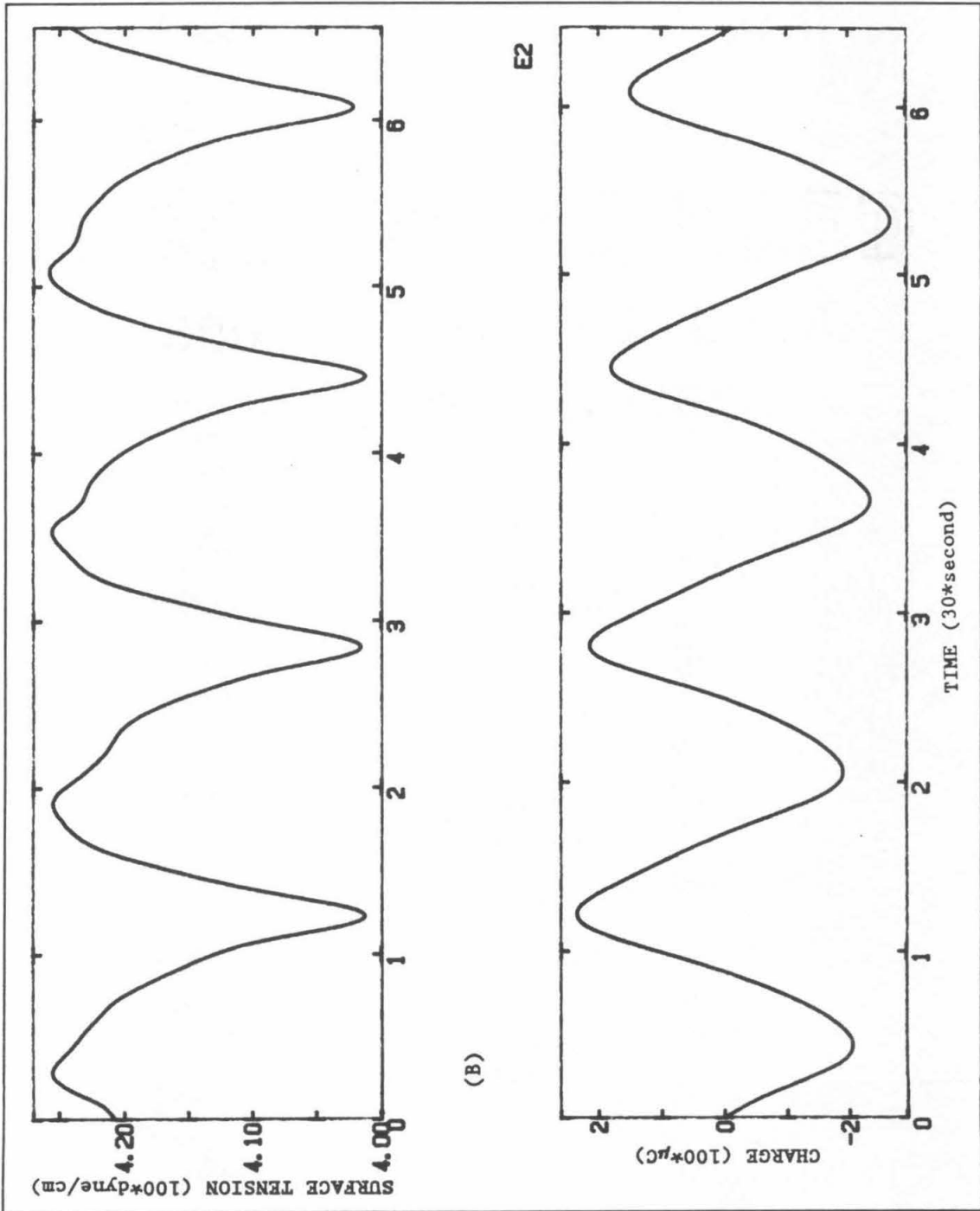
One convenient and simple technique for testing the hypothesis of mass-transport limited relaxation is linear sweep voltammetry (LSV). Mass transport will not become a limit until scan rates of ca.  $10^4 \text{ Vs}^{-1}$  are achieved<sup>1c-e</sup>, and the interphase can be assumed to be in statistical equilibrium for all scan rates that are practical at the very large electrodes used in this study (e.g.  $\leq 500 \text{ mVs}^{-1}$ ). LSV is also a useful technique for probing the behavior of species that undergo electron-transfer reactions with the electrode. Direct knowledge of the state of a non-equilibrium or steady-state interphase through which electric current is passing is desirable in many cases, especially if the reactant is absorbed. Because the Wilhelmy technique has the capacity to monitor dynamic and non-equilibrium surface tensions, it has the potential for ancillary monitoring of the state of the interphase while current due to ion-motion or

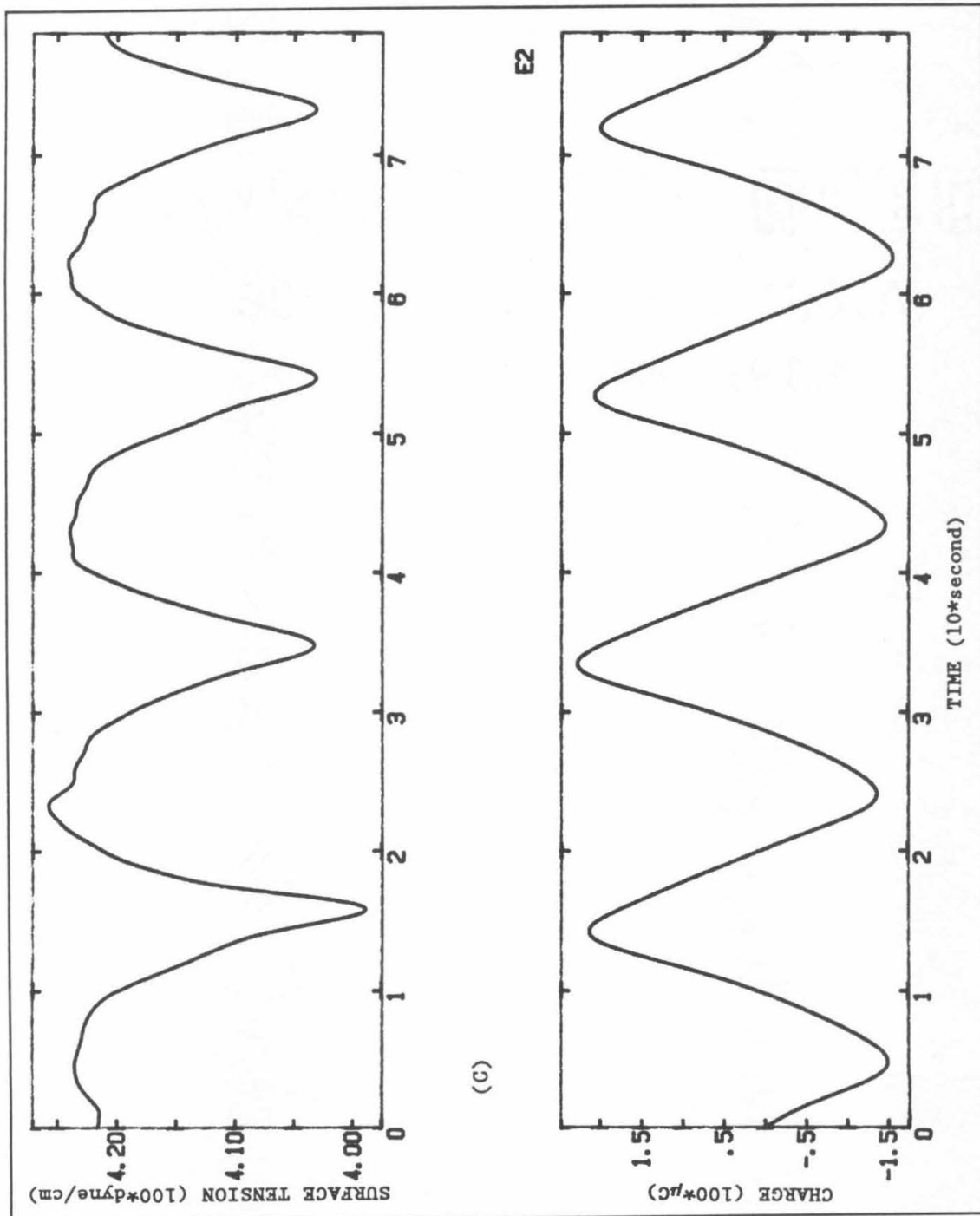
electron-transfer is flowing. To demonstrate this capacity, the output of the electrobalance, the potentiostat and the current follower during an LSV experiment were monitored simultaneously at ~20 Hz on three channels of an analog-to-digital converter driven by an IBM AT microcomputer.

The time-resolved surface tension and charge density obtained during LSV experiments with a 0.1 M NaF aqueous electrolyte solution at three different sweep rates is displayed in Figure 5. The top window of Figure 5a displays the time-resolved surface tension response as the potential is swept from -0.450 V vs. SSCE to -0.950 V at 10 mVs<sup>-1</sup>. The bottom window displays the charge density (integrated current) that was measured concomitant with the surface tension. The scale of the time axis is the same for both windows. The charge density in this case appears to be exactly in phase with the surface tension as expected from the Lippmann equation. However, when the scan rate is increased to 20 mVs<sup>-1</sup> (Figure 5b) the surface tension begins to lag behind the current. At 50 mVs<sup>-1</sup> (Figure 5c) the surface tension clearly is no longer in phase with the current. There are two possible explanations for this behavior; i) the Wilhelmy plate, the electrobalance or both have extremely slow response times, or ii) the hypothesis of mass-transport limited relaxation in non-equilibrium electrochemical systems is incorrect for the 0.1 M NaF system. Because a breakdown of the assumption of mass-transport limited relaxation has wide ranging consequences, the issue of unusual experimental limits on the response time of the Wilhelmy plate instrument will be addressed carefully.

Figure 5. Surface tension and integrated current obtained during linear sweep voltammetry for aqueous 0.1 M NaF at three different sweep rates. Upper windows display the time-resolved surface tension response of the interphase. Lower windows display the charge. The time axis for both windows is identical. Potential was ramped from -0.950 V to -0.450 V and measured with respect to a SSCE reference electrode. Initial potential was -0.500 V. (A) 10 mV/s. (B) 20 mV/s. (C) 50 mV/s.





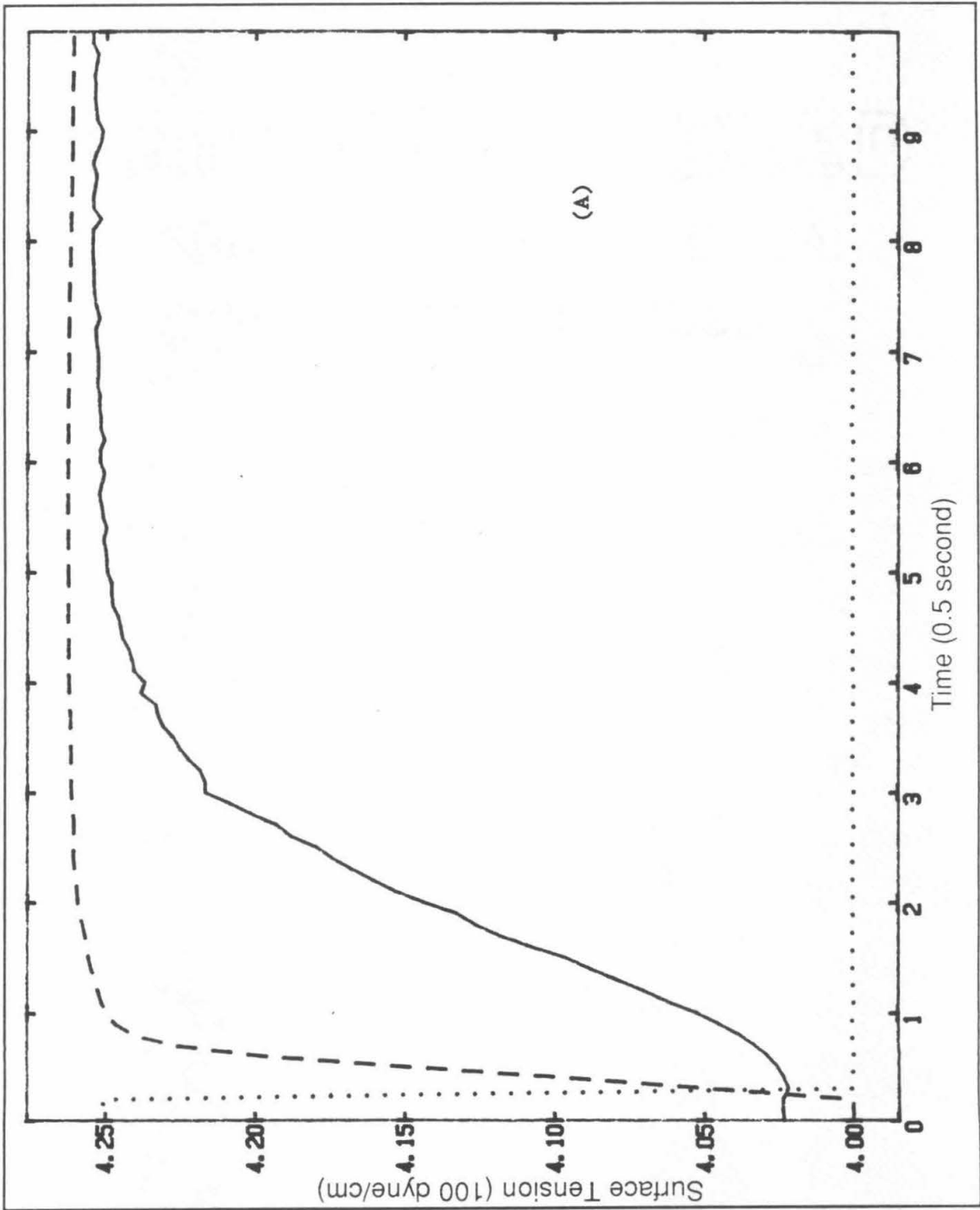


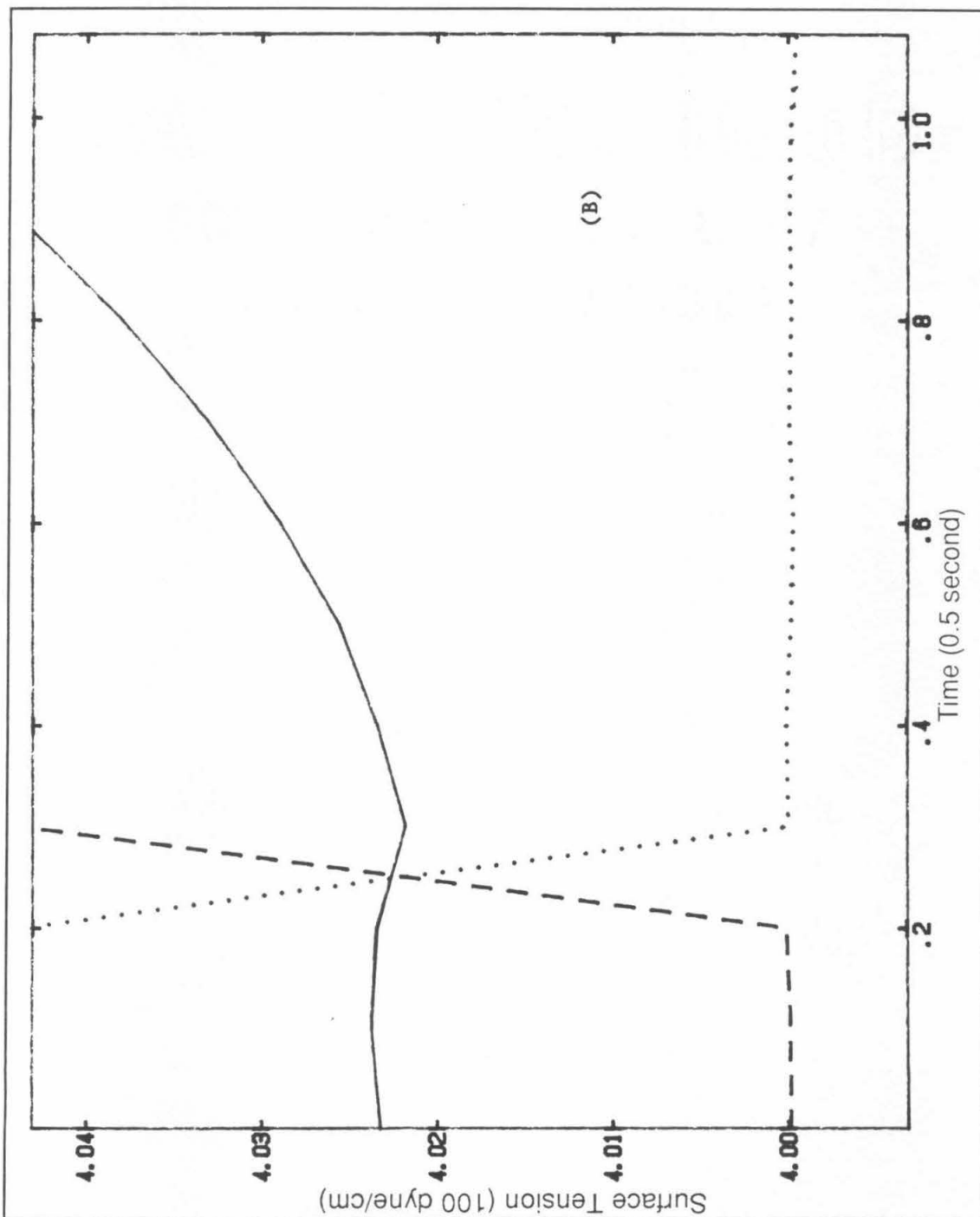
### Limits to the Response Time of the Wilhelmy Plate Technique.

The Wilhelmy Plate technique has been used to measure dynamic surface tension for several decades and response times for instruments that employ recording electrobalances are reported to be between 0.001 and 0.01 sec. for the air-water interphase.<sup>6</sup> Thus, it is unlikely that the instrumental response time of the recording electrobalance contributes to the observed phase lag in the surface tension during LSV experiments at scan rates larger than  $10 \text{ mVs}^{-1}$ . The other potential source of slow instrumental response is an inertial limit to the movement of the mercury meniscus. However, the largest possible change in surface tension at the air-mercury interphase (ca.  $420 \text{ dyne cm}^{-1}$ ) would require only 0.028 sec. to re-establish mechanical equilibrium (Appendix II).

To test the response time of the instrument in more detail under the experimental conditions employed here, the surface tension response to a step function in the applied electrostatic potential was observed. Figure 6a displays the time-resolved surface tension, applied potential and charge density that were measured concomitantly during a potential step from -1.000 V to -0.550 V with 0.1 M NaF as the supporting electrolyte. The surface tension and charge density responses clearly are occurring on very different time scales. The charge density requires ca. 0.3 sec. to relax completely, whereas the surface tension appears to require 4-5 sec. to reach a steady state. However, as illustrated in Figure 6b, the surface tension measurement begins to change within 0.05 sec. of the voltage step, indicating that the response time of the instrument is at least as fast as the time

Figure 6. (A) Concomitant measurement of surface tension, charge density and applied electrostatic potential for a 0.1 M NaF supporting electrolyte solution during a chronotensiometric experiment in which the applied potential was stepped from -1.000 V to -0.550 V vs. SSCE. The solid line is the surface tension, the dotted line is the applied electrostatic potential and the dashed line is the current. (B) Expanded view of (A) in the vicinity of the potential step.





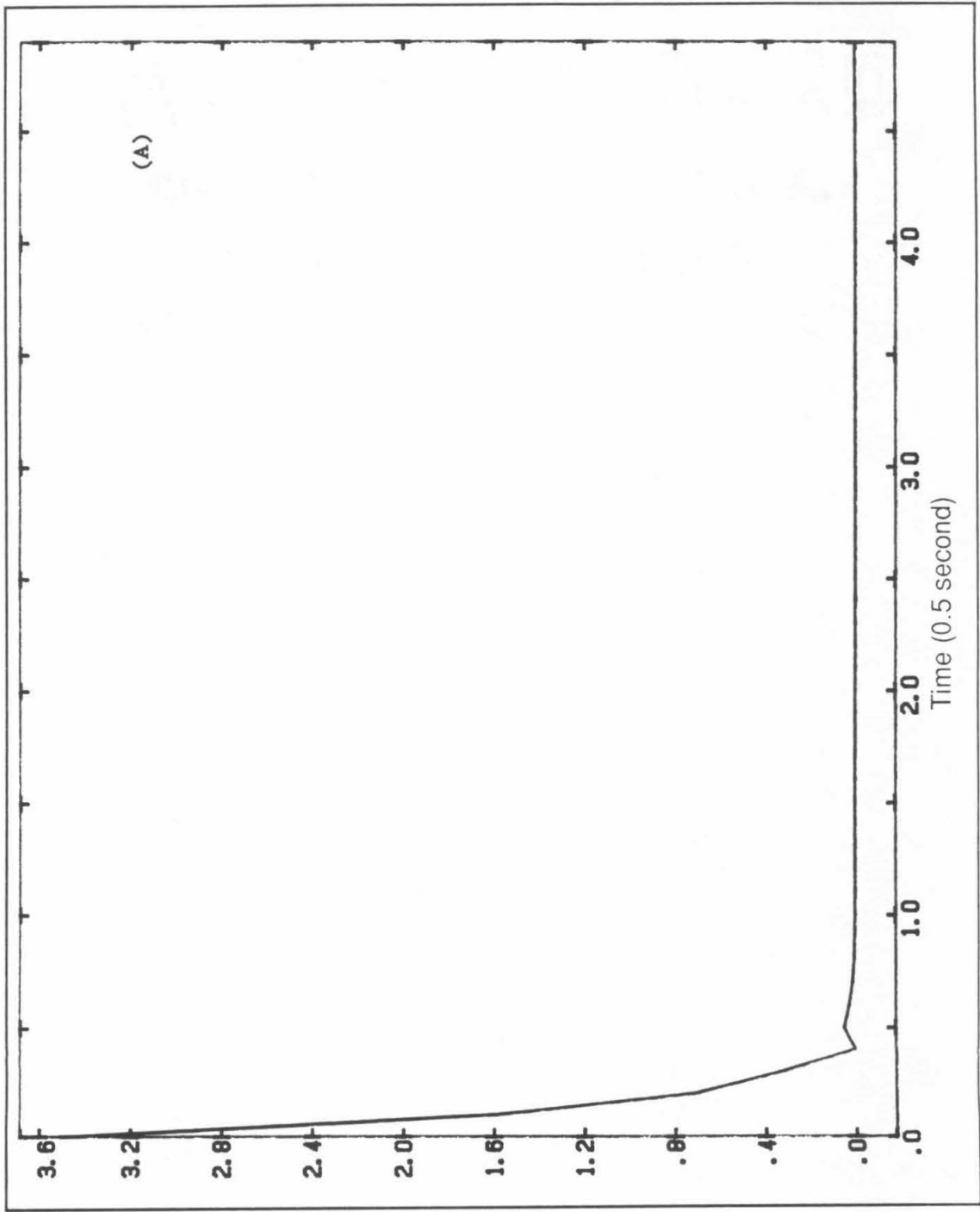
resolution of the analog-to-digital converter. Although electronic and inertial factors can be eliminated as potential causes of the slow response time of the instrument, the prospect of bizarre or non-obvious effects remains. A clear demonstration that the observed response is due to molecular processes and not unknown or overlooked electromechanical effects is desirable.

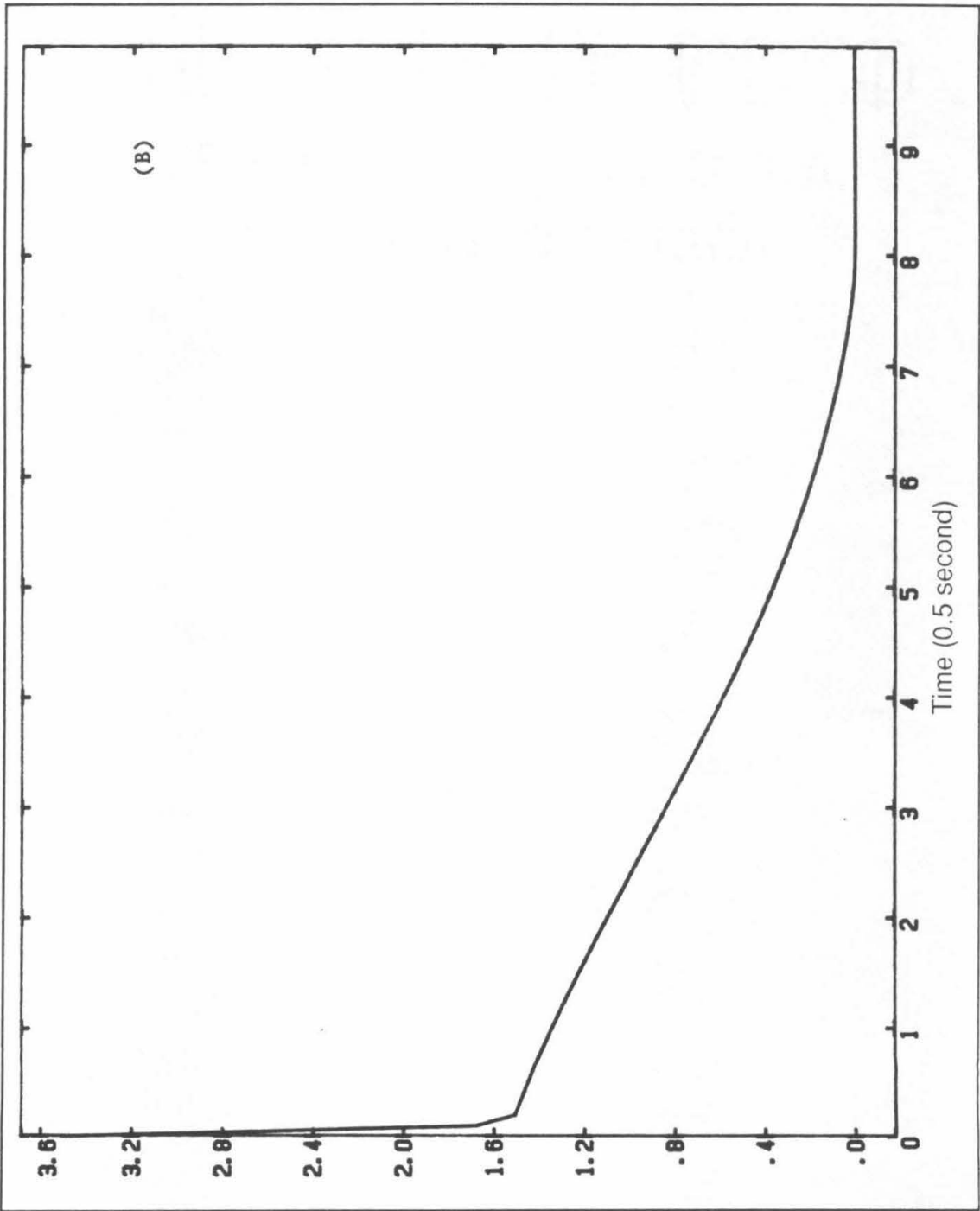
The existence of observable intrinsic fluctuations in the surface tension at any given applied electrostatic potential provides a ready test for the origin of the observed dynamical response. If these fluctuations arise from thermally-driven molecular events within the interphase, then the autocorrelation function,  $C(\tau)$ , of the intrinsic surface tension fluctuations should be related to the dynamical behavior of the system in response to the application or removal of an external force (e.g. applied electrostatic potential).<sup>9</sup> On the other hand, if fluctuations in the surface tension are due to mechanical or acoustic noise, then  $C(\tau)$  will not be related to the observed response or relaxation function and will be nearly identical for a Wilhelmy plate positioned at an electrified interphase and one that is hanging freely in air or water. The autocorrelation function is defined as the limit as  $t \rightarrow \infty$  for the integral;<sup>9a</sup>

$$C(\tau) = t^{-1} \int [(y(t) - \langle y(t) \rangle)(y(t + \tau) - \langle y(t) \rangle)] dt \quad (4)$$

Where  $\langle y(t) \rangle$  is the time average of the observable  $y(t)$ . Accurate evaluation of this integral for discrete-time data requires very large data sets and 50000 points were used in this study. Figure 7a displays  $C(\tau)$  evaluated for a Wilhelmy plate that was hanging freely in an aqueous 0.1 M NaF solution. The data was acquired at 20 Hz to

Figure 7. Autocorrelation functions for the steady state electrobalance output signal. (A) Wilhelmy plate suspended and immersed in an aqueous 0.1 M NaF electrolyte solution. (B) Wilhelmy plate positioned at the electrified mercury-0.1M NaF electrolyte interphase. Applied electrostatic potential was -0.550 V vs. SSCE.





be compatible with the experimental data presented in Figure 6.  $C(\tau)$  drops rapidly to zero as expected for uncorrelated white noise. However, when the Wilhelmy plate is positioned at an electrified interphase with an applied electrostatic potential of -550 mV,  $C(\tau)$  has an entirely different form as illustrated in Figure 7b. The autocorrelation function of the white noise displayed in Figure 7a is still present in Figure 7b, but additional processes that serve to extend the correlation time by several orders of magnitude also are operative.  $C(\tau)$  in Figure 7b requires nearly 3.5 sec. to decay to zero.

The response or relaxation function for some observable often is related to the autocorrelation function for intrinsic fluctuations of that observable by a formalism that was developed within the context of non-equilibrium statistical mechanics.<sup>9</sup> For the most simple case of a linear response functional that can be approximated successfully by the first term of its Taylor series expansion (i.e. "linear response function theory") the response function is related to  $C(\tau)$  by;<sup>9a</sup>

$$\psi(t) = \beta(\sigma^2 - C(\tau)) \quad (5)$$

where  $\sigma^2$  is the variance in the intrinsic fluctuations of the observable. Note that  $\sigma^2 = C(0)$  in the linear response function theory limit by virtue of the ergodic hypothesis. Examination of Figure 6a and Figure 7b shows clearly that equation (5) is not an appropriate relation for the systems being considered here. However, equation (5) is only valid for very simple and linear systems that are Markovian, Gaussian and ergodic.<sup>9c</sup> These are not terms that are likely to be

useful for characterizing a complex and anisotropic system such as the electrified interphase. Relations such as equation (5) can be written in very general form for linear and nonlinear response functionals, but they become quite complex and, in general, are intractable.<sup>9c</sup> The purpose here is not to establish a formal relationship between  $C(\tau)$  and  $\psi(t)$ , but to provide evidence for a molecular origin of the observed surface tension response. The relaxation time for  $C(\tau)$  in Figure 7b and the time necessary for the surface tension to achieve a steady state value in Figure 6 are of the same order of magnitude, whereas the relaxation time of  $C(\tau)$  in Figure 7a is much faster. This is good evidence that molecular events are responsible for the observed dynamical behavior of the electrified interphase. Thus, the observed surface tension lag in LSV experiments at slow scan rates and the observed slow response to potential step experiments appear to be a real phenomena and not an experimental artifact.

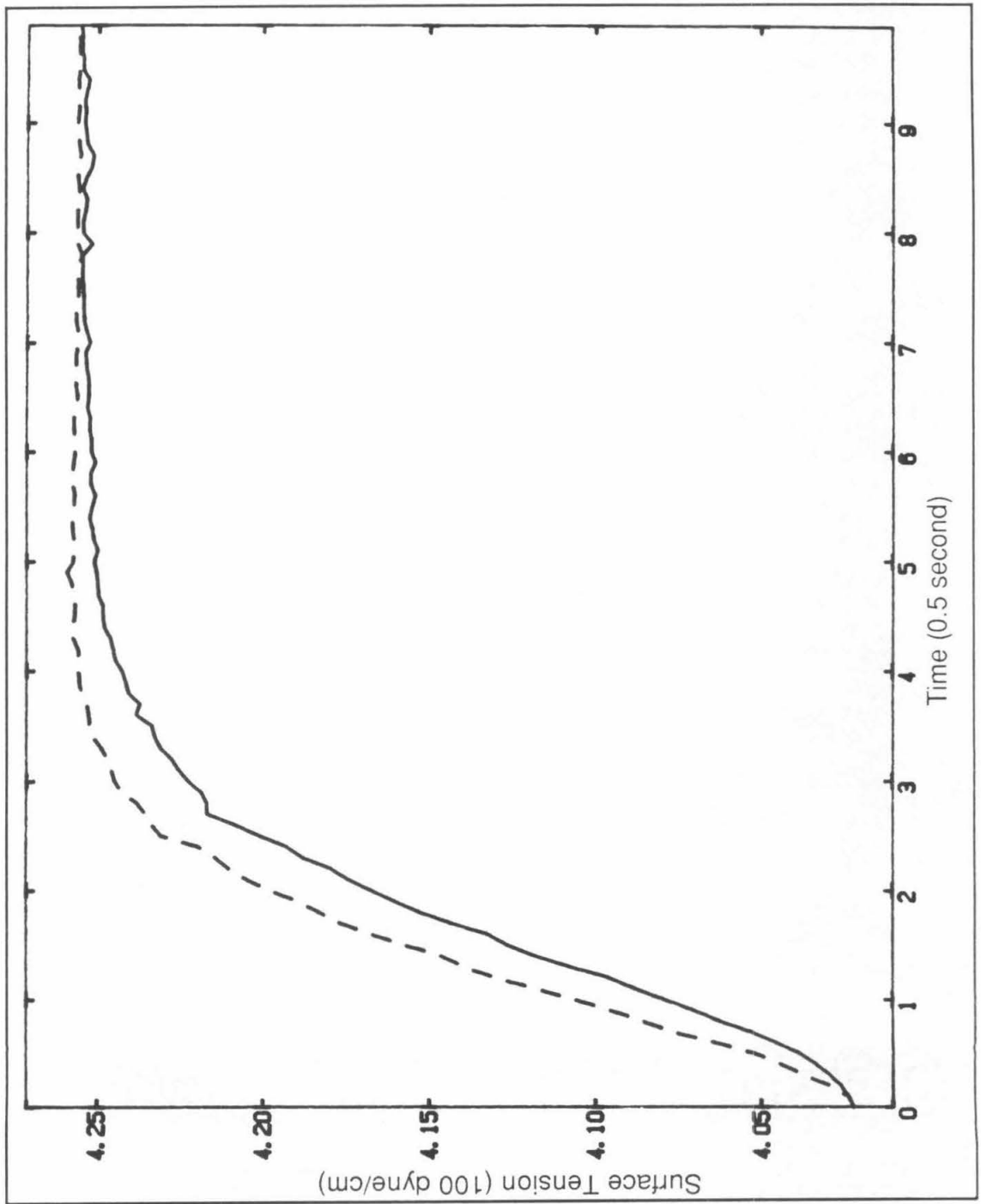
#### Chronotensiometry.

An apt name for the technique of measuring the surface tension response to a step function in the applied electrostatic potential would be chronotensiometry by analogy with the common electrochemical techniques of chronoamperometry and chronocoulometry. The chronotensiometric response of a 0.1 M NaF system displayed in Figure 6 implies that relaxation processes continue for time periods that are long compared to the time necessary to establish a diffusion-migration equilibrium for ionic species. Slow relaxation processes at electrified interphases have been observed and are mentioned frequently in the older literature of electrochemistry. The

E.M.F. of galvanic cells, for example, often reaches equilibrium very slowly and days may be required for attainment of stable electrokinetic potentials. Although Grahame mentioned these effects in his seminal review paper<sup>18</sup> and ascribed them to "polarization resistance", no serious experimental efforts to study polarization relaxation have been forthcoming. Very slow relaxation processes at interphases are a general phenomena not restricted to the electrified interphase, especially for systems that require adsorption/desorption events. For example, the frequency of dielectric relaxation for water that is adsorbed on zeolites and silicon oxide surfaces is between 10 and 30 Hz.<sup>11</sup> Although this is two orders of magnitude faster than the relaxation times observed in Figure 6 it is about eight orders of magnitude slower than the time scale for dielectric relaxation of water in bulk phases.

The exact molecular nature of post-diffusion relaxation processes cannot be determined uniquely by measuring macroscopic observables such as the applied electrostatic potential, the charge density or the surface tension. It is reasonable to hypothesize, however, that the relaxation of the dielectric by processes such as reorientation of dipoles, changes in the solvation of ions and ion-pairing are responsible for the observed relaxation of the surface tension after diffusion-migration equilibrium for ionic species has been established. Mass transport of ionic species is much faster than other relaxation processes because ions move in response to very strong coulomb forces, whereas the dielectric relaxation of the system is driven by thermally-induced fluctuations.<sup>9a</sup> Thus, the data in Figure 6 indicate that thermally-driven relaxation processes are the

Figure 8. Comparison of the time-resolved surface tension response of a 0.1 M NaF supporting electrolyte solution (solid line) and a 0.01 M NaF supporting electrolyte solution (dashed line) to a chronotensiometric experiment where the applied electrostatic potential was stepped from -1.000 V to -0.550 V vs. SSCE. Data was acquired at 20 Hz.



rate-limiting factors for the dynamical response of the electrified interphase and not ion motion as is assumed in most conventional electrochemical analysis.

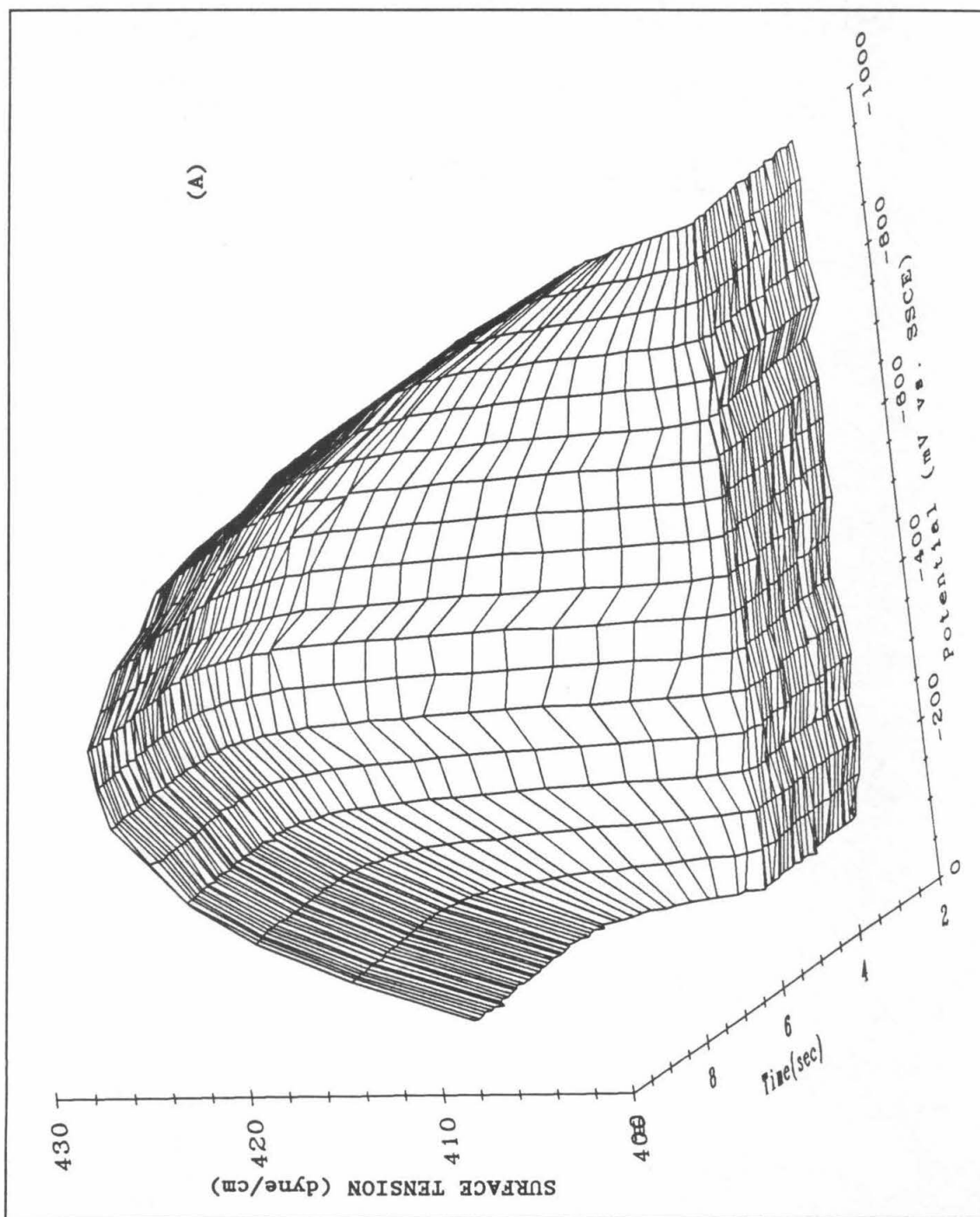
#### Effect of Supporting Electrolyte.

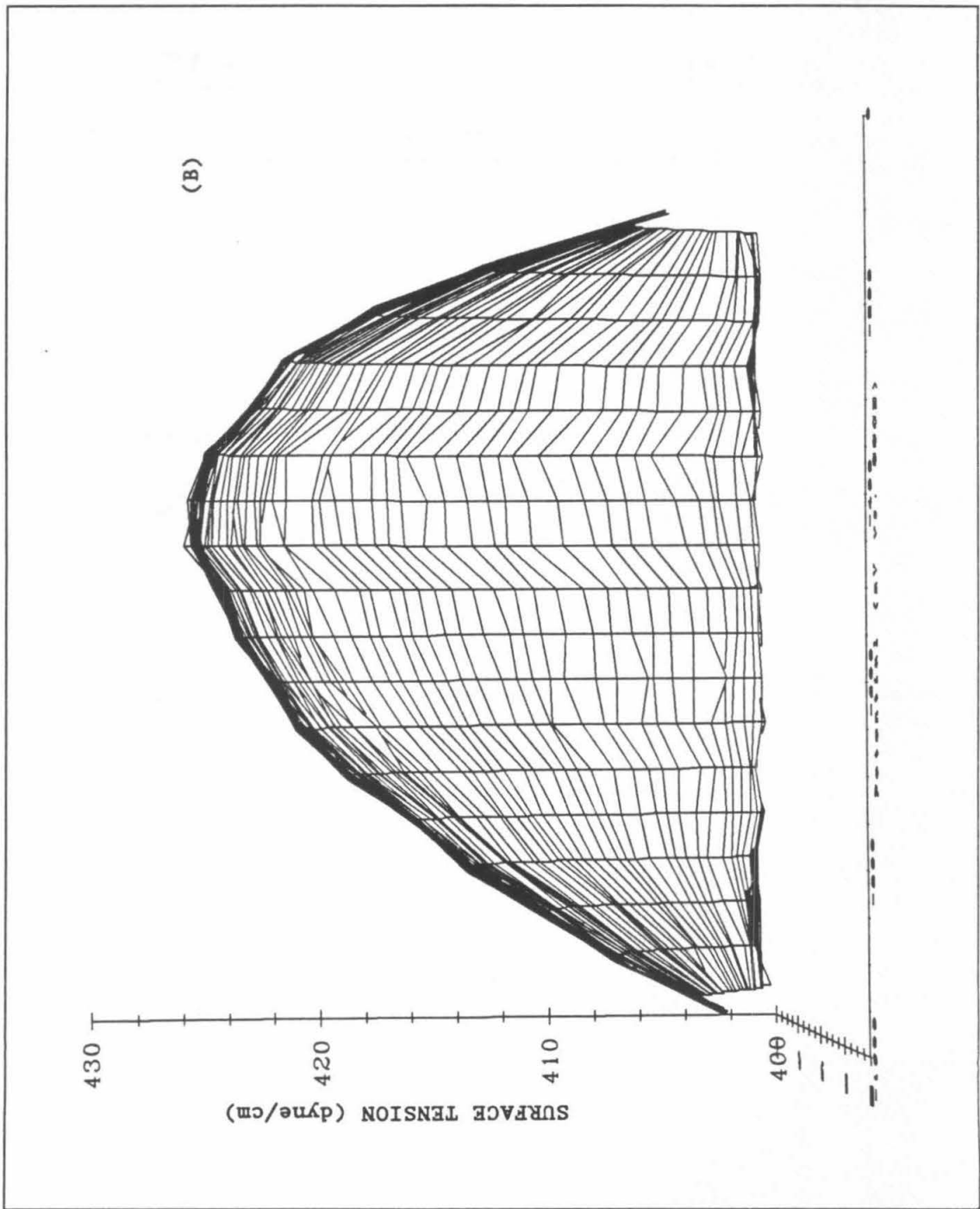
A further test of the validity of the hypothesis that slow relaxation of the surface tension is due to molecular events and not experimental artifacts was provided by examining the effects of supporting electrolyte concentration. Figure 8 compares the time-resolved surface tension response of 0.1 M NaF and 0.01 M NaF. The 0.01 M NaF system clearly relaxes much more quickly than the 0.1 M NaF system. Because changing the chemical composition of the bulk phase adjacent to the electrified interphase causes pronounced changes in the dynamical behavior of the interphase, a molecular origin of the observed behavior is lent further support.

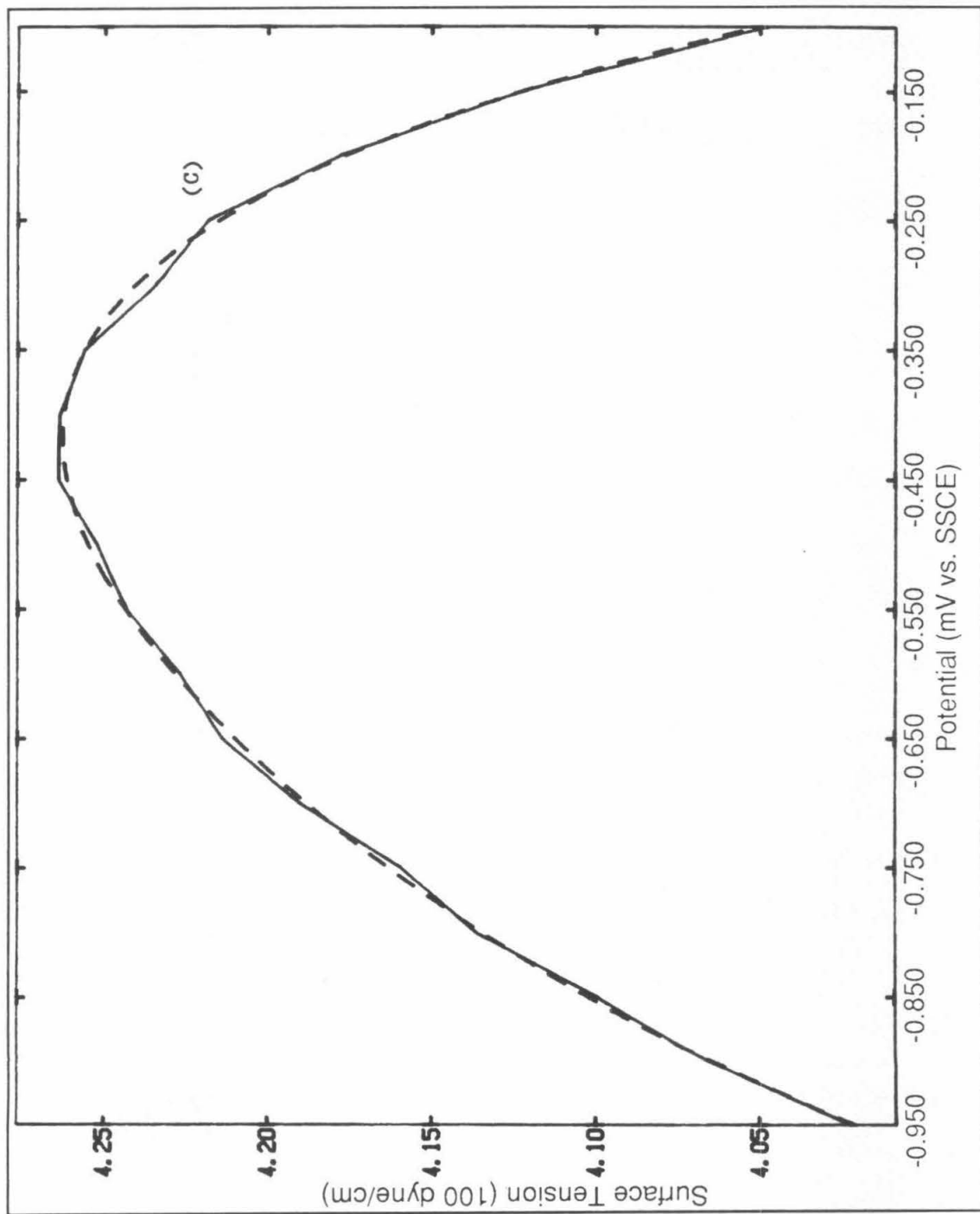
#### Non-Equilibrium Thermodynamic Analysis of Chronotensiometric Responses.

The dynamical behavior of the surface tension at electrified interphases has been treated within the context of non-equilibrium thermodynamics as outlined in chapter 3. In particular, equations (27)-(30)<sup>10a,b</sup> of chapter 3 describe the time-evolution of the surface tension and of the ECM after diffusion-migration equilibrium has been established and under a regime of constant external forces. To proceed with a non-equilibrium thermodynamic analysis of the dynamical response of the surface tension, it was necessary to observe a significant portion of the relaxation function surface for the

Figure 9. (A) Surface tension relaxation function surface of a 0.1 M NaF aqueous supporting electrolyte system for a series of chronotensiometric experiments where the applied electrostatic potential was stepped from -1.000 V vs. SSCE to the potential indicated on the potential axis. (B) Straight on view of the surface in (A) from the steady state end. (C) Superposition of an equilibrium electrocapillary curve obtained from the steady state region of the response function surface 10 sec. after the potential step event (solid line) and from literature values (dashed line).



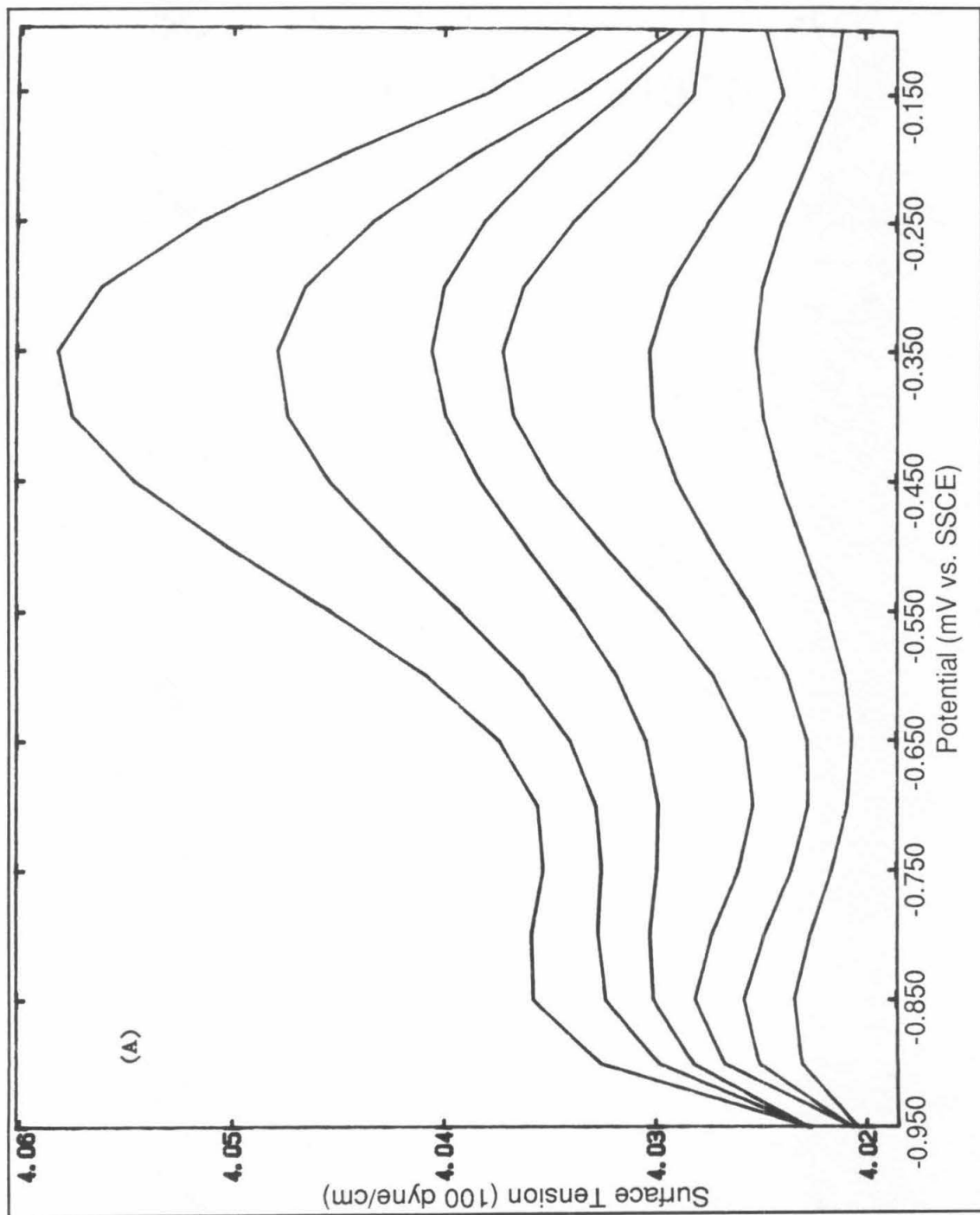




0.1 M NaF system. Figure 9a displays a portion of this surface from -0.100 V to -0.950 V. The surface was obtained by stepping the potential from an initial value of -1.000 V to a more positive potential in 50 mV increments and observing the concomitant surface tension response. The surface has a rather rough appearance due to intrinsic fluctuations in the surface tension and is not smooth as would be expected from equilibrium measurements of the surface tension such as those displayed in Figure 4. Figure 9b displays the relaxation function surface as viewed looking toward the steady state part of the surface. The surface here has a shape that looks qualitatively similar to the equilibrium electrocapillary curves in Figure 4 as expected. Because any two-dimensional slice of this surface at a constant time will yield an electrocapillary curve a direct comparison with equilibrium electrocapillary curves from the literature is possible as illustrated in Figure 9c. The electrocapillary curve obtained in this fashion 10 seconds after the step in applied potential (Figure 9c) is very similar to the equilibrium electrocapillary curve obtained from the literature, although fluctuations in the surface tension give it an irregular appearance.

The non-equilibrium electrocapillary curves obtained during the relaxation event (Figures 10a and 10b) are not scaled versions of the equilibrium curve. The curves in Figure 10a are taken from the first 0.35 sec. of the event and before a diffusion-migration equilibrium had been completely established. The curves denoted by solid lines in Figure 10b are from a section of the surface between 0.6 and 3 sec. after the event. The dotted line in Figure 10b is an electrocapillary

Figure 10. Non-equilibrium electrocapillary curves from the transient regime of the relaxation function surface. (A) 0.1 sec. to 0.35 sec. after the potential step event. Time spacing between curves is 0.05 sec. (B) Solid lines: 0.6 sec. to 3 sec. after the potential step event. Time spacing between curves is 0.2 sec.. Dashed line: 10 sec. after the potential step event. All curves in (A) and (B) were obtained from the ensemble average of 30 separately acquired response function surfaces.





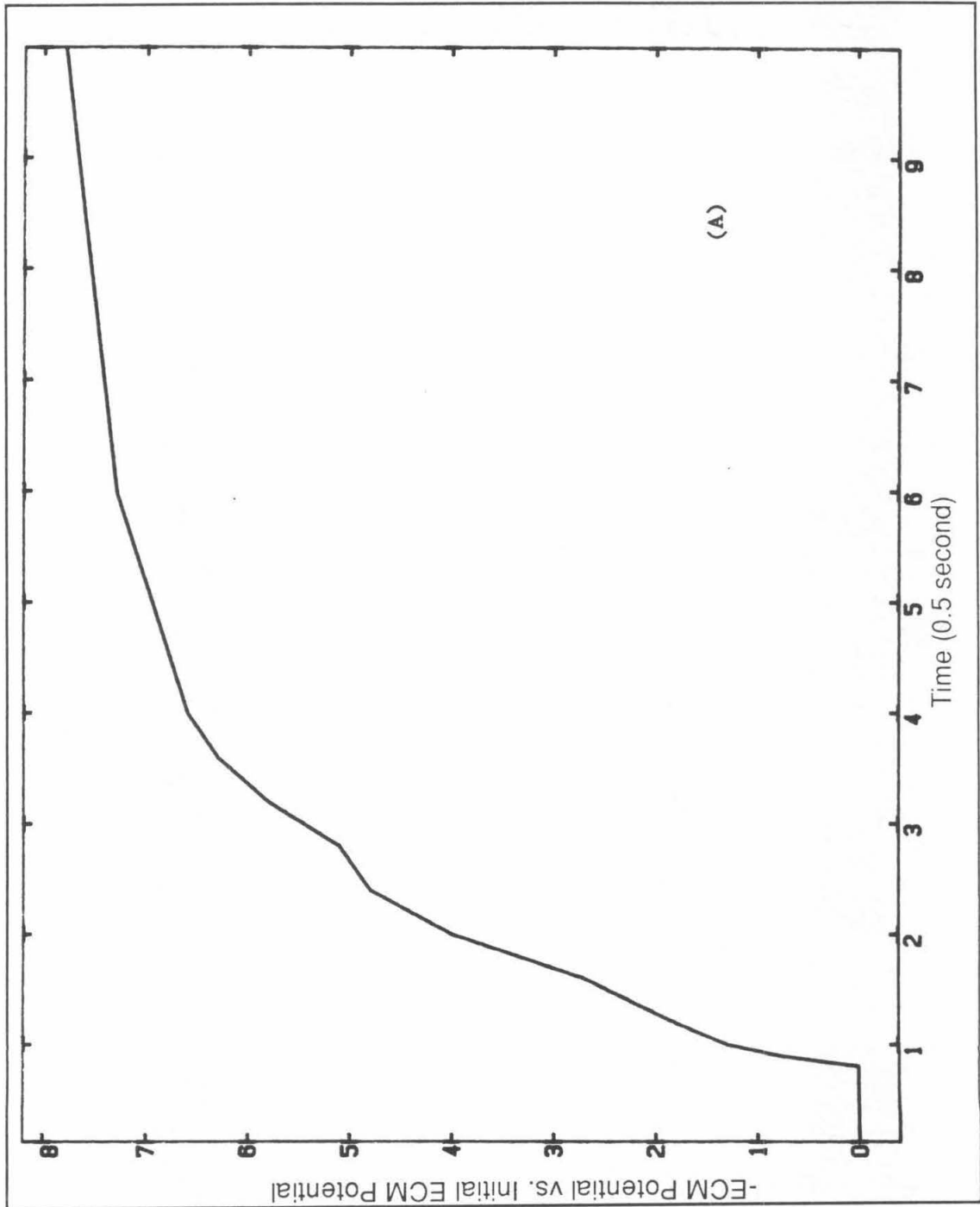
curve from the steady state region of the surface. The curves in Figures 10a and 10b were obtained by ensemble averaging 30 separately acquired relaxation surfaces because fluctuations in the surface tension prevent accurate evaluation of the shape of the curves and the ECM from a single surface. There appear to be two maxima in the non-equilibrium electrocapillary curves at short times (Figure 10a), one at  $-0.350$  V and one at  $-0.870$  V. The more negative maxima begins to disappear after diffusion-migration equilibrium has been attained (ca. 0.3 sec.), but continues to influence the shape of the non-equilibrium curves for at least two seconds (Figure 10b). The other feature of interest in Figures 10a and 10b is that the primary ECM shifts to more negative values with time. However, this behavior does not begin until the charge density has achieved a steady-state value as is evident from Figure 10a where the ECM potential appears to have a nearly constant value of  $-0.350$  V.

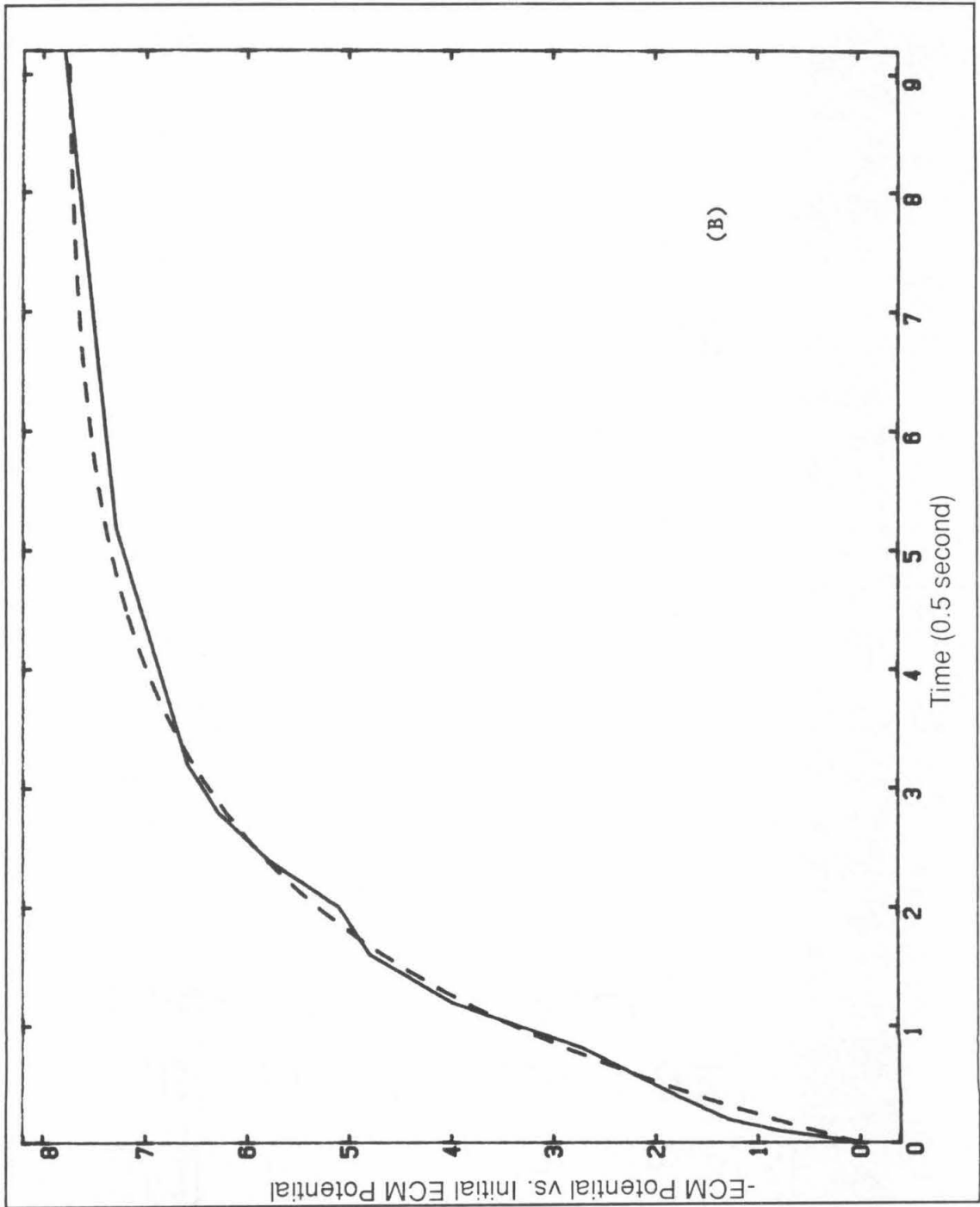
The analysis of Defay and Sanfeld that gives rise to equations (29) and (30) in chapter 3, predicts that the ECM potential should move with time after a diffusion-migration equilibrium has been established. The difference between estimates of the ECM potential for the curves in Figure 10 and the initial ECM potential is plotted versus time in Figure 11a. There is an initial region where the potential of the ECM does not appear to move that corresponds to the time necessary to establish a diffusion-migration equilibrium. After this initial region, the ECM potential appears to move in an exponential fashion toward a limiting value that is the equilibrium potential of the ECM. This was confirmed by fitting the time-varying data in Figure 11a to a single exponential with a time constant of

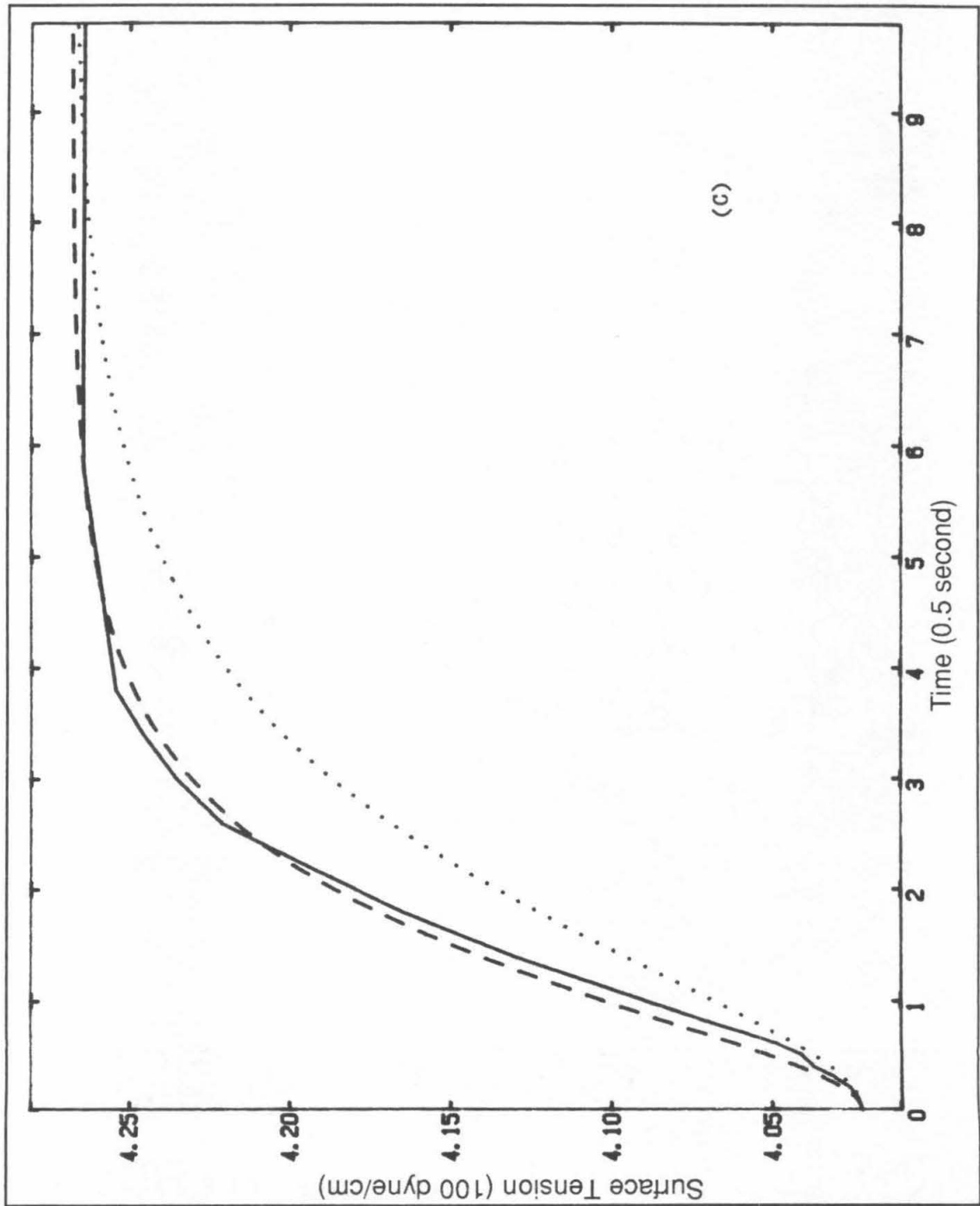
Figure 11. (A) Difference between the initial ECM potential and the ECM potential at different times ( $\Delta\phi$ ) for the non-equilibrium electrocapillary curves displayed in Figure 10.

Absicca scale = 10 mV. (B) Solid line:  $\Delta\phi$  for times after establishment of a diffusion-migration equilibrium. Dashed line: fit of a single exponential decay to the solid line (see text). Absicca scale same as (A). (C) Solid line: experimental values of the time-resolved surface tension for the ECM potential.

Dotted line: values calculated by equation (6) using a time constant of 0.877 sec.. Dashed line: values calculated by equation (6) for a time constant of 0.54 sec..







0.877 sec., *i.e.*;

$$\Delta\gamma_{\text{ECM}}(t) = (1 - \exp(-t/0.877))$$

as illustrated in Figure 11b. This would be consistent with a single process controlling the dynamical response of the ECM potential after establishment of diffusion-migration equilibrium. If this is true then equations (27) and (28) of chapter 3 predict that the dynamical response of the surface tension should obey an equation of the form;

$$\frac{d\gamma}{dt} \approx (1 - \exp(-t/0.877))^2 \quad (6)$$

The solid line in Figure 11c displays the experimental values of the time-resolved surface tension at the ECM and the dotted line the prediction of equation (6). The two curves are not equivalent. Changing the time constant to 0.54 sec. gave the dashed curve in Figure 10c. This curve is also not of the correct form to fit the experimental data, although it has a better qualitative appearance. Additional attempts were made to fit the data from constant values of the applied potential and the results were similar in all cases to those displayed in Figure 11c. Thus, although the analysis of Defay and Sanfeld does predict that the potential of the ECM will shift during a relaxation event, it does not appear to provide an accurate relationship between the dynamical behavior of the ECM potential and the dynamical behavior of the surface tension.

It is important to recognize that the analysis that led to equations (27) through (30) of chapter 3 applies only to local volume elements. The surface tension observable, however, is a global

quantity and relating it to the local surface tension employed in the analysis of Defay and Sanfeld requires an integration over all the volume elements of the interphase. It is probable that this analysis is valid for some volume elements and not for others, but this cannot be determined from measurements of the global surface tension.

Further, the analysis of chapter 3 requires that all aspects of the system be linear. Therefore, the field equations that describe the electrical properties of the system must be linear and gradients and higher order derivatives of state variables must not contribute to the observed response. Experimental evaluation of the ratio of charge density to electrostatic potential at different potentials demonstrates clearly that this ratio is not constant, and is nonlinear for all known electrified interphases. Hence, the field equations that describe the electrical properties of the interphase are also nonlinear. The autocorrelation function for intrinsic fluctuations in the surface tension and the observed chronotensiometric response of the surface tension are not related in a simple way as predicted by linear response function theory providing further evidence that the processes governing relaxation of the interphase are nonlinear. The electrified interphase should, in general, be considered a strongly nonlinear system and the failure of the analysis of chapter 3 to provide an accurate quantitative description of the global surface tension relaxation function is not surprising. The analysis is valuable, however, because it predicts the observed dynamical behavior of the ECM potential and affords insight into a powerful method for analyzing electrified interphases that is not common to contemporary electrochemistry. Conventional electrochemical analysis is not useful

for the phenomena described here because it assumes, *a priori*, that interfacial relaxation is controlled by the diffusion-migration of ionic species.

#### An Alternative Kinetic Model for the Chronotensiometric Response of the Surface Tension.

The global surface tension observable does not carry any direct information about the molecular processes responsible for the observed relaxation function surface. Phenomenological analysis based on non-equilibrium thermodynamics is useful and yields the prediction that the ECM potential of non-equilibrium electrocapillary curves will shift with time, but cannot address directly the question of mechanism. However, the form of equation (6) and the "s-like" shape of the dynamic surface tension curves displayed in Figures 5a and 10c suggests a mechanism based on the kinetics of adsorption processes that may be necessary to change the state of the interphase.

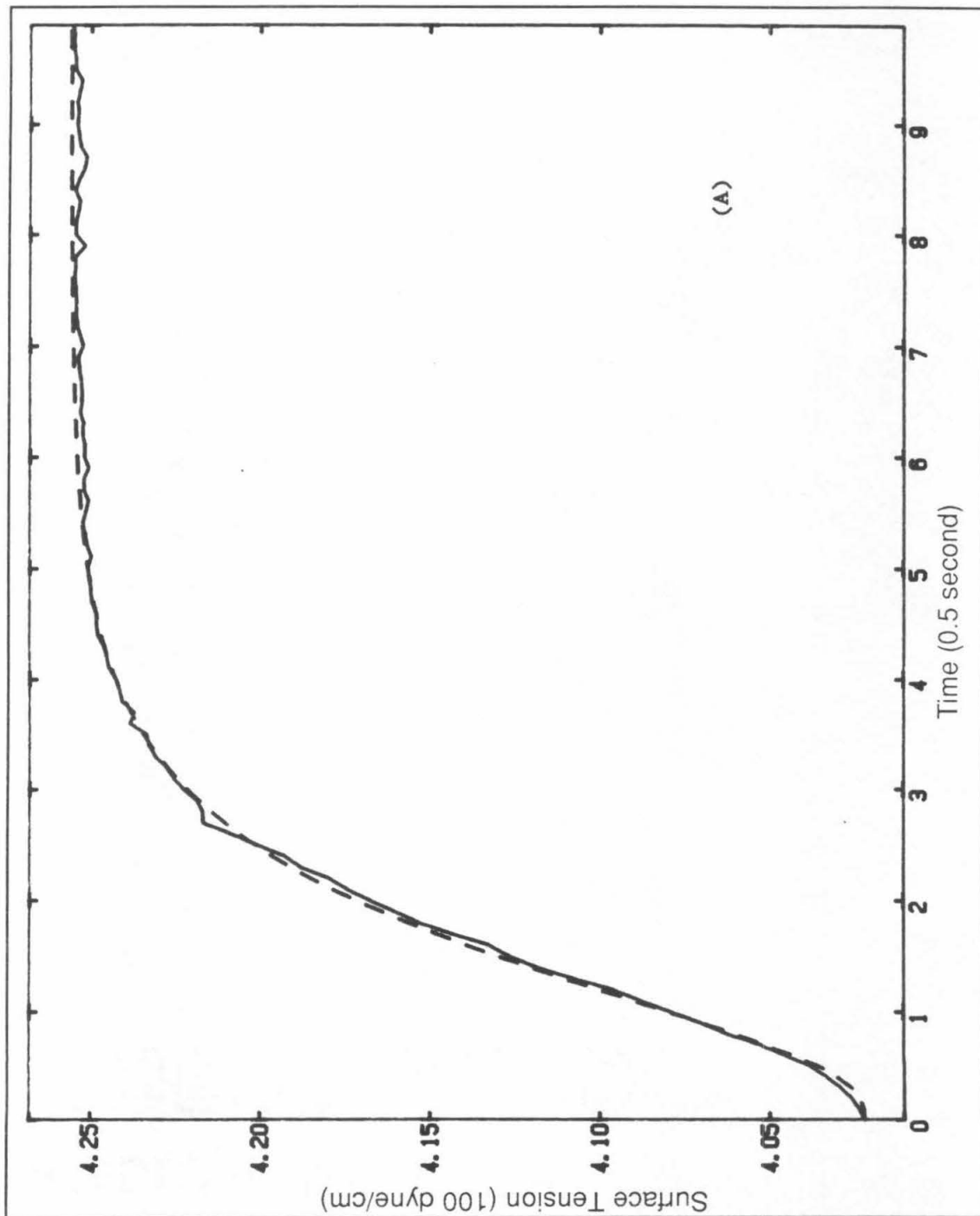
Assume that the surface consists of a large number of adsorption sites and that these sites are in one of two possible states. For example, they might be occupied by water molecules that could be oriented either with the interfacial electric field or against it or they could be occupied by ions that were either free or contact ion-paired with their co-ions. Assume further that a small fraction of these sites must change their states whenever the applied electrostatic potential is changed and that changing the state of a site requires  $n$  simultaneous first order processes. The dynamical response of a system like this will obey a relation of the form;

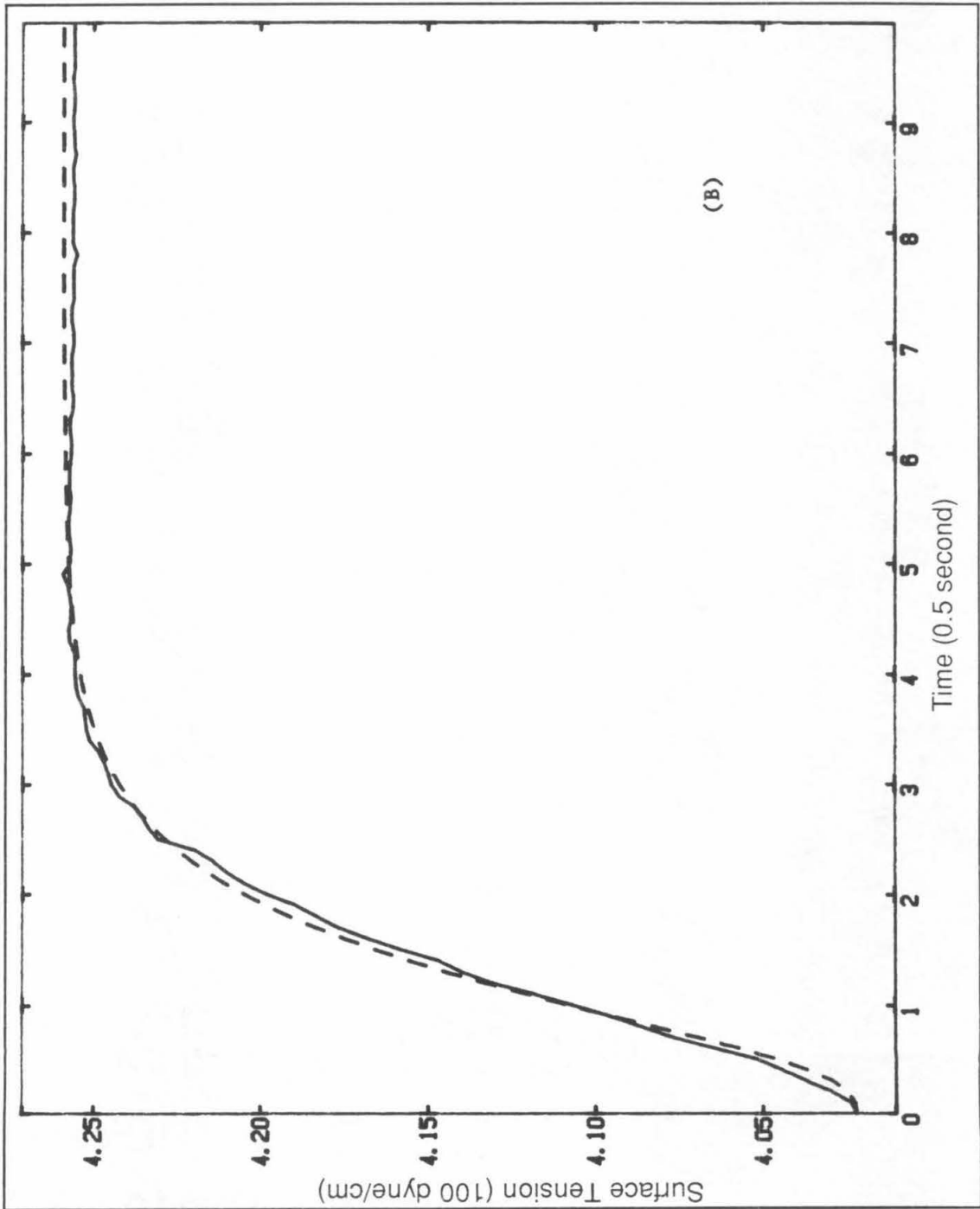
$$\gamma(t) = \Delta\gamma(1 - \exp(-t/\tau))^n \quad (7)$$

An example of this sort of physical system is found in neurons where the time-resolved conductance of a neuron is found to obey equation (7) where  $n = 4$ . The conventional explanation of this behavior is that changing the state of ion channels in the neural membrane requires four simultaneous first order events.

Figure 12 displays the chronotensiometric response of the surface tension for an aqueous 0.1 M NaF system (Figure 12a) and an aqueous 0.01 M NaF system (Figure 12b) as well as the predicted curves based on equation (7) with  $n = 3$  (dashed lines in Figures 12a and 12b). Both calculated curves fit the data rather well, lending some support to a kinetic model that requires three simultaneous first order processes to change the state of an adsorption site. The value of  $\tau$  was 0.51 sec. for Figure 12a and 0.41 sec. for Figure 12b. Although adsorption processes are likely to be important for the dynamical response of any interphase, the caveat that equation (7) can arise from a wide variety of physical processes must be added. Without independent knowledge of  $\tau$  or an understanding of why  $\tau$  depends on the chemical composition of the bulk electrolyte phase, an adsorption model is just one among many.

Figure 12. Solid lines: experimental values of the time-resolved surface tension for a chronotensiometric experiment. Potential was stepped from -1.000 V to -0.550 V vs. SSCE and data was acquired at 20 Hz. Dashed lines: values calculated from equation (7) for  $n = 3$ . (A) Aqueous 0.1 M NaF.  $\tau = 0.51$  sec. (B) Aqueous 0.01 M NaF.  $\tau = 0.41$  sec.





## SUMMARY.

A central motivation for measurement of dynamic surface tension was to provide an experimental test for the conventional hypothesis that an electrified interphase could be considered to have achieved statistical equilibrium once diffusion-migration equilibrium was established. By time-resolved and concomitant measurement of the applied potential, the charge density and the surface tension it was possible to show that for the very simple NaF system the hypothesis was not valid. In fact, relaxation processes appear to be on-going over time periods that are an order of magnitude larger than those necessary for establishment of a diffusion-migration equilibrium for ionic species. Thus, techniques for studying the dynamical response of the electrified interphase by monitoring the time-resolved behavior of the charge density or electrostatic potential are missing essential elements of the dynamical response. The extension of the Wilhelmy technique to the electrified interphase and the use of chronotensiometry as a tool for investigations of the dynamical response of the electrified interphase seeks to remedy this lack of access to crucial information.

The relaxation function surface for chronotensiometric experiments that step the potential from -1.000 V displayed two curious features in the non-equilibrium electrocapillary curves; i) the appearance of two electrocapillary maxima at times prior to the establishment of a diffusion-migration equilibrium and ii) a shift in the ECM potential with time after the establishment of a diffusion-migration equilibrium. This latter feature was predicted by

Defay and Sanfeld using a non-equilibrium thermodynamic analysis, but their prediction that the dynamical behavior of the ECM potential was related to the chronotensiometric response of the surface tension was not borne out by the experiments performed here. Nevertheless, the prediction of the observed shift in the ECM potential with time demonstrates the utility of non-equilibrium thermodynamics for analysis of the dynamical response of electrified interphases.

A very simple kinetic model based on adsorption predicted the observed dynamic surface tension response for two different bulk concentrations of supporting electrolyte. However, because the response of macroscopic observables such as surface tension is underdetermined, ancillary information about the molecular processes involved would be necessary to distinguish this model from a large number of other physical processes that could give rise to relations similar to equation (7).

The Wilhelmy technique for measurement of equilibrium and dynamic surface tension was shown to be a sensitive and reliable technique that can afford experimental access to information about the properties of electrified interphases that cannot be obtained using conventional electrochemical techniques. Whether this information is useful for or relevant to electrochemical processes remains, of course, to be seen.

## BIBLIOGRAPHY

1. a. Mohilner, D.M. in *Electroanalytical Chemistry*, volume 1; A.J. Bard, ed.; Marcel:Dekker, 1966.  
b. Parsons, R. in *Modern Aspects of Electrochemistry*, volume 1; J.O'M. Bockris, ed.; Butterworth:London, 1954.  
c. Delahay, P. *Double Layer and Electrode Kinetics*; Wiley-Interscience:N.Y., 1965, chap. 2.  
d. Conway, B.E. *Theory and Principles of Electrode Processes*; Ronald:N.Y., 1965, chap. 4 and 5.  
e. Bard, A.J.; Faulkner, L.R. *Electrochemical Methods*; J. Wiley and Sons:N.Y., 1980, chap. 12.  
f. Grahame, D.C. *Chem. Rev.* 1947, 41, 441.  
g. Grahame, D.C. *Ann. Rev. Phys. Chem.* 1955, 6, 337.
2. Wilhelmy, L. *Ann. Physik.* 1863, 119, 177.
3. Gaines, G.L. *Insoluble Monolayers at the Liquid-Gas*; Wiley-Interscience:N.Y., 1966.
4. a. Smith, T. *Adv. Coll. Interfac. Sci.* 1972, 3, 161.  
b. Smith, T. *J. Coll. Interfac. Sci.* 1968, 26, 509.  
c. Smith, T. *J. Opt. Soc. Am.* 1967, 57, 1207.
5. Lawrence, J.; Mohilner, D.M. *J. Electrochem. Soc.* 1971, 118, 259.
6. a. Mann, J.A. Jr. in *Techniques of Surface Chemistry and Physics*, volume 1; R.J. Good, et.al., eds.; Marcel Dekker:N.Y., 1972.  
b. Boonman, A.; Gieles, P.; Massen, C.H.; Egberts, J. *Thermochim. Acta* 1986, 103, 107.  
c. van dem Tempel, M.; Lucassen-Reynders, E.H. *Adv. Colloid Interfac. Sci.* 1983, 18, 281.
7. a. Sanfeld, A.; Steinchen, A.; Defay, R. *J. Phys. Chem.* 1969, 73, 4047.  
b. Sanfeld, A. *Introduction to the Thermodynamics of Charged and Polarized Layers*; J. Wiley and Sons:N.Y., 1968, chap. 14.  
c. Prigogine, I.; Mazur, P. *Physica* 1951, 17, 661.
8. a. Rowlinson, J.S.; Widom, B. *Molecular Theory of Capillarity*; J.E. Baldwin, ed.; Clarendon:Oxford, 1982.  
b. Defay, R.; Prigogine, I.; Sanfeld, A. *J. Coll. Interfac. Sci.* 1977, 58, 498.

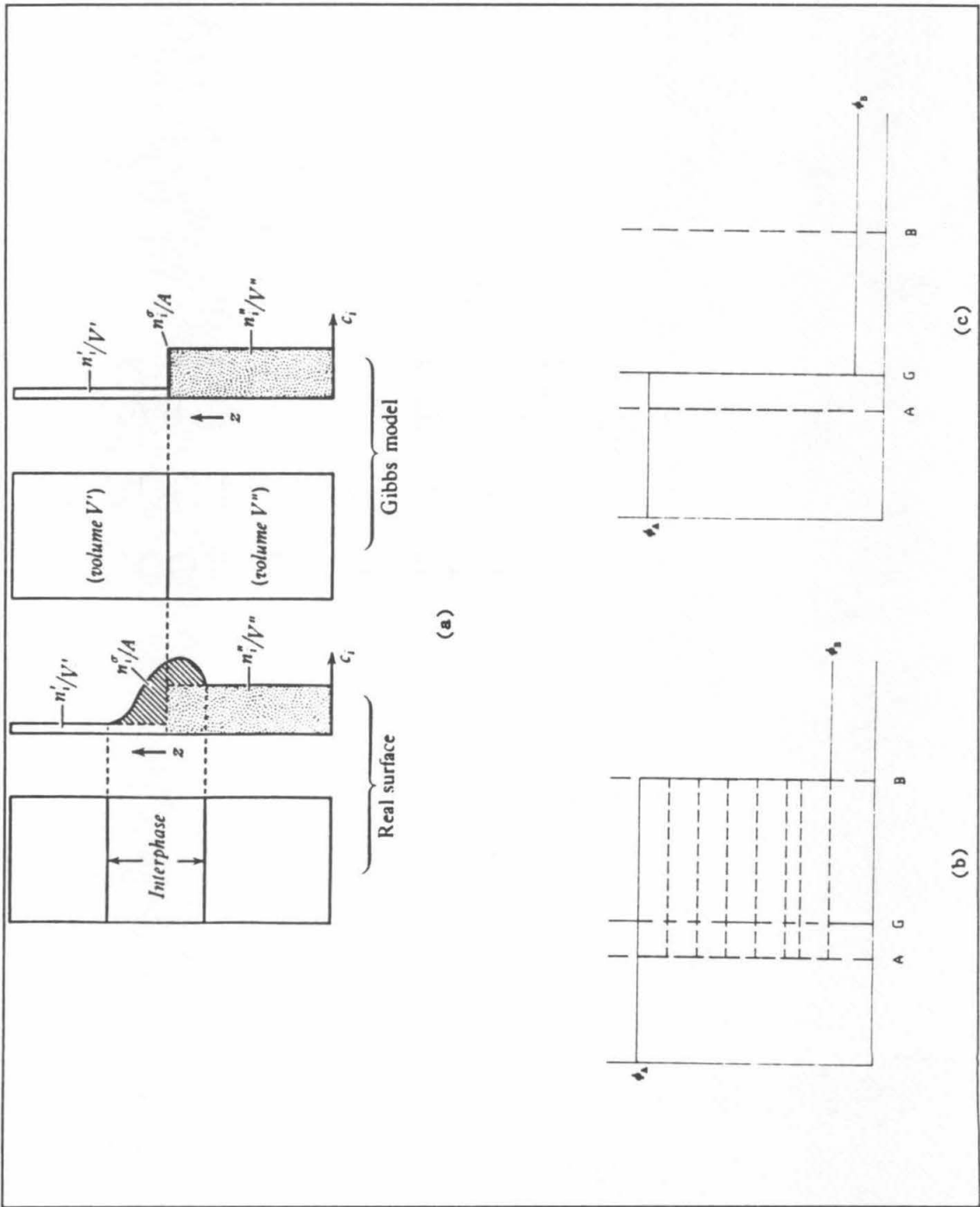
9. a. Kubo, R.; Toda, M.; Hashitsume, N. *Statistical Physics II. Nonequilibrium Statistical Mechanics.*; M. Cardona, ed.; Springer-Verlag:Berlin, 1983.  
b. Yourgrau, W.; van der Merwe, A.; Raw, G. *Treatise on Irreversible and Statistical Thermophysics. An Introduction to Nonclassical Thermodynamics.*; Dover:N.Y., 1982.  
c. Grandy, W.T., Jr. *Foundations of Statistical Mechanics. Volume II: Nonequilibrium Phenomena.*; A. van der Merwe, ed.; Reidel:Dordrecht, 1987.
10. a. Sanfeld, A.; Defay, R. *J. Phys. Chem.* 1969, 73, 4047.  
b. Defay, R.; Sanfeld, A. *Electrochim. Acta* 1967, 12, 913.
11. a. Kuwabara, R.; Iwaki, T.; Morimoto, T. *Langmuir* 1987, 3, 1159.  
b. Suda, Y.; Morimoto, T. *Langmuir* 1987, 3, 786.  
c. Iwaki, T.; Morimoto, T. *Langmuir* 1987, 3, 287.

**APPENDIX I**

## APPENDIX I

Use of an electrostatic potential,  $\phi$ , as an intensive variable of state for electrochemical systems is convenient because operational control of  $\phi$  is facile. Thus, the practice of defining an equation of state for an electrochemical interphase of planar geometry as some  $f(T, \rho_i, A, \phi)$ , where  $T$  is the thermodynamic temperature,  $\rho_i$  the density of species  $i$ ,  $A$  the surface area of the interphase and  $\phi$  an electrostatic potential, is common to the contemporary literature of electrochemistry.<sup>1</sup> Figure 1 sketches a simple demonstration of the problems that attend equations of state of the form  $f(T, \rho_i, A, \phi)$  for electrified interphases. Figure 1a displays the classic Gibbs dividing-surface model<sup>2</sup> applied to an electrified interphase where a three dimensional "real" interphase described in this case by some  $f(T, \rho_i, A, \phi)$  is mapped onto a two-dimensional "reference" surface described by some  $f(T, \rho_i, A, ?)$ . The origin of the question mark argument is clear from examination of Figures 1b and 1c that display the behavior of  $\phi$  along the axis normal to the interphase of figure 1a. Figure 1b displays a series of possible  $\phi$  profiles at the real interphase. Because  $\nabla X = 0$  is required of all intensive state variables within a phase,  $\phi$  can only change at the two boundaries between the interphase and the bulk phases (*i.e.* points A or B). Thermodynamics does not provide a prescription for changing  $\phi_A$  to  $\phi_B$  across the interphase and thus any value of  $\phi_A \geq \phi_\alpha \geq \phi_B$  can be chosen for the interphase. Mapping Figure 1b onto any arbitrary Gibbs dividing-surface does not solve this problem as illustrated in Figure 1c. Again,  $\phi_\alpha$  can assume any value between  $\phi_A$  and  $\phi_B$ . Variables that

Figure 1. (A) Conventional Gibbs Model of an interphase. (B) Electrostatic potential profile across the "real" interphase of (A). Solid line:  $\phi_{AB}$ , the "inner" electrostatic potential. Dashed lines: other choices for  $\phi$ . Broken line: Gibbs dividing-surface denoted G. (C) Mapping of (B) onto a Gibbs dividing surface at G.



can assume arbitrary values are not well-suited to the task of defining the state of a system.

There is a further problem with both the choice of  $\phi_\alpha$  as a state variable and the Gibbs dividing-surface model. Because changes in the potential in Figures 1b and 1c are step-functions, the electric field (i.e.  $\nabla\phi$ ) at the interphase assumes values of infinity. Electric fields within a thermodynamic system contribute to the total internal energy of the system and infinite electric fields contribute infinitely. An infinite electric field would generate a system with infinite energy - known more commonly as a perpetual motion machine - and any model that predicts this phenomena clearly is incorrect.

BIBLIOGRAPHY

1. a. Grahame, D.C. *Chem. Rev.* 1947, 41, 441.
  - b. P. Delahay *Double Layer and Electrode Kinetics*; Wiley:N.Y., 1980, chapter 2.
  - c. Mohilner, D.M. *Electroanal. Chem.* 1966, 1, 241.
  - d. A.J. Bard and L.R. Faulkner *Electrochemical Methods: Fundamentals and Applications*; Wiley:N.Y., 1980, chapter 12.
2. J.W. Gibbs *Collected Works*; Volume 1, Longmans:N.Y., 1928, 219.

**APPENDIX II**

## APPENDIX II

## The Inertial Limit for the Response Function of a Wilhelmy Plate

At equilibrium, the force exerted by surface tension to support a meniscus is equal and opposite to the force resulting from acceleration of meniscus mass by the gravity potential, i.e.;

$$\gamma\xi = F_\gamma = -F_g = -mg \quad (1)$$

Where  $\xi$  is the total perimeter length of the Wilhelmy Plate.

Evaluation of the inertial limit requires an equation of motion for a meniscus responding to a step function in the surface tension, e.g.;

$$F_\gamma(t) = -m_i g \quad t < t_s$$

$$F_\gamma(t) = -m_f g \quad t > t_s$$

The net force on a meniscus,  $F_{net}(t)$ , at any time  $t > t_s$  is just,

$$\begin{aligned} F_{net} &= -m_f g - m(t)g \\ &= -[m_f + m(t)]g \end{aligned}$$

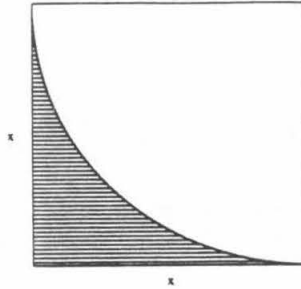
where  $m(t)$  is the mass of the meniscus at  $t > t_s$ .

The inertial limit is the total time,  $\Delta t$ , required to re-establish mechanical equilibrium by moving the height of the meniscus a distance  $\Delta x$ . This time depends only on the acceleration,  $g$ , and  $\Delta x$ . These quantities are related by a simple difference equation,

$$\Delta t^2 = 2\Delta x g^{-1} \quad (2)$$

Evaluation of equation (2) for any given  $\Delta\gamma$  requires an expression relating surface tension to the height of the meniscus.

Meniscus volume can be derived by considering the following diagram;



The cross-sectional area of a meniscus is  $x^2(1 - \pi/4)$  and the total volume,  $V = x^2(1 - \pi/4)\xi$ . The mass of a meniscus can be written in terms of  $x$  by introducing  $\rho = m/V$ ,

$$m = x^2 \xi \rho (1 - \pi/4)$$

From equation (1),

$$\gamma \xi = -mg = -x^2 \xi \rho (1 - \pi/4)g$$

$$\gamma = -x^2 \rho g (1 - \pi/4)$$

$$x = -\gamma^{1/2} [\rho g (1 - \pi/4)]^{-1/2} \quad (3)$$

Writing equation (3) as a difference equation and substituting for  $\Delta x$  in equation (2) gives the desired result,

$$\Delta t = (2\Delta\gamma^{1/2} g^{-3/2} [\rho(1 - \pi/4)]^{-1/2})^{1/2}$$

which for mercury ( $\rho = 13.6 \text{ g/cm}^3$ ) is,

$$\Delta t = (0.0000382 \Delta\gamma^{1/2})^{1/2}$$

Hence, the maximum value for  $\Delta t$  would correspond to a step from the ECM to a hypothetical potential where  $\gamma = 0$ . The time required to re-establish mechanical equilibrium for a  $\gamma$  step of this size is ca. 28

milliseconds. Response times for step sizes of experimental interest (e.g.  $\Delta\gamma \sim 25$  dyne/cm) are on the order of 10-15 milliseconds.

Because experimental relaxation times are at least two orders of magnitude larger than this, it is unlikely that inertial limits to the response function are an important factor in the observed response.

**APPENDIX III**

II-110

OPERATION GUIDE FOR MEASURING STATIC AND DYNAMIC SURFACE  
TENSION USING THE WILHELMY PLATE TECHNIQUE.

IN PARTIAL FULFILLMENT OF THE REQUIREMENTS  
FOR THE DEGREE OF  
DOCTOR OF PHILOSOPHY

DON MONTGOMERY  
FEBRUARY 1990

## Hardware

### 1.0 Vibration Isolation

#### ·1.0.1 Leveling

Vibration isolation is achieved by suspending the inert atmosphere chamber from three elastomer fiber cords (i.e. *bungi* cords) which are attached to a wooden tripod frame via three turnbuckles. To level the chamber, place a circular bubble level inside the chamber at the center and rotate the turnbuckles to move the cords up or down. The chamber should be configured as it will be during an experiment with the mercury filled electrochemical cell in place so that mass is distributed correctly and the apparatus will not have to be relevelled during an experiment. The turnbuckles will not, in general, allow for perfect leveling of the instrument and it is often necessary to add small weights to the bottom shelf of the chamber for fine adjustment of the level.

#### ·1.0.2 Mass Damping

The heavier the instrument is, the better the vibration isolation - especially at critical low frequencies. Fully configured the instrument weighs about 100 kg and this seems to be enough mass to afford good low frequency vibration isolation. If more mass is necessary just add lead weights to the bottom shelf of the chamber and relevel the instrument.

### 1.1 Inert Atmosphere Chamber

#### ·1.1.1 Seals

All flanges on the inert atmosphere chamber are sealed with PTFE o-rings. Because the chamber was constructed from salvaged parts, flange seals are both the ultra-high vacuum knife edge type and o-ring grooves. The ports with o-ring grooves will accommodate o-rings with a circular cross section. The knife edge ports require o-rings with a square cross section that are designed to be an alternative to the copper rings which are usually employed with knife edge flanges.

With the exception of the two main flanges (top and bottom), all of the o-rings on the instrument have standard sizes and should be in stock at any o-ring vendor. The o-rings with square cross sections can be obtained from vendors specializing in vacuum systems. The two main o-rings for the top and bottom flanges are approximately 55 cm in diameter and require a special order that will take eight to ten weeks.

O-rings will degrade fairly quickly if exposed to the ambient atmosphere in a chemical laboratory. They are best kept by storing them next to the frozen dinners in your freezer at home.

### **-1.1.2 Electrical Feedthroughs**

There are two electrical feedthroughs on the instrument. One is attached to the stainless steel cap that covers the end flange on the glass electrobalance case and the other is attached to the side of the chamber and serves to connect the electrochemical cell to the potentiostat. The use of these feedthroughs is self-explanatory. Care, however, must be taken to ensure that the perforated teflon and ceramic discs which separate the feedthrough leads are in place and that there are no shorts due to leads touching against one another.

### **-1.1.3 Spills**

Although the inert atmosphere chamber is fabricated from 304 stainless steel, it will rust very quickly if exposed to aqueous electrolyte solutions. If a spill occurs inside the chamber, immediately aspirate as much of the solution away as is possible. The chamber should then be wiped out thoroughly with kimwipes attached to a long appliance. Usually, the chamber will have to be recleaned after a major spill and any rust that forms scoured out with steel wool or an abrasive - a big hassle - so do not spill anything.

## **1.2 Electrobalance**

### **-1.2.1 Control Unit**

The output from the electrobalance is a voltage signal that is proportional to the force that the torque motor must apply to keep the balance beam level. Although the electronics

that drive the torque motor are on the electrobalance, the electronic tare adjustments, balance range control and voltage output for interfacing with a hardcopy device or with a computer A/D board is provided remotely via a control unit.

The control unit should be left on at all times because it requires at least 24 hours for the electronics to warm up. The Wilhelmy plate is suspended from the B hangdown loop (the one closest to the torque motor) and the control unit recorder range should be set on B as well. When the electrobalance is not in use, the output switch on the control unit should be set to SHORT. This will short the output jacks on the rear panel together and to the instrument ground. When measuring surface tension or adding tare weights, set the switch to OUTPUT.

#### **·1.2.2 Interfacing with the Computer**

There are two sets of output jacks on the back of the control unit that give a full span output of 0-1 mV and 0-10 mV. Use the 0-10 mV jack for the output signal that is sent into the A/D board. The output impedance of this jack is 900 ohms. The mass range that corresponds to this voltage signal is set by the RECORDER RANGE buttons on the front panel of the control unit. The output voltage signal varies in a linear fashion with changes in mass.

The output from the 0-10 mV jack should be sent through a BNC cable to an input channel on the A/D board. The input channel can be configured for either pseudo-differential or full-differential input. The signal should be split at the BNC connector where it enters the A/D board and sent to a digital voltmeter as well. Be sure that the total output impedance that the signal encounters is around 900 ohms.

#### **·1.2.3 Hangdowns**

The manufacturer provides 0.10 mm diameter nichrome wire for suspending balance pans and so forth from the electrobalance. However, the one meter length of nichrome wire used to hang the Wilhelmy plate from the electrobalance is nearly impossible to keep

straight and kink-free. A 5.5 mm diameter copper wire serves as an adequate substitute and has the advantage of being easy to work. The copper wire will amalgamate with any gas phase mercury that is present inside the chamber and its mass may change slowly over time. This should not be a problem if the wire is removed when not in use and mercury is not allowed to stand for long periods inside the chamber. The Wilhelmy plate should be hung from the B hangdown loop of the balance because this allows up to 3.5 grams of mass and is more robust. The higher accuracy of the A hangdown loop is not necessary and use of the A hangdown loop makes the experiment more susceptible to background noise.

Tare weights should be placed in the balance pan prior to any experiment because the serious mechanical disturbances that invariably accompany changing tare weights are not acceptable during an experiment. The Wilhelmy plate should be suspended in an aqueous solution during preplacement of tare weights to accurately adjust for the buoyancy of the kel-F jacket in water. The threaded rod assembly that moves the electrobalance up and down should be placed as near as possible to the middle of its range. This ensures the maximum possible travel for adjustment during an experiment. After preplacement of the tare weights, replace the glass hang-down cover and clamp it into place.

#### **1.2.4 Cleaning the Balance**

There are two ceramic stops that limit the travel of the balance beam and help prevent mechanical damage to the balance. These stops are somewhat porous and will adsorb mercury vapor that is present in the ambient atmosphere. This is a problem because the arms of the balance beam are plated with gold and will stick to the stops if there is sufficient adsorbed mercury in the stops. If this happens, it is not possible to do experiments and the electrobalance must be disassembled and the stops cleaned.

To gain access to the stops, remove the protective metal cowling that covers the electrobalance and turn the unit upside down. Be very careful not to bend any of the

hangdown wires, metal flags and especially the balance beam. Once the electrobalance is positioned for cleaning, apply a very dilute solution of nitric acid to one of the ceramic stops using a q-tip and then wipe it off with distilled water. Do not get any nitric acid solution on the gold-plated balance beam or you will have to return the unit to the manufacturer for an expensive repair and replating job. Repeat this procedure until the dull gray color on the ceramic stop disappears. Once this has been accomplished wipe the stop repeatedly with distilled water using a fresh q-tip each time. Finish by swabbing the stop with methanol and then trichloroethane to remove any organic residue left by the cleaning process. Repeat the procedure with the other stop (clean only one stop at a time), check the balance to be sure it is no longer sticking and then replace the cowling. The frequency with which this must be done depends on how frequently experiments are performed, but count on doing it at least once a year.

### **1.3 Computer**

#### **1.3.1 Analog-to-Digital Boards**

There are two Analog Devices RTI 800 series real-time interface I/O boards in the computer (RTI-802 and RTI-815) that provide a variety of data acquisition, analog output, digital I/O and counter-timer functions. Both the RTI-802 and RTI-815 boards provide 12-bit analog input or output channels with software selectable gain. The RTI-802 board has four analog output channels with jumper-selectable voltage output ranges of 0-10 V or  $\pm 10$  V at 2 mA. The RTI-815 board has 16 single-ended, 16 pseudo-differential or 8 full-differential input channels and two analog output channels with jumper-selectable voltage output ranges of 0-10 V or  $\pm 10$  V at 2 mA. The RTI-815 board provides one 8-bit digital input port and one 8-bit digital output port, both of which are TTL compatible. Time related digital I/O is also provided by the RTI-815 board which has three TTL compatible timer/counter channels with a maximum count rate of 100 kHz and one pacer clock channel

for time-based triggering. All of these I/O functions are accessible through BNC terminals attached to two rack mounted panels near the computer.

The RTI-802 board is configured as supplied by the factory and the output voltage range set for  $\pm 10$  V. This board should be used for analog output functions because a high precision reference voltage is generated on-board and distributed across all channels to provide tracking between the analog outputs. The outputs are also protected from accidental grounding. Data coding is selected as two's complement.

The RTI-815 board is configured for pseudo-differential input and a bipolar input range of  $\pm 5$  V. The input mode and voltage range is selected by positioning jumpers on the analog input multiplexer unit. The I/O map address location is 340H. The analog output voltage range is set for  $\pm 10$  V. Data coding is selected as two's complement.

A typical experiment requires three analog input channels for the electrobalance signal and inputs from the potentiostat. Two analog output channels are usually required to trigger and reset the potentiostat.

### **1.3.2 Software**

All of the I/O functions of the A/D boards can be accessed through software running under the PC DOS operating system by calling subroutines from libraries that are provided by the manufacturer. These macros are designed to be called from application programs that are written in Microsoft MACRO assembler, IBM compiled BASIC, IBM interpreted BASICA, Microsoft compiled BASIC, Lattice C, Microsoft PASCAL and Microsoft FORTRAN.

The manufacturer also provides software for constructing a configuration table (ADICONF.COM), loading the configuration table (CLOAD.EXE) and calibrating the A/D boards (RTICAL.COM). The configuration table (CONFIGB.DAT) should be loaded each time the system is booted-up by including the appropriate calls in the DOS CONFIG.SYS batch file. The boards should be calibrated at least once a year.

If you plan to use interpreted BASICA then run the BASLOAD.EXE program to obtain the correct address for use with the DEF SEG statement in your application program. For application programs that are written in other languages compile and then link your program to the appropriate language library. The manufacturer also provides two programs for testing all of the I/O functions of the A/D boards: ADITEST.EXE (source code in ADITEST.C) which is written in Microsoft C and FUNCT.BAS which is written in IBM interpreted BASICA.

The library subroutines that were of particular importance for the experiments that I performed were the following;

INITIALIZE - Initializes global data and the Am9513 timer chip.

AIN - Reads a single value from an input channel.

COLLECT - Read a specified number of samples from a single input channel using DMA (direct memory access) transfers.

SCAN - Does a sequential scan of all input channels under DMA.

CHECK - Checks status of DMA operation and transfers data to the user buffer.

CANCEL - Cancels the current DMA operation.

PULSE - Outputs a single pulse of a specified duration.

DELAY - Delays execution of the code for a specified period.

I wrote software routines in IBM interpreted BASICA, IBM compiled BASIC and Lattice C. There are three programs written in BASICA that you may find of use as guides when you write software for your specific application. SCAN1.BAS is for cyclic voltammetry, SYNC12.BAS is for potential step experiments and PULSE1.BAS is for applying single or multiple voltage pulses. All of these programs obtain data from three channels in a quasi-simultaneous fashion and send out the appropriate trigger pulses to the potentiostat to control the experiment. The data is written to files and displayed graphically on the terminal during an experiment.

### 1.4 Electrochemical Cell

The electrochemical cell is formed from a 9.67 cm diameter crystallization dish that is filled with about 5-6 mm of mercury to form a 73.44 cm<sup>2</sup> mercury pool electrode. Connection to this electrode is made through a platinum wire that is encased within a teflon jacket such that the solution cannot come into contact with the wire during an experiment. This working electrode lead is bent so that it clips over the edge of the crystallization dish and stays in place. The counter electrode is also formed from platinum wire which has been bent such that it forms a circular loop that clips onto the edge of the crystallization dish and extends approximately 1.5 cm down into the dish from the upper rim.

The reference electrode is located on the exterior of the chamber and connection with the cell is made through a 32 cm long glass probe that is sealed at one end by a plug of vicor glass. The vicor glass plug is attached to the the probe by means of heat-shrinkable PTFE tubing. The reference probe assembly is filled with a supporting electrolyte solution and stored with the vicor glass end immersed in a solution of the same supporting electrolyte. These probes are dedicated devices which can only be used for experiments that employ the same supporting electrolyte as used for the solution filling the inside of the probe.

### 1.5 Wilhelmy Plate

The Wilhelmy plate consists of a platinum plate which is approximately 0.13 mm thick by 2.5 cm long by 0.4 cm wide. No part of this plate should be exposed to the supporting electrolyte during an experiment. To ensure that this does not happen a kel-F jacket should be made with a 0.08 mm groove into which the platinum plate can be press fit. Be sure that there is at least 4 mm of platinum exposed after press fitting the plate into the jacket. The press fit should be very tight otherwise gases can form at the platinum plate during electrochemical experiments and get trapped inside the groove. If this happens the buoyancy of the plate will change with time and your experimental mass measurements will

be worthless. Small holes should be drilled at the corners of the kel-F jacket through which a piece of nichrome wire can be threaded to form a strap for hanging the plate. See my thesis for a diagram and more detailed description of the Wilhelmy plate assembly.

Once the Wilhelmy plate assembly has been fabricated, the exposed platinum can be plated with mercury by dipping it into a sodium-mercury amalgam ( 10:1 Hg:Na) until visual inspection indicates that Hg is covering all of the plate up to the lip of the kel-F jacket (about one to two minutes). Sonicate the Wilhelmy plate for about 30 minutes in a beaker of methanol to remove any sodium that remains in the mercury. Then sonicate the plate in a beaker of trichloroethane for about an hour and then again in fresh trichloroethane for about 15 minutes to ensure that the assembly is clean.

The Wilhelmy plate assembly should be stored by suspending it above a small pool of mercury such that the mercury plated portion is dipped into the pool and a meniscus of mercury adheres to the plate. The storage container should be configured such that exposure to ambient air is minimized. This will make cleaning the plate for use in an experiment a more facile task.

## **Experimental**

### **3.0 Pretreatment, Assembly and Cleaning of the Inert Atmosphere Chamber**

There are two classes of impurities that are cause for concern when measuring surface tension at electrified mercury interphases. One is oxygen and the other is organic impurities and dust. Oxygen can be managed by scrubbing the gas stream. However, the scrubbing process generates dust in the gas stream and lubricants used when the argon tanks are filled will yield organic impurities that are not removed by the oxygen scrubbing process. The dust problem can be managed effectively by including a 0.5 micron filter in the gas line. The trace organic problem can be solved by including an activated charcoal filter (I used a product manufactured by Scientific Glass Engineering). Clearly, the dust filter should be the last gas stream treatment stage before argon enters the chamber.

All bolts that are used to put together flange assemblies should be tightened in a symmetric fashion so that the o-rings are compressed uniformly. If this is not done the chamber will leak. Do not use Lock-tite on the bolts. If they are tightened properly, they will not loosen over time because the compressed o-ring acts as a spring.

The inert atmosphere chamber itself should be cleaned thoroughly with trichloroethane prior to final assembly. This means swabbing out the chamber with a lint-free cloth several times and removing any residual dust that is seen using vacuum aspiration. All of the small parts that are added to the chamber (e.g. flanges, feedthroughs and so forth) should be sonicated in trichloroethane if they will fit. Use gloves and pay attention to where you place and store recently cleaned parts prior to assembly. As a final cleaning step pour a quantity of trichloroethane into the chamber and swirl it around. Then invert the chamber over a 55 gallon drum and allow it to drain (eyebolts should be placed in a triangular pattern around the perimeter of the drum to support the chamber as it drains). Repeat this procedure several times and then seal the chamber after the trichloroethane has evaporated.

After the chamber has been sealed, add the remaining accessories (including the glass electrobalance vessel). The bunji cords should be attached to the upper flange of chamber, otherwise the instrument is unstable and impossible to level. The assembled instrument should be supported on lab jacks at all times, except during experiments, electrobalance adjustments and leveling. This prevents the cords from stretching and losing their elasticity over time.

The PTFE o-rings will adsorb oxygen when exposed to ambient air and this oxygen will leach out of the o-rings slowly during an experiment. Thus, the chamber should be flushed with argon for about 24 hours prior to an electrochemical experiment. This will ensure that the PTFE o-rings are saturated with argon. Maintain a vigorous flow of argon through the chamber during experiments. This will result in a high argon content in the air that you breathe while you are performing an experiment. Saturating your blood with argon

is not a good thing so be sure that the room in which you perform the experiments is well ventilated.

### **3.1 Pretreatment of Electrochemical Cell**

The crystallization dish and platinum wires should be cleaned by sonication in trichloroethane for about 30 minutes. Assemble the electrochemical cell and place it into the chamber. (It is important to note that you should wear gloves at all times when handling the electrochemical cell and inserting your hands into the chamber.) There should be a larger crystallization dish prepositioned inside the inert atmosphere chamber into which the electrochemical cell is placed. This larger dish will act as a spill guard to prevent electrolyte from coming into contact with the stainless steel body of the chamber. Connect the electrical leads to the electrochemical cell and reseal the chamber. Add mercury to the cell by pouring it down a long, precleaned stainless steel tube into the dish. After adding the mercury pool, aspirate the top layers of contaminated mercury away using a long stainless steel appliance which is connected to a vacuum pump.

At this point the Wilhelmy plate should be brought down onto the mercury surface (see section 3.2) and the reference electrode probe positioned close to the electrode surface near the Wilhelmy plate. Deaerated supporting electrolyte should then be added via a pipette such that it completely covers the top of the Wilhelmy plate. Connect the electrochemical cell to a potentiostat and then apply a constant potential to the cell that is negative enough to reduce oxygen. Re-adjust the Wilhelmy plate and continue to hold the applied potential constant until the background current has vanished (this usually takes about 12-24 hours). At this point the instrument is ready for experiments.

### **3.2 Placement of the Wilhelmy Plate**

The Wilhelmy plate should be placed into the inert atmosphere chamber after the electrochemical cell is in place, but before the mercury or reference electrode probe is added. The vertical position of the plate should be about right because it has been preset

during the addition of tare weights. Add the mercury up to a level that is above the bottom edge of the plate and aspirate the contaminated surface layers off of the mercury pool electrode (taking care not to aspirate the plate or hangdown hardware). Adjust the vertical position of the plate by raising and lowering the glass electrobalance case using the threaded brass rod and nut assembly. This is best accomplished by raising the bottom edge of the plate above the surface level of the mercury, but not so far that the meniscus breaks and the plate disengages itself from the surface. Slowly lower the plate until the voltmeter that is monitoring the electrobalance output indicates that the plate is losing mass. This will occur because the buoyant force of the mercury displaced by the plate will act against gravity (i.e. the plate will float) and the effective force the electrobalance torque motor must apply to maintain a level balance beam will decrease. At this point you should adjust the position of the plate and the coarse zero adjustment on the balance electronics such that the mass registered by the voltmeter is approximately what you expect and that the amount of electronic tare that is added is minimized. In general, positioning the plate, adjusting the level of the mercury pool electrode and adding electronic tare will take quite a bit of fiddling about (this process improves with experience).

After the plate position has been established, add the reference electrode probe and the supporting electrolyte. Potentiostat the cell at a potential near the electrocapillary maximum and repeat the above adjustment procedure. You will probably have to readjust one more time after the background current has fallen to zero.

### 3.3 Clean-up

The procedures for cleaning up after an experiment should be self-evident - especially if you have read this manual. I would like to emphasize some points of interest at the risk of appearing to patronize (this is an annoying habit one slips into after years of dealing with useless third world minions).

The order that I remove things from the chamber is as follows: (i) the Wilhelmy plate so that during subsequent steps you do not inadvertently damage the electrobalance, (ii) the electrochemical cell (pay attention while you do this - the thing is full of spillable supporting electrolyte) and (iii) remove the hangdown wire that supports the plate and reseal the chamber. Be sure that the chamber is supported by lab jacks while you are doing this.

After the chamber has been cleaned up let argon flow through the system for several hours to be sure that any condensed moisture that could rust the chamber has evaporated. If you plan on doing another experiment in the immediate future, then maintain a slow flow of argon through the chamber. If not then shut off the argon flow and be aware that you will have to resaturate the o-rings with argon before you do another experiment.

## SCAN1.BAS

```

10 F$="#.#####^"
20 INPUT "FILE NUMBER"; NUM$
30 FILE$ = NUM$ + ".DAT"
40 FILEA$ = NUM$ + ".ASC"
50 TFILE$ = "T" + FILE$
60 CFILE$ = "C" + FILE$
70 VFILE$ = "V" + FILE$
80 OPEN TFILE$ FOR OUTPUT AS #1
90 OPEN CFILE$ FOR OUTPUT AS #2
100 OPEN VFILE$ FOR OUTPUT AS #3
110 DEFINT A-Z
120 DEF SEG = &HEC7
130 INITIALIZE=0
140 AIN=18
150 PULSE=57
160 CALL INITIALIZE(XER)
170 BOARD=2
180 CHAN=0
190 CHAN1=1
200 CHAN2=2
210 CHAN3=3
220 CHAN5=5
230 RANGE=10000
240 PERIOD=100
250 GAIN=10
260 GAIN1=1
270 GAIN2=10
280 INPUT "FILTER ITERATIONS"; I
290 KEY 15, CHR$(&H40) + CHR$(&H1C)
300 ON KEY(15) GOSUB 690
310 KEY(15) ON
320 KEY 17, CHR$(&H40) + CHR$(&H39)
330 ON KEY(17) GOSUB 960
340 KEY(17) ON
350 SCREEN 2
360 PSET (25,180)
370 DRAW "U180"
380 FOR A=1 TO 3
390 FOR B=1 TO 12
400 DRAW "R5 BL5 D5"
410 NEXT B
420 DRAW "R576"
430 FOR C=1 TO 24
440 DRAW "U2 BD2 L24"
450 NEXT C
460 NEXT A
470 CALL PULSE (BOARD, CHAN2, RANGE, PERIOD, XER)
480 FOR S=1 TO I
490 CALL AIN (BOARD, CHAN3, GAIN1, VALL1, XER)
500 VAL1! = VALUE! + VALL1
510 VALUE! = VAL1!
520 NEXT S
530 VALL1 = VAL1!/I
540 VALUE! = 0
550 CALL AIN (BOARD, CHAN, GAIN, VALL, XER)
560 CALL AIN (BOARD, CHAN5, GAIN2, VALL2, XER)
570 Y=VALL*(57/4096)+2
580 Y1=VALL1*(57/4096)+62
590 Y2=VALL2*(57/4096)+122
600 PSET (X+35, Y)

```

```

610 PSET (X+35,Y1)
620 PSET (X+35,Y2)
630 WRITE #1,X,VALL
640 WRITE #2,X,VALL1
650 WRITE #3,X,VALL2
660 X=X+.5
670 IFLEN = IFLEN + 1
680 GOTO 480
690 SCREEN 0
700 CALL PULSE (BOARD,CHAN1,RANGE,PERIOD,XER)
710 CLOSE #1,#2,#3
720 FOR S = 1 TO 3
730 READ L$
740 IFILE$ = L$ + FILE$
750 OFILE$ = L$ + FILEA$
760 BFILE$ = "F:" + OFILE$
770 OPEN IFILE$ FOR INPUT AS #2
780 OPEN BFILE$ FOR OUTPUT AS #1
790 PRINT #1,"**"
800 ABSMIN =0!
810 ABSINC =1!
820 IFTYPE = 1
830 PRINT #1,USING "\          \ ";OFILE$;
840 PRINT #1,USING "\          \ ";OFILE$
850 PRINT #1,USING "# ";IFTYPE;
860 PRINT #1,USING "#### ";IFLEN;
870 PRINT #1,USING "#.#####^ ^ ^ ^ ";ABSMIN;ABSINC
880 FOR I= 1 TO IFLEN
890 INPUT #2,X,Y
900 PRINT #1, USING F$; Y
910 NEXT I
920 CLOSE #1,#2
930 DATA T,C,V
940 NEXT S
950 END
960 CALL PULSE (BOARD,CHAN1,RANGE,PERIOD,XER)
970 GOTO 950

```

```

10 F$="#.#####^"
20 INPUT "INITIAL FILE NUMBER"; NUM
30 INPUT "NUMBER OF RUNS";N
40 N1=0
50 NUM$ = STR$(NUM)
60 FILE$ = NUM$ + ".DAT"
70 FILEA$ = NUM$ + ".ASC"
80 TFILE$ = "T" + FILE$
90 CFILE$ = "C" + FILE$
100 VFILE$ = "V" + FILE$
110 OPEN TFILE$ FOR OUTPUT AS #1
120 OPEN CFILE$ FOR OUTPUT AS #2
130 OPEN VFILE$ FOR OUTPUT AS #3
140 DEFINT A-Z
150 DEF SEG = &HEC7
160 FLAG = 0
170 INITIALIZE=0
180 AIN=18
190 PULSE=57
200 DELAY=63
210 CALL INITIALIZE(XER)
220 BOARD=2
230 CHAN=0
240 CHAN1=3
250 CHAN2=5
260 CHAN3=1
270 RANGE=10000
280 PERIOD=10
290 GAIN=100
300 GAIN1=1
310 GAIN2=10
320 KEY 15, CHR$(&H40) + CHR$(&H1C)
330 ON KEY(15) GOSUB 1020
340 INPUT "INDUCTION PERIOD";IND
350 KEY(15) ON
360 SCREEN 2
370 PSET (25,180)
380 DRAW "U180"
390 FOR A=1 TO 3
400 FOR B=1 TO 12
410 DRAW "R5 BL5 D5"
420 NEXT B
430 DRAW "R576"
440 FOR C=1 TO 24
450 DRAW "U2 BD2 L24"
460 NEXT C
470 NEXT A
480 T0! = TIMER
490 CALL AIN (BOARD,CHAN1,GAIN1,VALL1,XER)
500 CALL AIN (BOARD,CHAN,GAIN,VALL,XER)
510 CALL AIN (BOARD,CHAN2,GAIN2,VALL2,XER)
520 Y=VALL*(57/4096)+2
530 Y1=VALL1*(57/4096)+62
540 Y2=VALL2*(57/4096)+122
550 T1! = TIMER
560 PSET (X+35,Y)
570 PSET (X+35,Y1)
580 PSET (X+35,Y2)
590 WRITE #1,X,VALL
600 WRITE #2,X,VALL1

```

```

610 WRITE #3,X,VALL2
620 IF INT(T1!-T0!) = 25 THEN GOTO 680
630 IF FLAG = 1 THEN GOTO 650
640 IF INT(T1!-T0!) = IND THEN GOSUB 990
650 X=X+.5
660 IFLEN = IFLEN + 1
670 GOTO 490
680 SCREEN 0
690 CLOSE #1,#2,#3
700 CALL PULSE (BOARD,CHAN3,RANGE,PERIOD,XER)
710 FOR S = 1 TO 3
720 READ L$
730 IFILE$ = L$ + FILE$
740 OFILE$ = L$ + FILEA$
750 BFILE$ = "F:" + OFILE$
760 OPEN IFILE$ FOR INPUT AS #2
770 OPEN BFILE$ FOR OUTPUT AS #1
780 PRINT #1,"**"
790 ABSMIN =0!
800 ABSINC =-1!
810 IFTYPE = 1
820 PRINT #1,USING "\          \ ";OFILE$;
830 PRINT #1,USING "\                                     \";OFILE$
840 PRINT #1,USING "# ";IFTYPE;
850 PRINT #1,USING "#### ";IFLEN;
860 PRINT #1,USING "#.#####^ ^ ^ ^ ";ABSMIN;ABSINC
870 FOR I= 1 TO IFLEN
880 INPUT #2,X,Y
890 PRINT #1, USING F$; Y
900 NEXT I
910 CLOSE #1,#2
920 DATA T,C,V
930 NEXT S
940 NUM = NUM + 1
950 N1 = N1 + 1
960 IF N1 = N THEN GOTO 980
970 GOTO 50
980 END
990 CALL PULSE (BOARD,CHAN,RANGE,PERIOD,XER)
1000 FLAG = 1
1010 RETURN
1020 CALL PULSE(BOARD,CHAN3,RANGE,PERIOD,XER)
1030 GOTO 980

```

## PULSE1.BAS

```

10 F$="#.#####^^^"
20 INPUT "FILE NUMBER"; NUM$
30 FILE$ = NUM$ + ".DAT"
40 FILEA$ = NUM$ + ".ASC"
50 TFILE$ = "T" + FILE$
60 CFILE$ = "C" + FILE$
70 VFILE$ = "V" + FILE$
80 OPEN TFILE$ FOR OUTPUT AS #1
90 OPEN CFILE$ FOR OUTPUT AS #2
100 OPEN VFILE$ FOR OUTPUT AS #3
110 DEFINT A-Z
120 DEF SEG = &HEC7
130 FLAG = 0
140 INITIALIZE=0
150 AIN=18
160 PULSE=57
170 DELAY=63
180 CALL INITIALIZE(XER)
190 BOARD=2
200 CHAN=0
210 CHAN1=1
220 CHAN2=2
230 CHAN3=3
240 CHAN5=5
250 RANGE=10000
260 PERIOD=10
270 GAIN=100
280 GAIN1=1
290 GAIN2=10
300 KEY 15, CHR$(&H40) + CHR$(&H1C)
310 ON KEY(15) GOSUB 960
320 INPUT "INDUCTION PERIOD";IND
330 KEY(15) ON
340 SCREEN 2
350 PSET (25,180)
360 DRAW "U180"
370 FOR A=1 TO 3
380 FOR B=1 TO 12
390 DRAW "R5 BL5 D5"
400 NEXT B
410 DRAW "R576"
420 FOR C=1 TO 24
430 DRAW "U2 BD2 L24"
440 NEXT C
450 NEXT A
460 T0! = TIMER
470 CALL AIN (BOARD, CHAN3, GAIN1, VALL1, XER)
480 CALL AIN (BOARD, CHAN, GAIN, VALL, XER)
490 CALL AIN (BOARD, CHAN5, GAIN2, VALL2, XER)
500 Y=VALL*(57/4096)+2
510 Y1=VALL1*(57/4096)+62
520 Y2=VALL2*(57/4096)+122
530 T1! = TIMER
540 PSET (X+35,Y)
550 PSET (X+35,Y1)
560 PSET (X+35,Y2)
570 WRITE #1,X,VALL
580 WRITE #2,X,VALL1
590 WRITE #3,X,VALL2
600 IF INT(T1!-T0!) = (IND + 25) THEN GOTO 660

```

```

610 IF FLAG = 1 THEN GOTO 630
620 IF INT(T1!-T0!) = IND THEN GOSUB 930
630 X=X+.5
640 IFLEN = IFLEN + 1
650 GOTO 470
660 SCREEN 0
670 CLOSE #1,#2,#3
680 CALL PULSE (BOARD,CHAN1,RANGE,PERIOD,XER)
690 FOR S = 1 TO 3
700 READ L$
710 IFILE$ = L$ + FILE$
720 OFILE$ = L$ + FILEA$
730 BFILE$ = "E:" + OFILE$
740 OPEN IFILE$ FOR INPUT AS #2
750 OPEN BFILE$ FOR OUTPUT AS #1
760 PRINT #1,"**"
770 ABSMIN =0!
780 ABSINC =-1!
790 IFTYPE = 1
800 PRINT #1,USING "\          \ ";OFILE$;
810 PRINT #1,USING "\          \ ";OFILE$
820 PRINT #1,USING "# ";IFTYPE;
830 PRINT #1,USING "#### ";IFLEN;
840 PRINT #1,USING "#.#####^ ^ ^ ";ABSMIN;ABSINC
850 FOR I= 1 TO IFLEN
860 INPUT #2,X,Y
870 PRINT #1, USING F$; Y
880 NEXT I
890 CLOSE #1,#2
900 DATA T,C,V
910 NEXT S
920 END
930 CALL PULSE (BOARD,CHAN2,RANGE,PERIOD,XER)
940 FLAG = 1
950 RETURN
960 CALL PULSE (BOARD,CHAN1,RANGE,PERIOD,XER)
970 GOTO 920

```